Aus der Klinik für Strahlentherapie und Radioonkologie,

Universitätsklinikum des Saarlandes, Homburg/Saar

Direktor: Univ. Prof. Dr. med. Ch. Rübe

Monte-Carlo simulation of the Siemens Artiste linear accelerator flat 6 MV and flattening-filter-free 7 MV beam line

Dissertation zur Erlangung des Grades eines

Doktors der Naturwissenschaften

der Medizinischen Fakultät

der UNIVERSITÄT DES SAARLANDES

2018

vorgelegt von: Alemeh Sadrollahi

geb. am: 12.03.1988 in Damghan

Index

Summary

There have been a number of Monte Carlo studies of clinical linear accelerators in the past years but only few of them focused on flattening filter free beams and a small handful of them consider a Siemens linear accelerator. The aim of this work is to provide the up-to-now missing information on the Siemens Artiste FFF 7 MV beam line using a Monte-Carlo model fit to the realistic dosimetric measurements at the linear accelerator in clinical use at our department.

The main Siemens Artiste 6 MV and FFF 7 MV beams were simulated using the Geant4 toolkit. The simulations are compared with the measurements with an ionization chamber in a water phantom to verify the validation of simulation and tune the primary electron parameters. Hereafter, other parameters such as surface dose, spectrum, symmetry, flatness/unflatness, slope, and characteristic off-axis changes are discussed for both Flat and FFF mode.

Fine-tuning the electron beam parameters and of the flattening filter were the most important challenges in this simulation, because these parameters verify the validity of the simulation after creating the geometry. In contrast to other vendors (Varian or Elekta), the Siemens implementation increases the incident electron beam energy for the FFF beam line to create closely similar depth-dose curves for the flat 6 MV and FFF 7 MV beams. Therefore, the

mean electron energy for the FFF beam was 8.8 MeV and 7.5 MeV for flat 6 MV, the spread energy and spot size of the selected Gaussian distribution source were 0.4 MeV and 1mm, respectively. There is good agreement between calculation and experimental results; the absolute differences were less than 2% and in the most cases less than 1%.

The dose rate of the FFF beam was 2.8 (2.96) times higher than for the flattened beam for a field size of 10×10 (20×20) cm^2. The penumbra, surface dose and the mean energy of photons decreased by removing the flattening filter. Finally, the results show that the off-axis changes had no strong effect on the mean energy of FFF beams and this effect was even more considerable for the flattened beam.

Zusammenfassung

Verschiedene Studien haben Monte Carlo Simulationen für klinische Linearbeschleuniger durchgeführt, allerdings waren nur die wenigsten davon auf flächungsfilterfreie (FFF) Energien ausgelegt. Speziell die an den Siemens Linearbeschleunigern verwendete Implementierung der FFF Technik wurde bisher noch nicht mit Monte-Carlo-dosimetrischen Methoden untersucht. Das Ziel dieser Arbeit ist es, diese bisher fehlenden Informationen für eine Siemens Artiste FFF 7 MV Modalität bereitzustellen, unter Verwendung eines Monte Carlo Models, welches an reale dosimetrische Messungen an einem Linearbeschleuniger in klinischer Nutzung an unserer Einrichtung angepasst wurde.

Die Hauptenergien der Siemens Artiste Maschine, 6 MV und FFF 7 MV, wurden mit dem Geant 4 Toolkit simuliert. Diese Simulationen wurden mit Messungen verglichen, die mit einer Ionisationskammer im Wasserphantom aufgenommen wurden, um die Validität der Simulation zu verifizieren und die Parameter für die Primärelektronen einzustellen. Im Anschluss werden andere Parameter wie die Oberflächendosis, das Spektrum, die Symmetrie, die flatness bzw. unflatness, die Steigung und die charakteristischen off-axis Veränderungen sowohl für den flachen, als auch den FFF Modus diskutiert.

Die Feinabstimmung der Elektronenstrahlparameter sowie des Ausgleichsfilters waren die größten Herausforderungen dieser Simulation. Im Gegensatz zu anderen Anbietern (Varian oder Elekta, wird bei Siemens die Strahlenergie für den FFF Modus erhöht, um annähernd gleiche Tiefendosiskurven für 6 MV und FFF 7 MV Photonen zu erhalten. Aus diesem Grund

war die mittlere Elektronenenergie für die FFF-Modalität 8,8 MeV und für 6 MV 7,5 MeV. Die Energiebreite und Spotgröße der gewählten Gaußschen Quelle waren 0,4 MeV und 1 mm. Die Übereinstimmung zwischen den Berechnungenund den experientellen Ergebnissen war sehr gut; die absoluten Unterschiede betrugen weniger als 2%, in den meisten Fällen sogar weniger als 1%.

Die Dosisrate des FFF Strahls war 2,8 (2,96)- mal höher als die des flachen Strahls für eine Feldgröße von 10×10 (20×20) cm^2. Der Halbschatten, die Oberflächendosis und die mittlere Energie der Photonen wurden durch die Entfernung des Flächungsfilters verringert. Schlussendlich zeigen die Ergebnisse, dass die off-axis Änderungen keinen starken Effekt auf die Strahlenergie der FFF Modalität haben, wobei dieser Effekt deutlich bedeutender für den flachen Strahl war.

1. Introduction

1.1 Radiation Therapy

Radiation therapy or radiotherapy is one of the three commonly used methods for treating a tumor (surgery and chemotherapy are other two). Radiation therapy is based on the interaction of electromagnetic waves (X-rays and gamma rays), charged particles (electrons, protons and heavy ions) and neutral particles (neutrons) with body tissue at the molecular level. The quality and intensity of these interactions depend on the energy of the primary or – in case of photons and neutrons – secondary charged particles, which are usually electrons. The charged particles can break the chemical bonds and damage cells by ionization damage to the DNA (deoxyribonucleic acid). The purpose of radiotherapy is to transfer a sterilization dose to the tumor in such a way that the least possible harm is caused to the healthy tissues surrounding the tumor.

Radiation may be used in early-stage cancer for definite or adjuvant treatment. It can be used prior to surgery to shrink the tumor, or after surgery to prevent locoregional relapse, or radiation may be used palliatively to alleviate the effects of the disease, such as pain from the main cancer location. Radiation may also be used to prevent cancer growth in some other areas at risk for metastases. In some types of cancer, radiation may be combined with surgery or chemotherapy. In these cases, the treatment plan is coordinated between the surgeon, the medical oncologist and radiation oncologist.

Treatment plan

The treatment planning process is complicated and it may take several days, but it is one of the most important parts of radiation therapy.

The first part of treatment planning is called simulation. In the commonly used virtual simulation technique, the physician will delineate the size of the tumor with the presumed spread and healthy tissues within the treatment area on a computed tomography (CT) scan that provides a three-dimensional image of the patient. Treatment planning also involves prescribing the treatment dose to the tumor and creating a treatment plan, mostly based on the CT data set.

The radiation dose that is prescribed to the patient depends on the size of the tumor, the sensitivity of the tumor to radiation, and the ability of the healthy tissue to tolerate radiation. In general, the total prescribed radiation dose is divided into several smaller fraction doses that are given to the patients over the course of several weeks. This causes less damage to healthy tissues. For example, treatments are usually given to the patient on a daily basis, 5 days a week, for 5 to 7 weeks.

1.2 Different Radiation Therapy Techniques

External radiation therapy

External or percutaneous radiation therapy is the most common type of radiation therapy. In this method, radiation is applied from an external source on the cancerous area. The systems producing ionizing radiation for external beam radiation therapy are: radioactive isotope systems like cobalt-60 and cesium-137 (now mainly obsolete), X-ray generators which are divided into different groups in terms of X-ray energy (soft X-rays are mainly used for surface treatment), and electron accelerators (linear accelerators) operating at megavoltage energies.

Internal Radiation Therapy (Brachytherapy)

Internal radiation therapy as brachytherapy, which means short-distance therapy, directly places the source of radiation inside or close to the target volume. Brachytherapy is capable of delivering a high dose of radiation to a small area with comparatively good sparing of organs

at risk, but can only be applied to tumor localizations accessible to the radiation source. The two main divisions are interstitial radiation and intracavitary radiation.

Intra-operative radiation therapy

In this method, the radiation is delivered directly to the cancerous area during surgery. This method is often used in abdominal cancers, pelvis cancers and cancers that tend to relapse. Intra-operative radiation therapy (IORT) reduces the amount of tissue that is exposed to radiation, so healthy tissues are protected during surgery. In this method, a high single dose can be used.

3D Conformal Radiation Therapy

3D Conformal Radiation Therapy (3D-CRT) enhanced the planning of radiation therapy treatment by providing 3D of perception of the tumor and surrounding normal tissue. 3D-CRT coordinates the treatment volume to the shape of the tumor by using a multileaf collimator (MLC). Consequently, the maximum radiation dose is delivered to the tumor while surrounding normal tissues are more protected.
The patient is fixed with different positioning localization devices to keep the body immobile in order that the radiation can be accurately targeted from several directions.

Intensity-modulated radiation therapy (IMRT)

Intensity-modulated radiation therapy (IMRT) is the next generation of 3D-CRT. This technique is used for the tumors with concave or complex shapes which are placed close to organs at risk. It has two key additional features compared to conformal radiotherapy: Non-uniform intensity of the radiation beams and computerized inverse planning [68].

Volumetric modulated arc therapy (VMAT)

Volumetric modulated arc therapy (VMAT) is a new technique in radiation therapy which was first introduced in 2007 that allowed the simultaneous variation of three parameters during treatment delivery, *i.e.* gantry rotation speed, treatment aperture shape via movement of MLC leaves and dose rate. Therefore, this method can deliver high-quality dose distributions in less time comparing with IMRT or 3D-CRT [69].

Stereotactic Radiosurgery

This method delivers a very high dose to a small tumor area in one (stereotactic radiosurgery) or few treatment fractions (stereotactic radiation therapy). The most commonly treated indication is the brain, but small tumors in the lung, liver of vertebra may also receive stereotactic treatment. Both linear accelerators and dedicated machines (gamma knife, cyber knife) are used for this technique.

1.3 Aim of this work

This thesis focusses on the physical modelling of a linear accelerator (linac) used for radiotherapy treatment. The linac installed at the Department of Radiotherapy of the Saarland University Medical Center is equipped with a new technique for obtaining higher-output photon beams, called a flattening-filter-free (FFF) mode. This technique has been developed and implemented in recent years and is still relatively new to the clinical routine.

The main reason to use FFF mode is an increase in dose rate by a factor of about 2-4. High dose rate implies shorter treatment time and this is thought to be useful in managing the intrafractional patient and organ motion and reduce the dose to critical organs outside the treatment volume. For example, in a given stereotactic treatment for a 25 Gy single-fraction, the beam-on time was reduced from circa 15 minutes to circa 7 minutes with 15%-5% reduction in dose to healthy organs near the cancer [71].
Furthermore, linac head leakage will also be smaller for FFF beams because of reduction of treatment time. A further reduction comes from the fact that about one-third of all scattered radiation which is produced in the head of the linac arises from the flattening filter (FF). So by removing it, the head scatter is again significantly reduced. This reduces the undesirable dose in the patient and also improves dosimetry in FFF mode with comparing FF mode.
In addition to this, the flattening filter selectively hardens the spectrum (according to the off-axis distance because of the variable thickness of the FF), which may impact on different dosimetric characteristics such as spectrum, depth-dose profile, maximum dose, surface dose.

Although a number of studies exist that have presented realistic physical models for linear accelerators in FFF mode, none of them have investigated the Siemens Artiste linac model, in which the FFF technique is implemented in a different way from the other manufacturers. In particular, a frequently observed disadvantage of FFF beams, a decreased beam energy and consequently increased surface dose, was addressed in the Siemens design by increasing the acceleration energy. No information about the success of this procedure exists, the surface dose and energy spectrum have not been published so far. The aim of this thesis is therefore to characterize the dosimetric properties of the FFF beam line in comparison with the corresponding flat beam.

The bases for linear accelerator functioning are presented in Chapter 2. The physical design of the Monte Carlo model is explained in Chapter 3. After obtaining a realistic model that matches the dosimetric measurements, the dosimetric characteristics of the FFF mode are presented and compared with the standard beam-line (6 MV flat beam) (Chapter 4) and are compared with the corresponding results for linear accelerators by the Varian and Elekta manufacturers which follow a different technical implementation in Chapter 5.

2. Theory

2.1 The physics of percutaneous radiation therapy with an electron linear accelerator

High energy photon production

Megavoltage X-ray beams used in medical application are usually produced by electron linear accelerators (linacs). For creating high-energy photons, a linac uses high-frequency electromagnetic waves to accelerate electrons to high energy inside a vacuum tube. These high energy electrons are directed onto a high-density target to produce megavoltage photons via Bremsstrahlung interaction.

Figure 2.1 shows a schematic of how electrons accelerate in a linear accelerator. An electron gun is required to produce free electrons, where electrons are boiled off a hot cathode, with an energy of about 50 KeV. These free electrons enter a wave guide, which consists of a hollow rectangular copper piping system filled with of SF_6. This so-called klystron produces pulsed microwaves which interact with the ejected electrons. By this interaction, the ejected electrons absorb energy and so are accelerated, forming bunches.

Electrons exit from the 1-1.5 m length of the wave guide and enter the bending magnet assembly. Achromatic bending can be either through 90˚ or 270˚, but most medical linear accelerators employ a 270˚ for energy filtering. This design typically directs the electrons

towards the high-density target to create bremsstrahlung photons. In this case, bremsstrahlung photons are produced when electrons as negatively-charged particles interact with positively charged nuclei of the target and slow down.

Photon with energy of $E=h\upsilon$ ($h=6.6\ 26 \times 10^{34}$ [m^2 kg / s] is Planck's constant and υ is photon frequency) are created due to the loss of energy of the electrons. Finally, the photon beams travels through other linear accelerator components to be modulated and shaped for delivering a desired dose in patient or phantom [4].

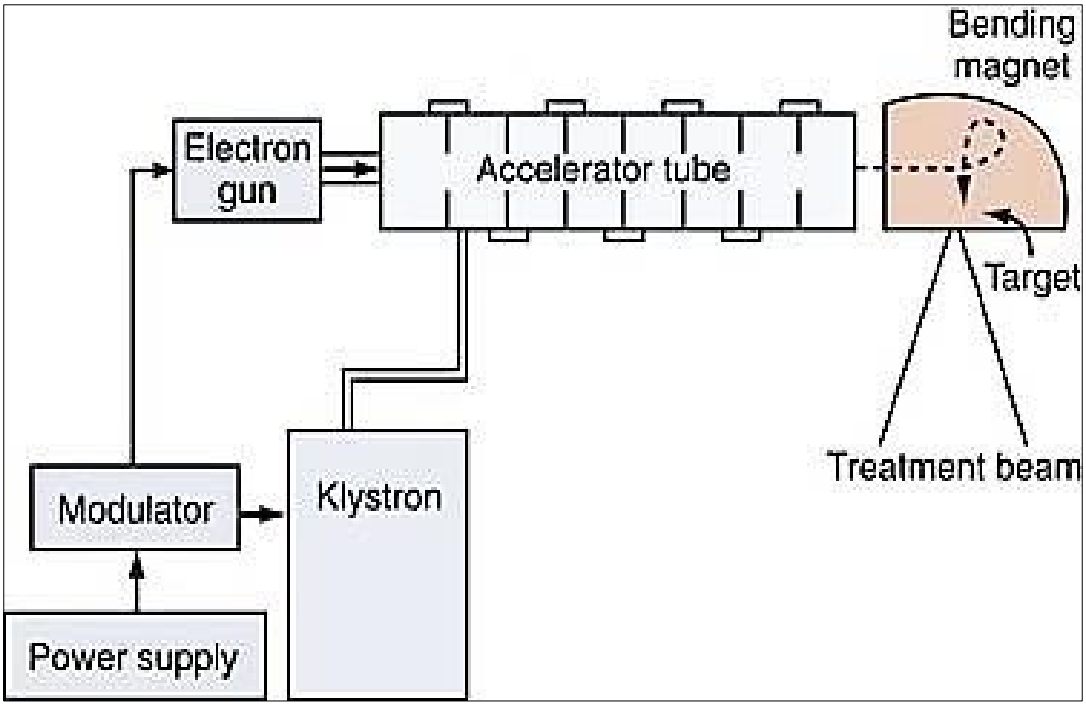

Figure 2.1 Schematic a linear accelerator [41]

The area the electron beam strikes on the target is called the spot size. The spot size of the primary electrons has a direct effect on the penumbra in the dose profile.

The penumbra is defined as the region near the edge of the field where the dose falls off rapidly and is one of the factors that reduces the radiation effectiveness. The nominal physical penumbra is the sum of three individual penumbras, a) transmission penumbra, created by

transmission through the collimator jaws, b) geometric penumbra, attributed to the source size and c) scatter penumbra, due to the X-ray scatter [38].

Generally, the physical penumbra may be attributed to electron contamination and low-energy electron which are scattered from linac head. For the geometric penumbra, it depends strongly on the spot size and can be minimized by using a small source diameter (Figure 2.2).

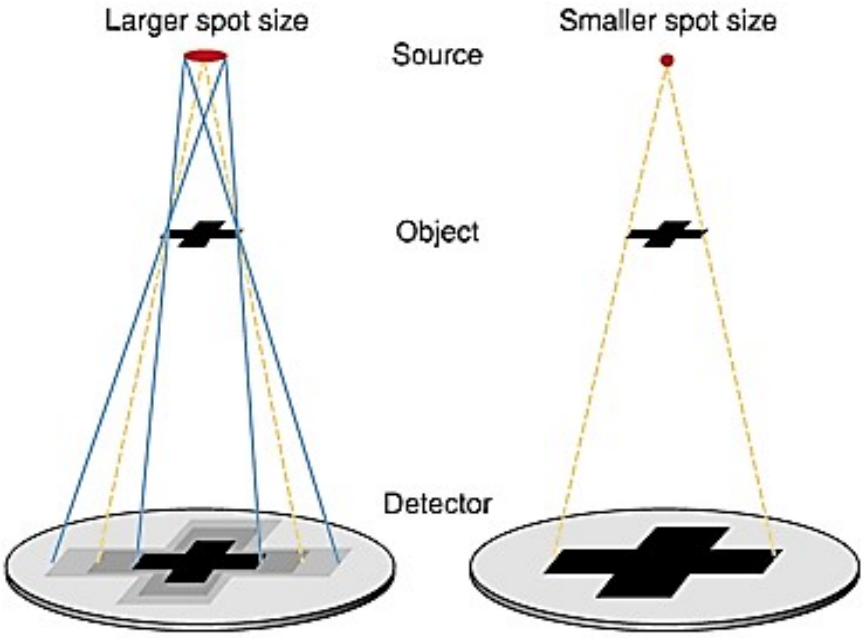

Figure 2.2. Diagram of the geometric penumbra due to the spot size. A narrower spot size will leave a smaller penumbra region, while a large spot size will cause a large penumbra [42]

Although the primary electrons are mono-energetic, the bremsstrahlung photons are generated with a continuous spectrum of energies. The original spectrum in vacuum has a maximum at zero with negative slope to a minimum at maximum cut-off energy of the primary electron energy (Figure 2.3, Kramers' law)

$$I(\lambda)\,d\lambda = K\left[\frac{\lambda}{\lambda_{min}} - 1\right]\frac{1}{\lambda^2}\,d\lambda \qquad (2.2)$$

where I is the distribution of intensity (photon count) against the wavelength λ, K is proportional to the atomic number of the target element, and λ_{min} is the minimum wavelength given by the Duane–Hunt law. Aacording to this law, $\lambda_{min}=hc/eV$, where *h* is Planck's constant, *e* is the charge of the electron, *c* is the speed of light, and λ_{min} is the minimum wavelength of X-rays that can be emitted by Bremsstrahlung interaction in an X-ray tube by accelerating electrons through an excitation voltage V into a metal target [54].

In the linear accelerator target, this spectrum of photons is filtered by self-attention. Because of this filtering, low-energy photons are preferentially absorbed. For primary electrons with keV energy, the resulting spectrum curve is peaked approximately at 1/3 of the primary electron energy; this peak moves approximately 1/6 of the primary electron energy if electrons are accelerated in the MeV range.

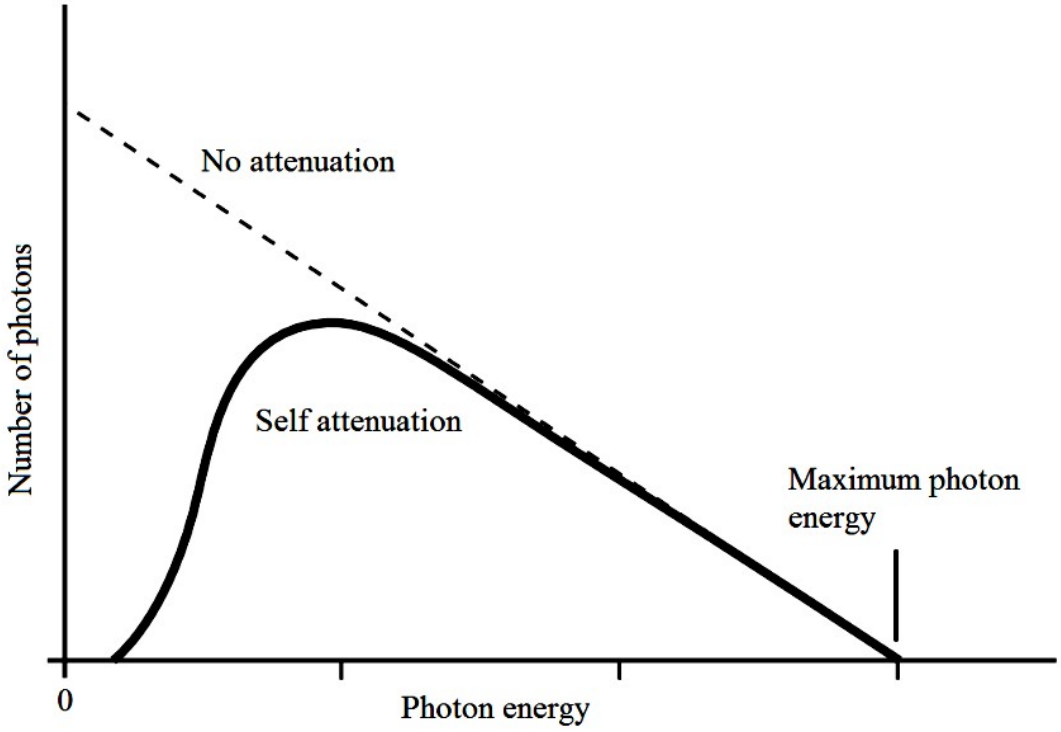

Figure 2.3. A plot of an X-ray spectrum produced from an electron beam

The angular distribution of bremsstrahlung photons depends strongly on primary electron energy. Figure 2.4 shows a schematic illustration of the spatial distribution of bremsstrahlung photons. As this figure shows, most photons in the MV range are produced around the

direction of primary electrons, φ=0, and there is a sharp fall-off in photon fluence for high angles. For example, for 10 MeV the angular distribution is about 1.4˚ while, this angle for 100 KeV electrons is about 64.4˚.

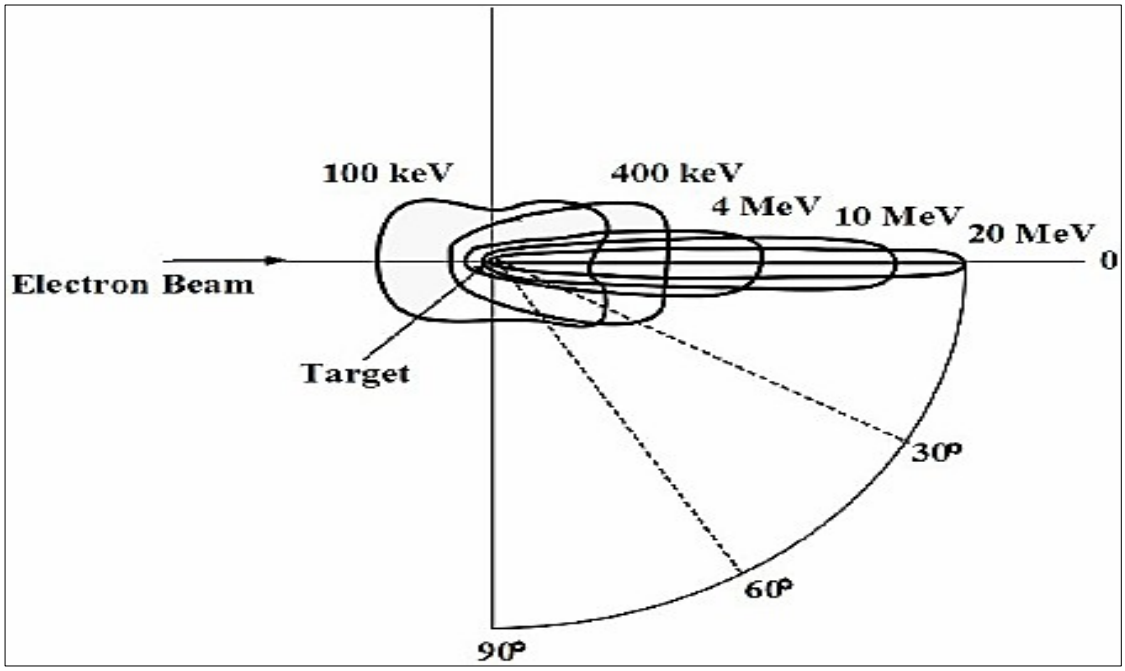

Figure 2.4. Schematic illustration of the spatial distribution of X-ray photon scaused by bremsstrahlung off a thin target [26]

2.2 Linear Accelerator Gantry Head

In radiation therapy, the X-ray treatment beam must have particular properties: they must be created with well-defined different size, the energy and intensity of the beam should be controllable, they must be aimed at the patient from any desired direction with high accuracy, the dose pattern must be stable and must be accurately monitored during treatment [19].

To achieve these aims, most medical linear accelerator gantry heads are designed a similar way to Figure 2.5. The role of every component in the modification and shaping of the X-ray is explained in the following.

The Primary Collimator:

When accelerated electrons are incident on the target, a broad high-energy photon beam is produced. The divergence of the resultant beam is restricted by a conical block of highly attenuating material that surrounds the target, known as the primary collimator.

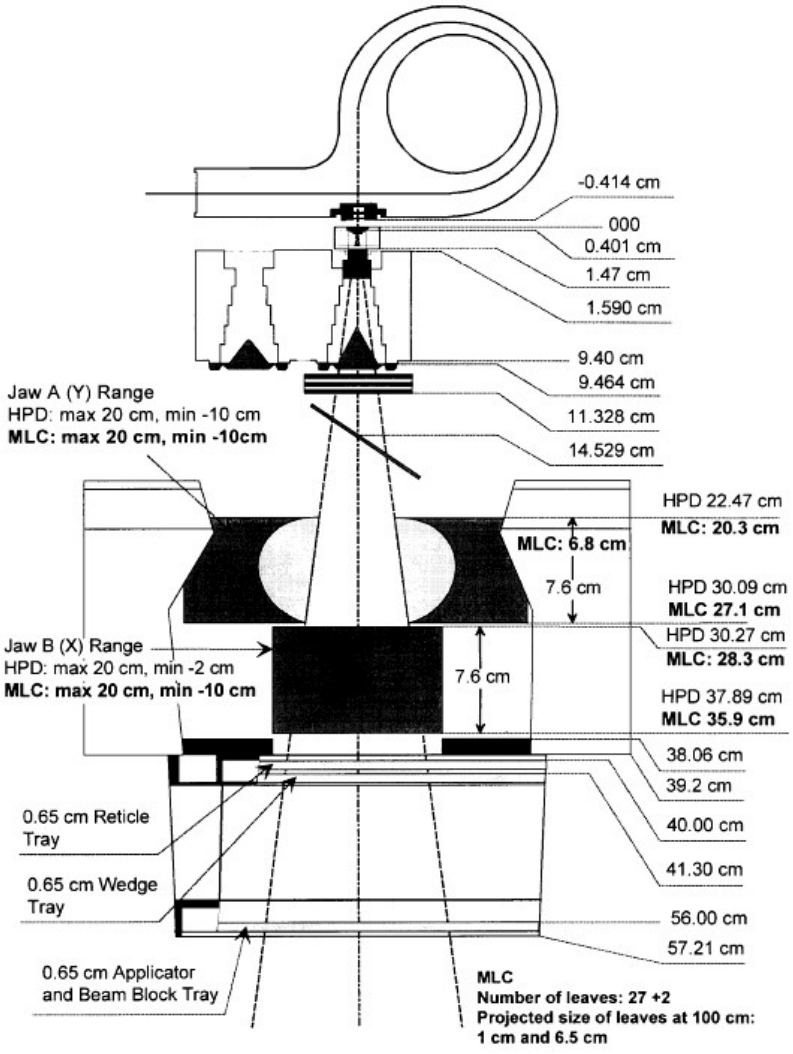

Figure 2.5. Cross-sectional schematic of Siemens Artiste linear accelerator gantry head

Flattening Filter (FF):

According to Figure 2.4, bremsstrahlung photons produced by higher electron energy (generally 4-20 MeV electron beams in cancer radiation therapy) have a sharp angular distribution. In early treatment planning, it was highly desirable to have flat energy fluence because of 3D-CRT treatment planning; therefore, to produce such a uniform beam, a FF has been routinely employed in medical linear accelerators since the 1950's. The FF has a cone shape to attenuate the sharp peak on the central axes of the bremsstrahlung photon beam more than the beam edges (Figure 2.6) and hence create uniform fluence within the open beam.

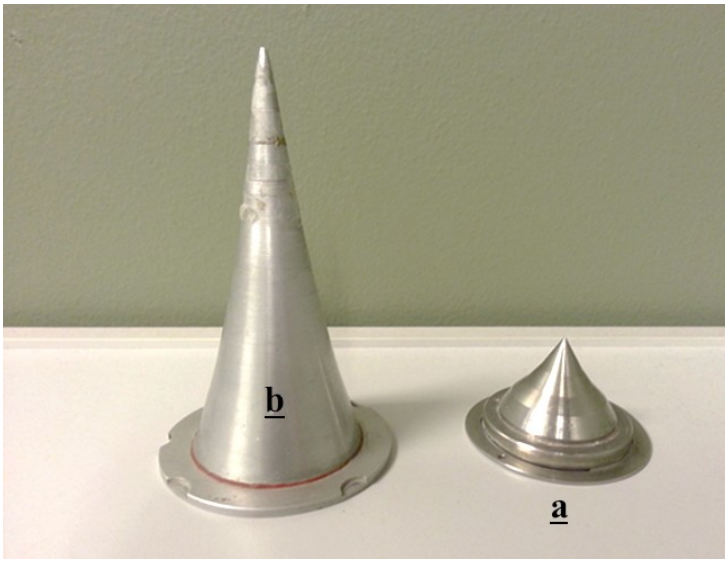

Figure 2.6. Varian Flattening filter of in medical linear accelerators
a) low energy, b) high energy [8].

The monitor chamber:

The dose monitoring system consists of several ionization chambers or a single chamber with multiple plates. The chambers are usually of transmission type, such as parallel plate or cylindrical thimble chambers. This component is used to measure the machine output and beam flatness and symmetry during treatment. As the delivered dose to each point depends on the beam and measurement geometry (source-surface-distance, measurement depth etc.),

ionization chamber measurements report the dose delivery rate in the arbitrary unit “monitor unit per minute” (MU/min).

Medical linear accelerators are then calibrated under a given reference condition generally in such a way that 100 MUs correspond to a delivered absorbed dose of 1 Gy at the depth of maximum dose (d_{max}) in a phantom placed at source-surface-distance 100 cm for a field size of 10×10 cm^2.

The secondary collimator:

The secondary collimator consists two pairs of opposing blocks, the upper blocks are called x-jaws and and lower blocks y-jaws. These blocks are usually made of lead or tungsten to provide a rectangular field size at the linear accelerator iso-center. The jaws can be moved to any desired field size (with a maximum of 40 cm for the linac analysed in this thesis).

The Multileaf Collimator:

A multileaf collimator (MLC) can be used in addition to or as a replacement to one pair of jaws (for the Siemens Artiste linac, it replaces the X jaws). It is a collective of movable leaves of high atomic material, which block the radiation beam forming complicated shapes by moving individual leafs. MLC’s are used to alter the shape of the linear accelerator beam to match the border of the target-tumor to decrease the absorbed dose in healthy tissue. Without MLC’s, the linear accelerator can only treat square or rectangular shapes. Depending on the linear accelerators type and brands; they have 40 to 160 leaves, arranged in pairs (Figure 2.7).

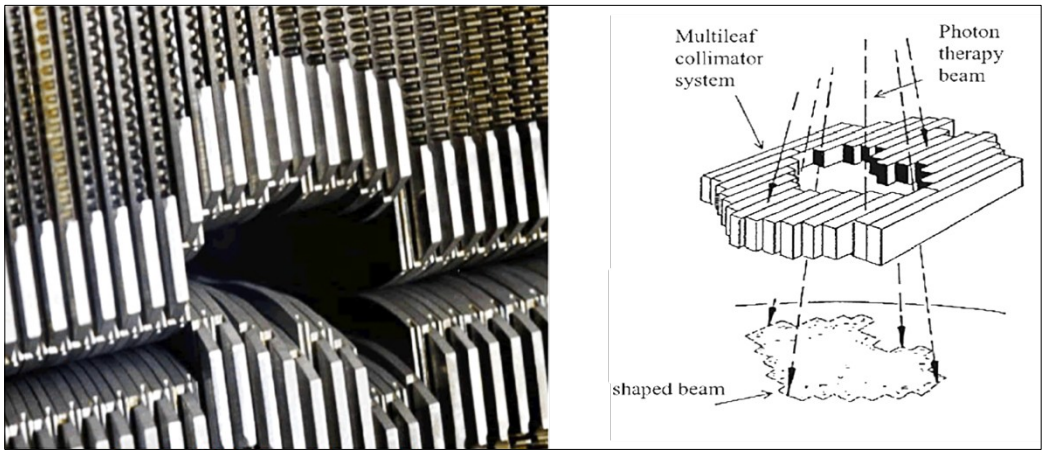

Figure 2.7. 160 MLC with a certain shape open field [1].

2.3 Flattening Filter Free (FFF) Beam

While adding the flattening filter (FF) to the linac head has some disadvantages, most notably the decreased dose rate, it was a necessary component of linacs in the past because of the requirement of early treatment planning of uniform photon fluence profiles. Advancements of recent radiation therapy techniques, such as stereotactic radiation therapy and intensity modulated radiation therapy or volumetric-modulated arc therapy, allow for the use of unflattened beams, so the flattening filter free (FFF) mode becomes an option. In the recent past, many Monte Carlo calculation and experimental studies have dealt with the dose characteristics of radiation produced when the FF is removed from standard linacs[1]. According to these studies, the FFF mode is clinically suitable and in some aspects superior over a flat photon beam.

2.4 Dose Deposition

The quantities used to measure ionizing radiation are based on the biological, physical, or chemical effects of radiation. This effect mainly depends on the energy transfer of radiation to the environment and how this is distributed in the material. The amount of transferred energy or deposited energy in the material depends on the type of particle, the energy of the particle and the absorbing material (e.g., water or soft tissue). In radiation therapy, most of the dose in the patient is generated by megavoltage bremsstrahlung photons undergoing several types of interactions. The present section will talk about important photon interactions with material and their probabilities. In the following, the absorbed dose and its properties will be described.

2.5 The interaction of X-rays and matter

X-ray photons may encounter orbital electrons or atomic nuclei. Often, in the X-ray energy domain, collisions occur with orbital electrons. There are five main interactions of an X-ray photon with matter: coherent scattering, photoelectric effect, Compton scattering, pair production, and photodisintegration.

[1] [11, 16, 23, 34, 35, 36, 37, 40, 49, 51, 63, 70, 72, 73]

Coherent Scattering:

Coherent scattering changes the direction of the photon beam without making any changes in the wavelength and hence energy. This collision is in the form of the Thomson and Rayleigh scattering. Thomson scattering involves a single electron in the collision, but the Rayleigh scattering results from a collision with all the electrons of an atom. In the X-ray energy range, a small contribution from coherent scattering is detected, therefore, this does not contribute much dose in matter.

Photoelectric effect:

In this collision, a photon with energy slightly higher than the energy of a bound electron from an atom collides with one of the orbital electrons and removes it from its orbit. All photon energy is transferred to the electron and it is released in the form of a free photoelectron into the environment. The remaining empty energy level is filled by one of the electrons in the higher shells and the energy difference is emitted in form of characteristic X-rays. The photoelectric collision depends on two factors: radiation energy and the atomic number of the absorber. The larger the electron density of a material, the higher the probability of photon interactions with the electrons of that material, therefore, the photoelectric absorption cross-section increases with the fourth power of the atomic number (Z). In contrast, the photoelectric absorption cross-section (σ) decreases with the third power of energy.

$$\sigma \frac{Z^4}{E^3} \qquad (2.\ 2)$$

Compton Scattering:

Compton's model for the interaction of a photon and an electron is based on the assumption that the electron must be almost free and stable. Of course, every electron in the matter moves and is partially bound to the atoms of its mother, but the electrons of the outer layers of the atom can be considered to be practically free. In contrast to the photoelectric effect, in

Compton scattering the photon is not destroyed, but is elastically scattered by the electron (Figure 2.8).

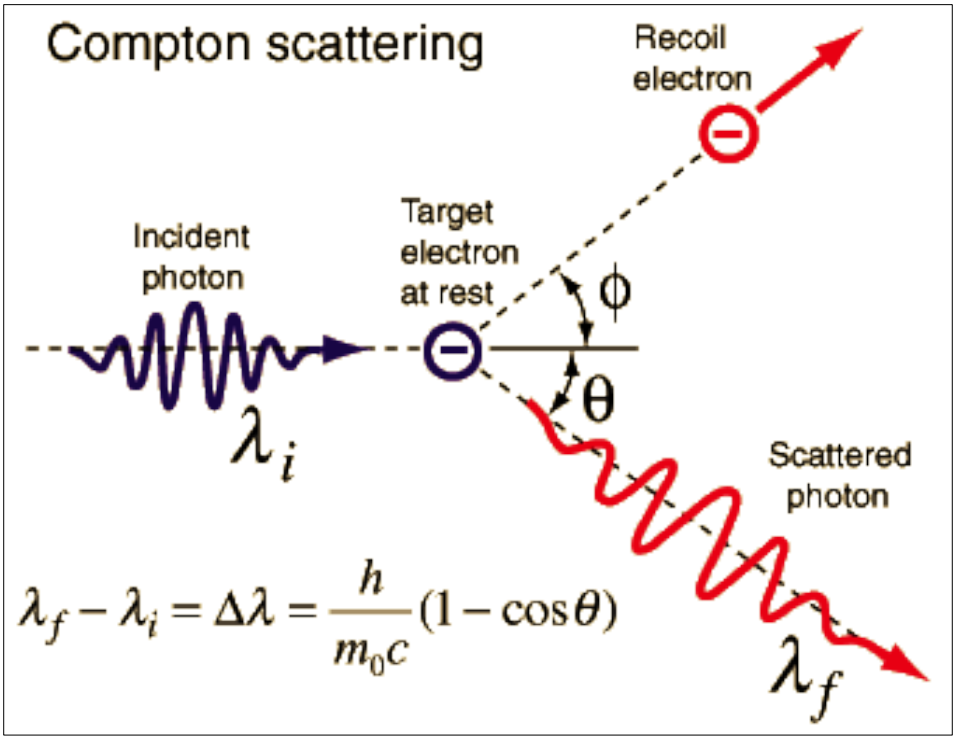

Figure 2.8. Schematic of Compton scattering [77]

In this case, some the photon momentum transfers to the electron. Therefore, the momentum and the energy of the scattered photon is less than the amount of momentum and the energy of the incident photon. The photon scattering cross section at various energies is described by the Klein-Nishina Formula as:

$$\frac{d\sigma}{d} = \alpha^2 r_c^2 P \qquad (2.2)$$

Where E_γ is the input photon energy and:

$$\alpha = \frac{1}{137} \quad , \quad r_c = h/m_e \qquad (2.2)$$

$$P\left(E_\gamma, \theta\right) = \frac{1}{1 + \left(E_\gamma / m_e c^2\right)} \qquad (1.2)$$

The scattering cross-section at different angles for the different energies of the input photon is presented in Figure 2.9.

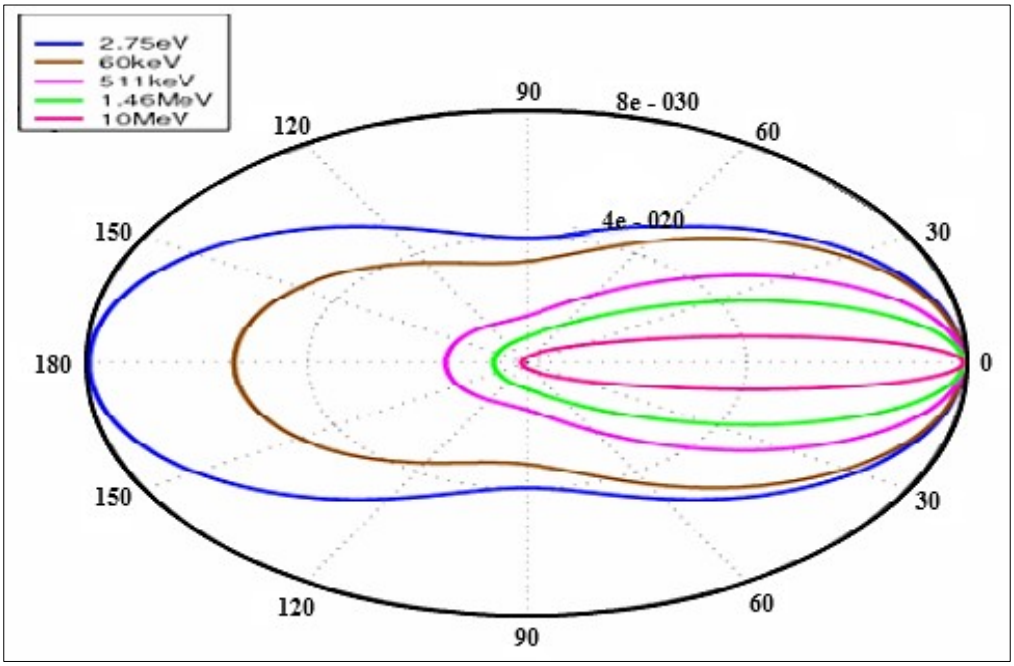

Figure 2.9. Distribution of scattering-angle cross sections over commonly encountered energies observed by *Klein* and *Nishina* [55].

Pair Production:

While passing through the field of the atomic nucleus, a high-energy photon (over 2×511 keV) can disintegrate and form an electron-positron pair. Energy and momentum are conserved, so that the two particles travel in nearly opposite directions.

Photodisintegration:

In photon decomposition, the nucleus of an atom is decomposed by a high energy photon, releasing neutrons or protons, alpha particles, or a bunch of particles. The photon should have enough energy to overcome the core binding energy of 7MeV to 15 MeV. In the case of photon radiation therapy, the probability of this interaction is very low and is generally ignored.

The linear attenuation coefficient of X-rays:

When X-rays collide with an absorbing material, they can interact with the atoms through each of the five mechanisms described and lose their energy along the way, until they deposit all of energy in the absorber. In these interactions, the amount of beam attenuation is determined by the number of incident photons that cannot continue in their original path and are eliminated from the passage of beams. In this relation, the total reduction in the number of initial X-rays by a certain material thickness is called attenuation of radiation.

According to the Lambert-Beer law (Equation 2.6) , the decrease in intensity of the X-ray beam depends on the thickness (x) and absorption coefficient (μ) of matter. as

$$I(x) = I_0 \exp(-\mu x) \qquad (2.2)$$

I_0 is the initial X-ray beam intensity, I(x) is the intensity after a thickness of x. By introducing absorption coefficient (μ), it is possible to summarise the probability of occurrence of the named interactions.

The total linear attenuation coefficient includes the corresponding coefficient for each type of interaction:

$$\mu = \mu_{PE} + \mu_{coh} + \mu_{CS} + \mu_{PP} \qquad (2.2)$$

Equation 2.7 gives the total linear attenuation coefficient, where μ_{PE}, μ_{coh}, μ_{CS} and μ_{PP} represent the coefficient for photoelectric, coherent, Compton and pair production interactions, respectively. As the coefficient depends on the density of material this quantity is often shown as the mass attenuation, $\frac{\mu}{\rho}$ ($\frac{cm^{-1}}{g/cm^3} = cm^{2/g}$. Figure 2.10 shows the total mass attenuation coefficient for soft tissue at different energies.

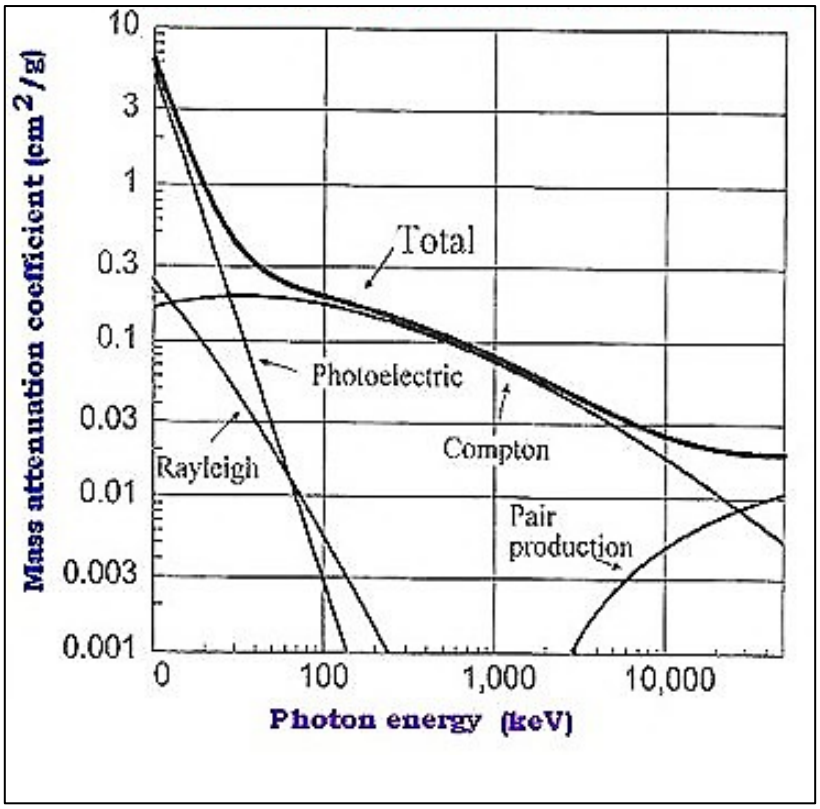

Figure 2.10. Total mass attenuation coefficient for soft tissue [56]

2.6 Dosimetry

The energy absorbed by the tissue (radiation dose) is an important factor in the probability of the incidence and severity of the biological effects of the beam. In estimating the actual risks, several other important factors are important for the biological effects of radiation, such as tumor and tissue radiation sensitivity, repopulation, DNA repair, etc.

Radiation Dose (D)

The amount of energy absorbed per unit mass is called absorbed dose or radiation dose (Gy), a Gray corresponds to 1 Joule absorbed by 1 kg of material (1 Gy = 1 J/kg). Before the SI (The International System of Units**)** replaced the older unit by the Gray, dose was measured in rad (radiation absorption dose, 1 Gy = 100 rad).

dD/dt

Dose rate is the amount of energy absorbed per unit time and mass.

2.7 Monte Carlo Method

Overview of the Monte Carlo method

In the 1970s and early 1980s, Monte Carlo (MC) methods were introduced into medical physics [6]. At that time, simple geometries in a water phantom were modelled for homogeneous irradiation by point sources. After that, the use of MC simulation in medical physics has been widely increased and currently, this method has numerous applications in medical physics, such as micro and nano dosimetry. In the case of the radiation therapy, the MC method is the most accurate method to simulate and determine the dose deposition. For dose calculation, this method develops dose deposition from physical knowledge and data of the principal interaction of particles, such as attenuation coefficient and cross-section data instead of using corrections to existing measurement data [65]. There are many MC calculation engines to predict deposited dose but because of the exorbitant calculation time, very few engines are employed in medical physics routine applications. They are an excellent alternative to analytical approaches, which can be inadequate due to simplifications in the analytical calculation models.

MC is a numerical technique which simulates the individual trajectories of each particle by using random sampling of probability distributions to solve problems. In MC applications, a particle which is transported from the source and its daughter particles which are created in different interactions along the path of simulation is referred as “particle history”. In order to achieve a high statistical accuracy in predicting physical quantities, a large number of histories are required. In fact, the statistical uncertainty of a simulation depends on number of considered histories N and usually decreases as $N^{-1/2}$ [47].

Particle Simulation

As previously mentioned, to utilize the MC method, the problem must have the ability to produce random numbers and have a stochastic model, therefore, a simulation of particle interactions is an ideal model for applying the MC method because particle interactions are inherently stochastic in nature. The random numbers and probability distributions are two significant elements which are used to simulate each step of the particle trajectory and choosing in each step the type of interaction and particle state (energy, direction).

Electron and photon transport

The simulation of electrons and photons, which are important particles in radiation therapy, has some difficulties because of the generation of secondary particles, such as bremsstrahlung photons, delta ray, X-ray fluorescence and Auger electrons. Bremsstrahlung photons created by electrons were already mentioned. Delta rays are secondary electrons which are ejected from their orbit with energy higher than the ionization energy so they can escape a significant distance away from the primary radiation beam and produce further ionization [7]. An Auger electron is produced through a physical phenomenon called Auger effect. In this phenomenon a core electron leaves a vacancy and an electron from a higher level quickly fills this vacancy. When this transition occurs, there are two possibilities to match the quantum energy with the energy gap between upper and lower level. The first probability is a photon is emitted called X-ray fluorescence. On other cases, an electron from the outer level is emitted, called Auger electron [28, 48].

In general terms, radiation transportation in the MC method is simulated in four main steps:

a) determine the step size (length of the path travelled by particle before an interaction occurs),

b) transport to the interaction point taking the geometry into account,

c) determine the interaction type (probabilistic sampling) and

d) simulate the interaction and determine the energy and angle of deflection of the particle and every daughter particle.

All these steps are repeated for all particles and their daughter particles until they leave the geometry of interest or lose all of their energy. It is clear that in the interaction of photons and electrons, this is a complex model because of their secondary particles, consequently, simulation of all of them will prohibitively increase calculation time. For addressing this problem, the MC simulation defines two parameters, the “production threshold” and “energy cut-off”, which help to reduce the computational time. These parameters will be represented in the following section.

Photon transport

Analog Monte Carlo or “event-by-event” techniques can be used for the simulation of photons and all secondary particles which arise from collision. Analog simulation is usually used for neutral particles and other particles with small cross section and a long mean free path length. The mean free path length λ plays an important role in photon transport. It is the average distance a photon travels in material between two consecutive interactions (Equation 2.8).

$$\lambda = \frac{A}{N_a \rho \sigma_{total}} \tag{2.2}$$

Where A, N_a and ρ are the atomic mass number, Avogadro’s number and the material density, respectively, and σ_{total} is the total cross section which is proportional to the interaction probability.

Generally, the simulation follows the particle to find the position of interaction. After finding the position, the code checks the material of the new position and records it. In the next step, the type of the interaction is simulated. The choice of the each interaction depends on the probability of each interaction which is related to total cross section ($\sigma_{total} = \sum \sigma_i$).

For the case of radiation therapy, the interaction of the photons is limited to the four main interactions outlined above, the photoelectric effect, Compton scattering, pair production and Rayleigh scattering.

Electron transport

MC simulation for electrons is totally different and more complicated than for photons. Photons and other neutral particles deposit their energy at separate points along their mean free path, but charged particles deposit their energy in a near continuous set of interactions because of their electromagnetic field. The mean free path of electrons (positrons) is smaller than photons due to the numerous interactions in the medium. Beside the approximately continuous energy loss of electrons, they have large scattering angles because of their small mass [65].

Interactions of electrons are classified in three categories: soft collisions, hard collisions (knock-on) and nuclear Coulomb field interactions.

When an incident electron passes by an atom, the two parameters classical atomic radius (a) and the distance between the incident electron and the nucleus (b) define the type of electron interaction (Figure 2.11).

- if $b \gg a$, then the collision is considered soft,
- if $b\, a$, a knock-on collision will occur,
- if $b \ll a$, the electron will interact with the nucleus field.

The soft collision is the most probable interaction to occur and electrons deposit 50% of their energies due to soft collisions. Delta rays, X-ray fluorescence and Auger electrons are produced by knock-on collision and X-ray bremsstrahlung is produced via nuclear Coulomb field interaction.

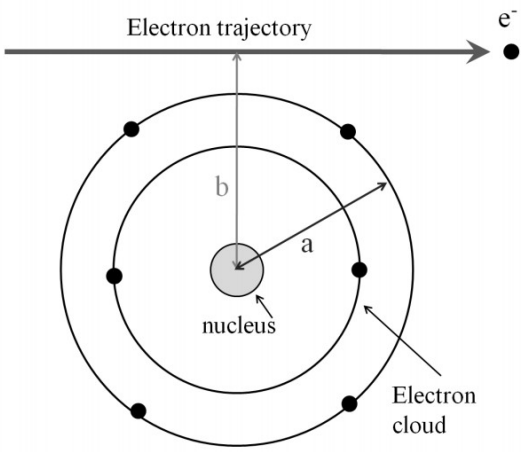

Figure 2.11. Parameters in an electron collision with atom (a is the classical atomic radius and b is the impact parameter) [47].

So an “event-by-event” simulation technique is not suitable for electron interactions due to long computational times to achieve precise physical quantities. For overcoming this problem, most MC codes use a condensed history approach, treating many small interactions as one larger event. Condensed history is a fundamental algorithm to simulate the electron transport which was developed by Berger [9]. This algorithm breaks the electron trajectory into a

series of steps which are named condensed steps (Figure 2.12). In each step, the electron interaction with matter creates small changes in energy and/or direction of the electron.

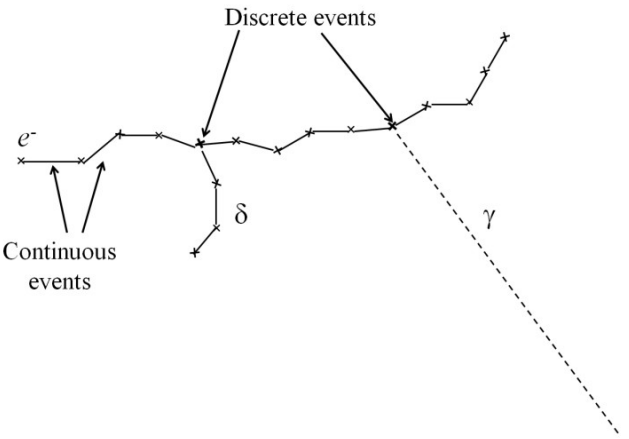

Figure 2.12. Schematic representation of the MC simulation of an electron by successive steps of condensedhistory between points of discrete events resulting in a δ-ray and a bremsstrahlung photon [32].

The entire effect of all these interactions is considered by a condensed step. Generally, the electron interactions in this algorithm are divided into two categories: soft collisions and catastrophic interactions. The soft collisions and their angular deflection in each step are considered by multiple-scattering theory [9, 32, 47].

Catastrophic interactions consider other electron interactions, i.e. secondary particle production, Delta ray and high-energy bremsstrahlung production, independently from the simulation of the primary particle. These interactions produce discrete events (Figure 2.12) and are simulated in two classes which are defined by Berger (1963) [9]. Figure 2.13 illustrates the electron energy algorithms in condensed history, which is according to conservation of energy and momentum on a macroscopic scale.

• **Class I:** this class is used for soft and catastrophic interactions when the secondary particle is produced without changing the primary particle step (energy and direction).

• **Class II**: this class is for catastrophic interactions and implements the condensed history for when the secondary particles' production process changes the energy and direction (angle) of the primary particle.

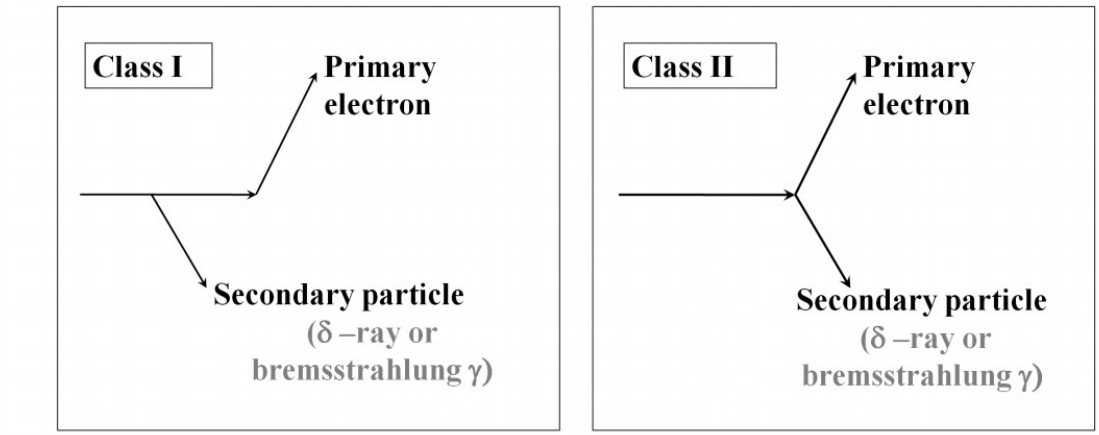

Figure 2.13. Different ways to perform a sampling of electron energy loss, class I (left) and class II (right) algorithms [47].

Variance reduction techniques

Every physical quantity obtained from MC simulation is a random variable with a variance. Low variance is requested in all MC simulations by using variance reduction technique. The variance reduction technique lies at the heart of MC simulation to increase precision of the estimate and improve efficiency of a MC code by reducing calculation time [33].

Several variance reduction techniques, such as photon splitting, electron history repetition, Russian roulette and the use of quasi-random numbers have been proposed to improve the efficiency of MC simulation. It has been demonstrated that it is possible to further improve the efficiency by optimizing transport parameters such as electron energy cut-off, maximum electron energy step size, photon energy cut-off and a cut-off for kerma approximation, without loss of calculation accuracy. In this section, only variance reduction techniques used in this thesis are described [64].

Bremsstrahlung Splitting and Russian Roulette

In the particle splitting technique, secondary particles in a given interaction with weight w=1 split into N secondary particles of different energy and direction. The statistical weight of the new particle is decreased by factor of 1/N. In the simulation of linear accelerators, bremsstrahlung splitting is a good and important example, as that in each Bremsstrahlung interaction a number of photons is artificially produced rather than just one.

Additionally, the Russian roulette is another technique, in which for each particle with statistical weight W_{old} this is used as a survival probability (p), so that the particle is killed with probability (1-p), and its statistical weight is adjusted to the new value:

$$W_{new} = W_{old}\left(\frac{1}{1-p}\right) \qquad (2.\ 2)$$

When Russian Roulette and particle splitting are combined, particles will tend to have nearly equal weights, which is advantageous in reducing the variance in the computed quantity of interest [53]. Directional bremsstrahlung splitting (DBS) is a combination of the splitting technique and Russian roulette.

2.8 Monte Carlo in radiation therapy

There are several codes based on MC simulation for different scenarios and with different program implementations. In the case of radiation therapy, the MC code should be able to consider all aspects of electron and photons transport and accumulate accurate physical quantities in a phantom. EGSnrc, MCNP and GEANT are MC codes which were developed for radiation transport calculations in medical applications.

Geant4 toolkit:

Since the MC codes are very diverse and each of them has a series of advantages and shortcoming, Geant4 was selected as a simulation code in this work.

The wide scope of applications, availability of source code, flexibility in the design of complex geometries, the ability to design animated geometries by using some tricks and support (regular troubleshooting by the code extension team) are some of the benefits of this code compared to the rest of the available codes.

The project of Geant4 (**Ge**ometry **an**d **T**racking) was introduced in 1994 at CERN and the first version of it was released in 1998. The latest version until the writing of this thesis is Geant4_1_03_p01 in mid 2017.

Although the project was originally designed in CERN for high-energy-physics, it was later extendet to other fields of science such as space science, cosmic rays, nuclear physics, and medical applications and even microelectronic scenarios. The concept and uses of this code can be found in its two main references [2, 3].

2.9 General structure of Geant4 and particle transport

In Geant4, everything is considered as an object in the same way as in object-oriented programming and the user needs to create the objects. Here, I give a very short overview of the process and how to transport particles in Geant4.

Construct the detector object:

The whole environment, in which the particle must be transported with all the geometric properties and the materials of that environment, is called the detector. The first step which the user needs to complete the project is to build this object via predefined classes in Geant4.

Construct the primary particle source

For generating a primary event in a Geant4 application, the primary particles have to be generated. The user can create the primary particle in two main ways. According to the characteristics of the required source, either the particle gun class (*G4ParticleGun*) or the general particle source class (*G4GeneralParticleSource*) can be use to generate the primary particle. Both classes are used exactly the same way in Geant4, but there are some differences between them. For example, the particle gun class generates particles with given momentum and position, while the particle source class is able to generate primary particles with spectral and angular distribution.

Define the physics-List

The interaction of particles with matter is described according to the cross sections of their interactions. The production of these interactions and the description of interactions are done by the physics-list object. Finally, the process of manufacturing the detector and the production of cross-sections and particle transport is initiated [24].

Methods to improve system performance in Geant4

Monte Carlo is a very slow method for solving particle transport problems, although with the advent of powerful processors, some of these problems have been solved; but in many cases long simulation times are still a major problem. Hence, some tricks are anticipated for increasing the efficiency of computing systems in the Geant4 toolkit. Parallel processing and multithreading are some methods to decrease the computational time in simulations. In addition, there are variance reduction techniques as outlined above. But in Geant4 there is another approach to optimizing the particle transport which will be explained in the following. Generally Geant4 follows the particle up to zero energy, unless the particle is removed from the environment or destroyed by a process. In some cases, however, to enhance the system and save time on particle transport, the user can ignore particles in an unrealistic way with the use of some techniques and stop the process of tracing without causing any changes in the physical nature of the problem.

- **Range Rejection**

Range rejection discards an electron (as charged particle) if its residual range is smaller than the distance to the nearest boundary to leave the region. Distance to the nearest boundary and range of electrons are calculated in each electron step by predicting the path length travelled until reaching the cut-off energy without any discrete interactions [59]. It should be noted that in regions where the bremsstrahlung process is an important interaction mechanism, e.g. in the target of a medical linear accelerator, range rejection must be turned off [17].

- **Transport cut-off**

This technique is specified with two main parameters; energy cut-off and production threshold energy. Both parameters are threshold energy for transporting particle. Whenever the energy of a particle falls below the energy cut-off, the particle is terminated and its energy is deposited locally [60] and if the energy of the primary particle is below the production threshold, the secondary particle will not be produced and the primary particle will be terminated by depositing the remaining energy locally. Clearly, by increasing these thresholds, the computational time will be decreased. Energy cut-off and production threshold energy can be defined for each type of particle and for each region separately.

➢ **Ignoring Particles**

In this method, contrary to the previous method, particles are produced by various processes, but after production, the user can ignore them and finish the process of transport for these particles. For example, the user can ignore the gamma rays that move in a particular direction or neutrons produced in a given volume with a particular energy and stop the transport process for them. In this case, after ignoring the particle, the user can select one of the 6 possible modes, which are shown in the Table 2.1. For example in the second mode, the particle is stopped and ignored, but processes such as decay can be tracked, and in forth mode, the particle and all its secondary particles are ignored, and their energy is stored locally. The user should note that each of these methods is useful in a particular physical condition and all of them cannot be used everywhere.

Table 2.1. Various possible modes are available for a particle and it's secondary

1	Letting the particle survive and continuing the process of transportation	**fAlive**
2	Invoke active rest physics processes and kill the current particle afterward	**fStopButAlive**
3	Ignoring the particle tranpostion but continuing the transport process for its secondaries	**fStopAndKill**
4	Finishing the transport completely for the particle and its secondaries	**fKillTrackAndSecondaries**
5	Suspend the transport process	**fSuspend**
6	Postpone the transport process to the next event	**fPostponeToNextEvent**

3. Material and Methods

The Siemens Artiste in the mode of the newly introduced flattening-filter-free 7 MV photon beam was simulated inthe Geant4 toolkit using the Monte Carlo method. All details about the geometry and material of the head of linac rely on the information from manufacturer references. The main goal is to extract the physical-dosimetric properties, such as depth dose and dose profile.

Figure 3.1 illustrates the strategy of the simulation and how to extract the physical-quantities step by step, which consists of three separate programs. The first program is the Linac-Headprogramwhich simulates the particle transport in the treatment head including the target, collimators, jaws, ion chamber system, and mirror. The output of this program is a phase space file (PSF) with information on the particle in a phase space scoring plane placed at a distance of 20 cm or 90 cm from the target. The next program is Linac-dose which retrieves the particles from the PSF as source input of the program in order to measure the deposited dose in the water phantom and analyse it. The energy spectrum, particle fluence and angular distribution of photon radiation are analysed by the Linac-Spectrum program. Finally, the output of the Linac-Dose and Linac-Spectrum is compared with experimental data.

While each of these three programs uses special methods and techniques in order to have the best efficiency, they have some common aspects in their classes, such as the definition of the

materials, geometry and type of the physics list. Therefore, first, the common aspects are described and then each program will be investigated separately.

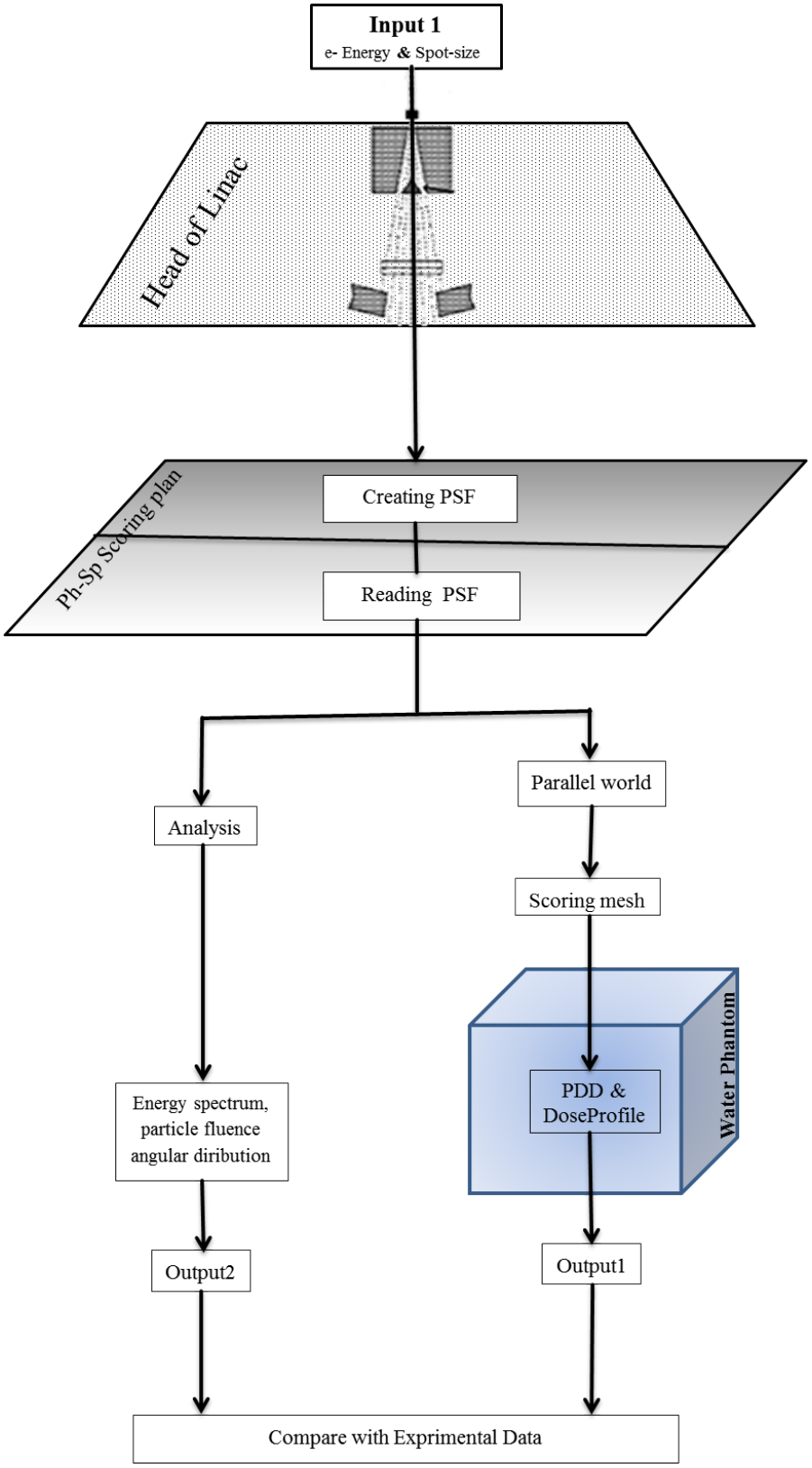

Figure 3.1. Schematic of the strategy of the simulation.

3.1 The common aspects in all simulations

Definition of the Geometry

The detector construction class in Geant4 is one of three mandatory classes in order to model a realistic experiment. In this class, the user should define all the geometry of the experiment with the materials and their spatial position. In Geant4, each geometry is called a solid with individual name, material and position. The existence and definition of a "world volume" in the detector construction is compulsory because it defines the global coordinate system in which all other solids are located.

In our work, all three simulation programs have a common world volume and so have a common coordinate system. All geometries are defined with CGS and Boolean solids in all programs and have the visualization option with some visualization drivers such as the OpenGL and the DAWN event display [4].

Definition of the material

G4Isotope, *G4Element* and *G4Material* are three main classes to design materials in Geant4. Each of these classes has a table of material properties, but only the *G4material* class is used in tracking, the geometry and the physics of simulation.

For the definition of materials the easiest way is using the internal Geant4 database which is derived from the NIST[2] database of elements and isotope compositions. Therefore, in the present work, all materials are defined inthis database.

Definition of the physical model

G4VuserPhysicsList is one of the mandatory classes in Geant4 that defines the all particles and physical processes in the simulation. Based on possible interactions in our simulation, the electromagnetic standard model option3 (*emstandard_opt3*) has been used. The validity of this model is in the range of energy between 1 keV to 100 PeV and it can transport photons and charged particles in this energy range. In this model, electromagnetic processes such as ionization, excitation, multiple scattering and bremsstrahlung radiation for charged particles,

[2] National Institute of Standards and Technology

as well as Compton scattering, photoelectric effects and gamma transformations for photons are formulated.

Also, the value of range cut is defined in the physics list class. In electromagnetic interaction to avoid infrared divergence, some processes required the range cut as production threshold. The range cut is defined for gammas, electron and positrons. The user defines the range cut as a distance and in Geant4 this distance is internally converted to energy (production threshold energy) for each material. In our simulations, the range cut is defined as the default value (1 mm) for all materials in all three programs for gammas, electrons and positrons.

3.2 Linac-Head program

The Linac-Head program simulates the treatment head geometry and transported particles in the treatment head. The most important part of this program is tuning the primary electron beam incident on the target.

The head of the accelerator also has a complex structure, most of its internal components that are not in the beam path are not considered in simulations. Table 3.1 shows the main simulated components which are included with their position and the number of layers of each component. In the following, the simulated components and their operation in the accelerator are described.

Table 3.1. Properties and position of each main simulated component of the treatment head

Component	Distance from zero Point [mm]	Number of layers
Target and exit window	-1.57	10
Primary collimator (and flattening filters)	15.6	4
Ion chamber system	106	5
Mirror assembly	147	1
Pair of jaws	222.5	2

3.2.1 Detector construction class in Linac-Head Program

Target

Accelerated electrons are directed towards the target to generate bremsstrahlung photons. When electrons penetrate into the target, the interactions occur between the incident electrons, target electrons, and protons in the target nuclei. These interactions lead to the production of photons (bremsstrahlung radiation). The optimal target is designed in a way that most incoming electrons are absorbed by the target.

Table 3.2. Target and exit window parameters

Description	**Material**	Thickness of layer (mm)
Exit window	Titanium (Ti)	0.05
	Water (H_2O)	0.66
	Titanium (Ti)	0.05
Target Assembly	Tungsten (W)	0.64
	Nicoro	0.15
	Copper (Cu)	1.65
	Nicoro	0.05
	Stainless steel (SS)	1.02
	Graphite	10.16
	Stainless steel (SS)	0.04

In this accelerator, the target and exit window contain 10 layers of varying thickness of titanium, water, graphite, tungsten, nicoro, copper and stainless steel. The height of this component is about 15 mm and the radius is 3 mm. Constituent elements and thicknesses of each layer are reported in Table 3.2 and Figure 3.2 shows the simulated target and exit window in the Linac-Head program. The abundances of the elements in stainless steel and nicoro are shown in Table 3.3 and Table 3.4, respectively.

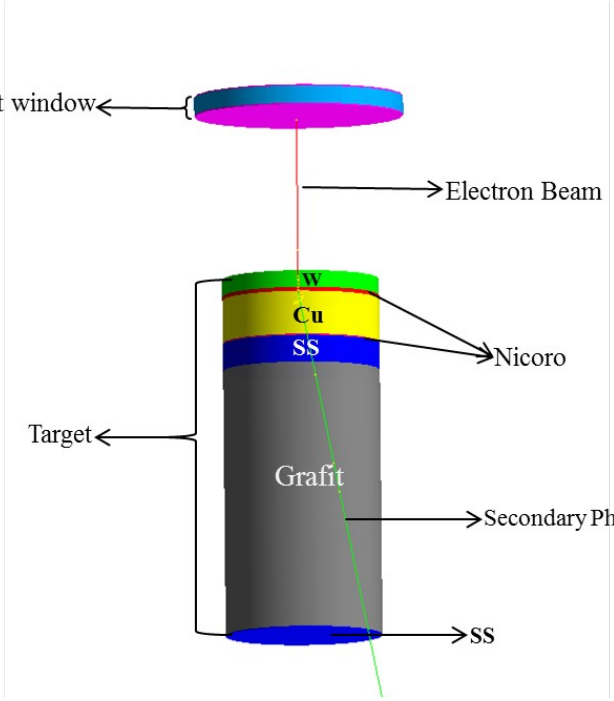

Figure 3.2. The simulated target and exit window in Linac-Head program

Table 3.3. Abundances of the Elements in Stainless steel (density=8.02 [g.cm^{-3}])

Element	% by weight
Nickel (Ni)	10
Silicon (Si)	1
Chromium (Cr)	19
Manganese (Mn)	2
Iron (Fe)	68

Table 3.4. Abundances of the Elements in Nicoro (density=15.6 [g.cm^{-3}])

Element	% by weight
Nickel (Ni)	3
Gold (Au)	35
Copper (Cu)	62

Primary collimator and flattening filter:

The primary collimator is located below the target. This part of the accelerator determines the size of the largest radiation field and since it has a high density, it absorbs the photons that are scattered outside of the desired treatment field. The primary collimator is made of tungsten and is designed as a cylinder with a conical hollow in which the flattening filter is located. The height of primary collimator is about 8.5 cm and the outer radius of cylinder, upper and lower radius of the conical hollow are about 6.2, 0.8 and 2.2 cm, respectively.

Generally, a FF is used to create uniform photon fluence. Besides, it absorbs the lower-energy photons more strongly than the higher-energy photons, so the spectrum is hardened. It also reduces the overall intensity of the photons and reduces the contamination of the photon field by secondary particles. A FF has a conical shape and is made of stainless steel. The height of flattening filter depends on electron energy (Figure 2.6). Simulation of flattening filter was one of challenge in this work. Because there was not any information about the exact height and shape of this component and on the other hand, the energy of flattened beam was also unknown. Therefore, different values of height were implemented in separate programs for probable energies. Also, we were not sure that flattening filter was made of a layer or composed of several layers. So to clarify this, other programs were implemented in addition to the named programs. Figure 3.3 show a schematic of the primary collimator with the FF (for 6 MV photons) in the Geant4 visualization driver.

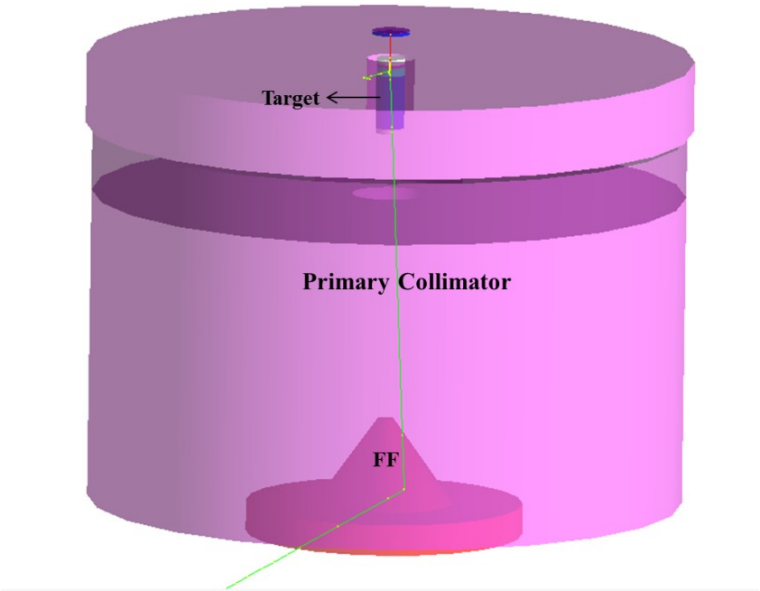

Figure 3.3. The schematic of primary collimator with FF

Ion chamber system:

The radiation delivered by the accelerator is monitored by the ion chamber system. These ion chambers are calibrated in the MU unit in reference conditions. This component involves 5 layers of air and ceramic (Al_2O_3). Table 3.5 shows the arrangement of layers, the location and thickness of each layer, respectively.

Table 3.5. Structure of ion chamber system

Description	Material Traversed by Beam	Distance from zero Point [mm]	Thickness [mm]
Ion Chamber System	Ceramic (Al_2O_3)	106	1.52
	Air	107.5	1.8
	Ceramic (Al_2O_3)	109.3	1.52
	Air	110.8	1.8
	Ceramic (Al_2O_3)	112.65	1.52

Mirror assembly

This part of the accelerator is the simplest part with a rectangular shape, located below the ion chamber. The mirror is made of glass and serves to optically visualize the beam as a light field. This serves for visual beam and field alignment and verification for treatment. The properties of the glass mirror are derived from the NIST database of elements and isotope compositions. In our program, the mirror is placed at 14.7 cm from the coordinate origin with an inclincation of 30° degrees.

Pair of jaws

Under the mirror assembly, there are two pairs of jaws that form the secondary collimator. These jaws are installed in pairs and in two directions perpendicular to the central axis in the beam path. They operate independently and produce rectangular fields with a

maximum dimension of 40×40 cm^2 at the isocenter (distance 100 cm from the target). The jaws are made of Tungsten (W).

Overall, Figure 3.4 shows a complete simulation of the treatment head of the Siemens Artiste in different modes. This geometry is simulated in the detector class of the Geant4. In the next sections, all other part of the Linac-Head program, the primary particle source class, output, and other conditions are investigated.

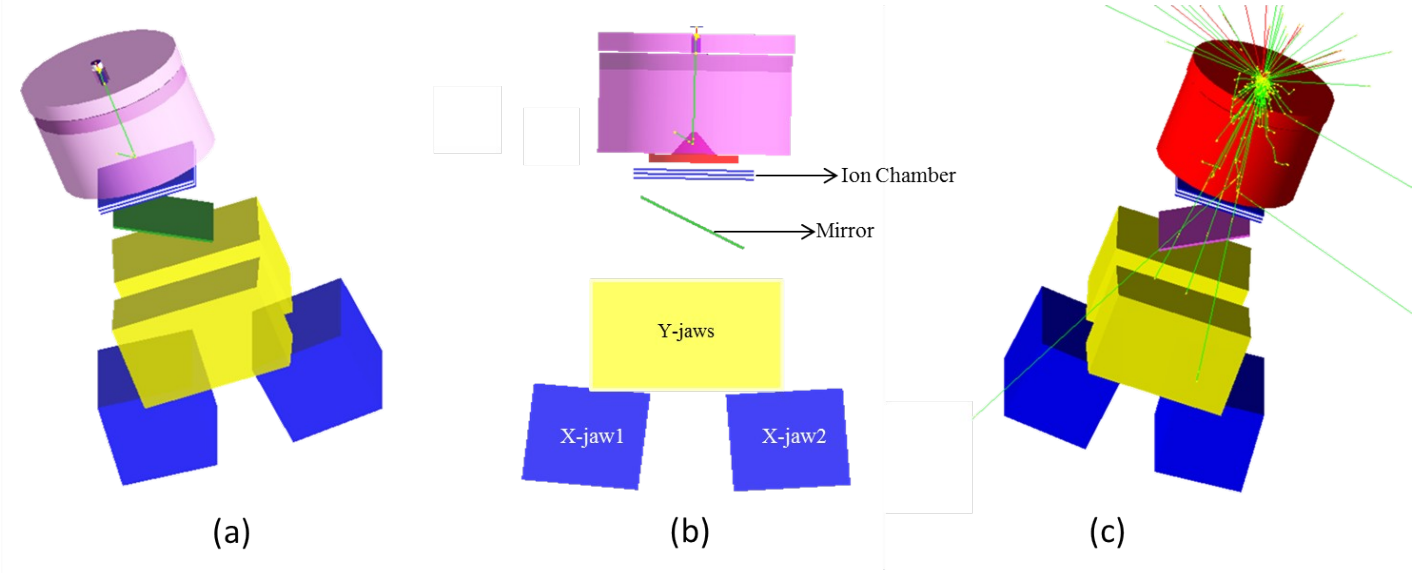

Figure 3.4. View of simulated accelerator head, a) FFF 7XU, b) flat 6 MV, c) transported particle in Geant4

3.2.2 The primary particle source class in the Linac-Head program

Clearly, the primary particle in radiation therapy is the accelerated electron. In Geant4 defining this particle with a given energy is an easy task if its properties are known. However, because of lack of knowledge about exact parameters of the electron beam from the manufacturer, the user needs some technique to define electron beam parameters. These techniques are described in the following section.

Primary Electrons Parameters

Generally, one of the big challenges in the simulation of medical linear accelerators is finding the parameters of the electron beam striking the target, because the spectrum of the electron beam changes with respect to the time after it leaves the factory, so it should be obtained by trial and error. The parameters of the electron beam, such as mean energy, energy spread and spot size should be estimated in the first phase of simulation. Verhaegen and Seuntjens, (2003) [75], suggested three steps for addressing this problem: Firstly, the user can estimate the energy beam and spread energy by matching the measured and calculated depth dose profiles for a 10×10 cm^2 field size. In the next step, by matching the dose profile forvarious field sizes, the spot size can be estimated. Finally in the last step, the program should be again executed with the spot size estimated in the second step in order to calculated depth dose.

In this work, general particle source (GPS) is used for the simulation of the electron beam. For determining the electron beam parameters various program runs were executed with different mean energy, energy spread and spot size. Therefore, according to the energy of linac in FFF 7XU mode, the mean energy was selected in the range from 7 MeV to 9 MeV in 0.1 MeV steps for each independent run. The energy spread ranged from 100 keV to 1 MeV with 100 keV steps. The simulated beam has a 2D Gaussian distribution in the X-Y plane, with full width at half maximum (FWHM) ranging from 0.5 mm to 2 mm.

The example below shows an input micro file of the Linac-Head program which defines a Gaussian beam distribution with 7 MeV mean energy, 1 MeV energy spread and FWHM 1 mm located at (0, 0, -1 cm) and Figure 3.5 shows the electron beam distribution and the vertex position in the X-Y direction of this example.

Noted that, in Geant4 the FWHM and energy spread are defined by the sigma parameter.

```
/gps/particle e-
/gps/direction 0 0 1
/gps/pos/type Beam
/gps/pos/centre 0. 0. -1. cm
/gps/pos/halfx 0 mm
/gps/pos/halfy 0 mm
/gps/pos/sigma_x 1 mm
```

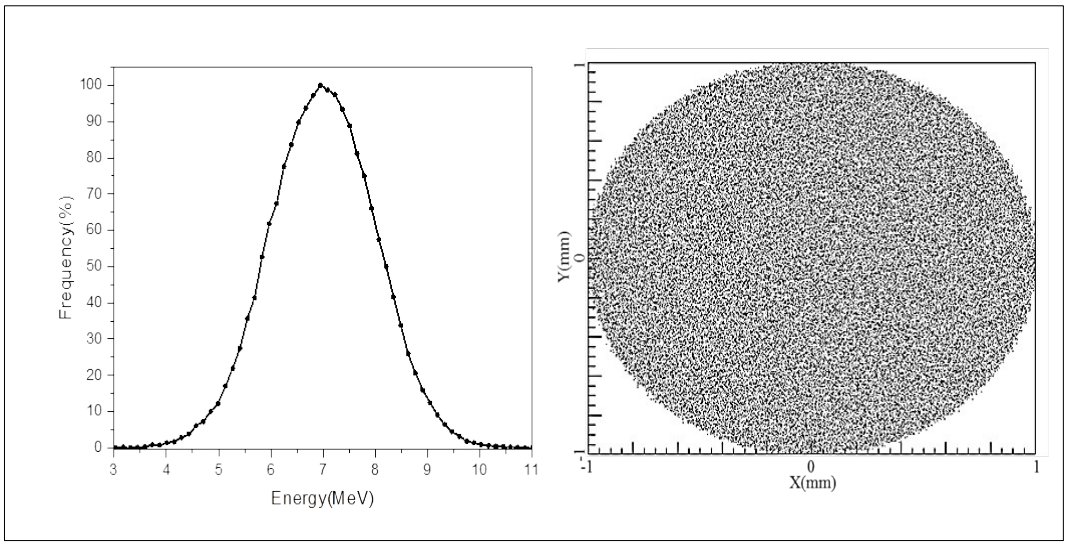

Figure 3.5. Right panel: the electron beam distribution of above example, left panel: the vertex position in the X-Y direction.

3.2.3 Output of the Linac-Head program

The main goal of the Linac-Head program is to create a phase space file (PSF). This file is a collection of photon spectrum properties travelling from treatment head to the phantom or patient. More information about this file is given in the next section.

Phase space file

The PSF records particle properties such the energy, position, direction, charge, particle type and extra variables for any particle passing through the scoring plane which is simulated at a position just below the mirror assembly (20 cm from zero point (z = 20 cm)) or below the jaw at z = 90 cm.

After saving the particle information in a PSF, this file will be used as particle source in the next step of the simulation in the Linac-Dose program to scoring depth dose in a water phantom. This method is known as virtual source model. The main advantage of this method is that the processing is faster than the classic MC simulations and the statistical uncertainty in the dose calculation is increased by reusing the particles from the PSF [29, 67, 39].

Recently, the International Atomic Energy Agency (IAEA) has been working on a PSF databank to establish a freely available public database of phase space data for clinical accelerators and ^{60}Co units used for radiotherapy applications[3]. The IAEA-phsp format has been designed and agreed upon by an international expert committee for its use in medical applications [10], and two classes for writing (*G4IAEAphspWriter*) and reading (*G4IAEAphspReader*) PSFs were defined. These two classes are available on the IAEA-phsp project web site, so these were used in the simulations for this thesis.

The aim of the reader class is to obtain the information of particles in the PSF and use them as particle source in the *G4PrimaryGenerator* class. With the writer class the user can create a PSF in their own Geant4 application. Details of these classes are presented in the following subsections.

[3] https://www-nds.iaea.org/phsp

3.2.4 How to use IAEA PhSp classes in a Geant4 application:

G4IAEAphspWriter is used to write a PSF in Geant4 application. This class simulates a scoring plane at a given position to store the information of particles crossing through it. Particle energy E, statistical weight W, the three components of position (x, y, z), and the direction cosines (u, v, w) are the most important information stored in a binary file of extension ".IAEAphsp". To avoid storing particles passing multiple times through the scoring plane, *G4IAEAphspWriter* stores the information of the particles that pass the scoring plane just only the first time.

In our project, the Linac-Head program was adapted to write IAEA phase space format in two separate executions. Figure 3.6 shows how the Geant4 application was combined with IAEA classes to write the phase space file and shows the relationship between the classes in the Linac-Head and IAEA-phsp classes.

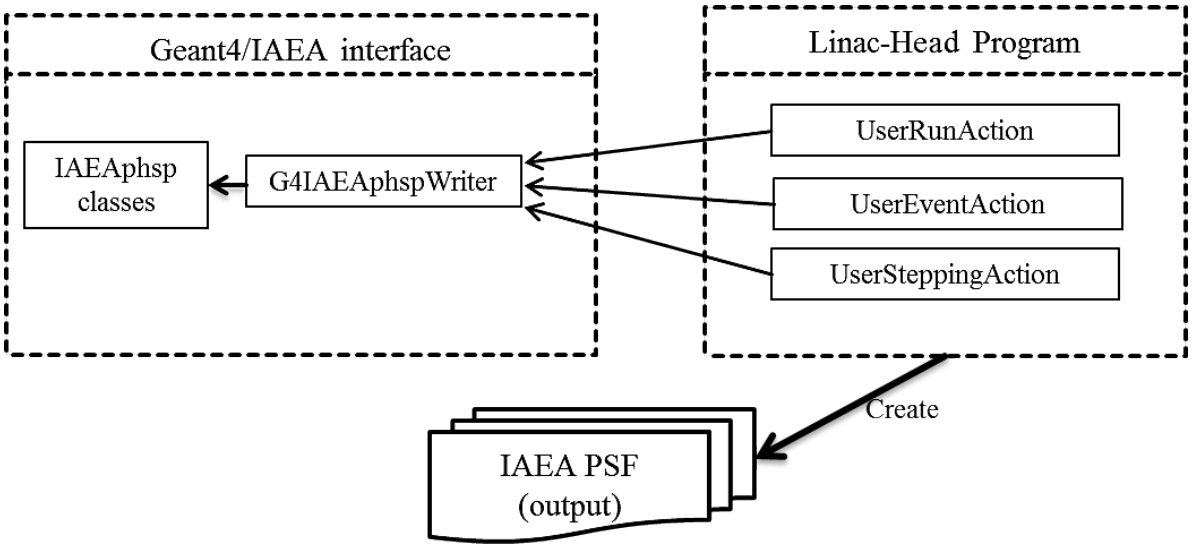

Figure 3.6. The relationship between the classes in Linac-Head and IAEA Ph-Sp classes.

For the using IAEA-phsp classes in Geant4 there is a reference file which the user must download from the IAEA phase space website and this simulation is implemented in a set of read/write routines composed by the following files:

- *iaea_config.hh*
- *iaea_header.hh* and *iaea_header.cc*
- *iaea_phsp.hh* and *iaea_phsp.cc*
- iaea_record.hh and *iaea_record.cc*
- *utilities.hh* and *utilities.cc*

The user must bear in mind that for executing a Geant4 simulation in order to read/write a PSF, all the files listed above must be copied in the directory of the Geant4 application. Likewise, the *G4IAEAphspReader* (.hh and .cc) classes for reading a PSF and *G4IAEAphspWriter* (.hh and .cc) classes for generating a PSF must be copied.

The next step is changing the Linac-Head source code and prepares it for writing an IAEA-phsp file, which is described below.

According to Figure 3.6, for writing a PSF, it is mandatory to have these three classes: "*Run Action*", "*Event Action*" and "*Stepping Action*" in the Geant4 application. Each of these classes should be prepared and adapted with the IAEA-phsp application:

1. in "Run Action" class:

- In *BeginOfRunAction()* method: *G4IAEAphspWriter.hh*, should be obtained to invoke *SetZStop()* method. This method defines the position of the scoring plane in the Geant4 application. For example; we define this scoring plane before the phantom at 90 cm distance from the target (*SetZStop(90*cm)*).
- in *EndOfRunAction()* method : the *EndOfRunAction()* method of the *G4IAEAphspWriter* class must be invoked by means of *G4IAEAphspWriter::GetInstance()*.

The source of the “RunAction” in our simulation is shown below:

RunAction.cc

```
#include"RunAction.hh"
#include"G4Run.hh"
#include"globals.hh"
#include"G4IAEAphspWriter.hh"
#include"G4SystemOfUnits.hh"
#include"G4PhysicalConstants.hh"

RunAction::RunAction()
{}
RunAction::~RunAction()
{}
voidRunAction::BeginOfRunAction(constG4Run*aRun)
{
G4IAEAphspWriter*IAEAWriter=G4IAEAphspWriter::GetInstance();
IAEAWriter->SetZStop(90.0*cm);
IAEAWriter->BeginOfRunAction(aRun);
}
voidRunAction::EndOfRunAction(constG4Run*aRun)
{
G4IAEAphspWriter::GetInstance()->EndOfRunAction(aRun);
}
```

2. In“Event Action” class: in this class the user just needs to invoke the *G4IAEAphspWriter* class in the *BeginOfEventAction()* method, as can be seen in the “Event Action” source below:

EventAction.cc

```
#include"EventAction.hh"
#include"G4Event.hh"
#include"G4IAEAphspWriter.hh"
EventAction::EventAction()
{}
EventAction::~EventAction()
{}
voidEventAction::BeginOfEventAction(constG4Event*aEvent)
{
G4IAEAphspWriter::GetInstance()->BeginOfEventAction(aEvent);
}
```

3. In“Stepping Action” class: the user must to invoke the *UserSteppingAction()* method of *G4IAEAphspWriter*.

SteppingAction.cc

```
#include"SteppingAction.hh"
#include"G4Step.hh"
#include"G4IAEAphspWriter.hh"

SteppingAction::SteppingAction()
{}
SteppingAction::~SteppingAction()
{}
voidSteppingAction::UserSteppingAction(constG4Step*aStep)
{
G4IAEAphspWriter::GetInstance()->UserSteppingAction(aStep);
}
```

Finally, with this structure, the user can create a PSF. As mentioned, scoring plans were placed at z=20 cm or z=90 cm in order to monitor the photon spectrums across their trajectory.

3.3 Linac-Dose program

The role of the Linac-Dose program is to estimate the deposited dose in the water phantom. This program estimates the percent depth dose and dose profile as a function of depth in the phantom. For extracting the output, parallel worlds and parallel navigators are used, which reduces the computational time considerably. All details about this program are described in this section.

3.3.1 Detector construction class in Linac-Dose

The detector construction in Linac-Dose has a simple structure. If the scoring plane is located at z=20 cm, the geometry includes the jaws and water phantom and if the scoring plan is at z=90 cm the geometry just includes the water phantom.

The material, shape, and position of the jaws have been considered in the previous section. The water phantom has a rectangular shape with dimensions $30\times30\times30$ cm^3 filled with water and the distance between the upper surface of water phantom and the surface of the target (SSD) is 100 cm.

3.3.2 The primary particle source class in Linac-Dose

In Linac-Dose, the primary particle source is the PSF that was created in the Linac-Head program. Each recorded particle in the PSP is again retrieved as a particle source in this step. Therefore, in this step, we need the *G4IAEAphspReader* class.The *G4IAEAphspReader* class works like other primary particle generators, for example *G4ParticleGun* and *G4GeneralParticleSource*, which are derived from *G4PrimaryGenerator* virtual class.

The main utilities in *G4IAEAphspReader* are:

- Keeping correlations between particles is vital in GEANT4 for a correct statistical analysis. There are two types of correlations: a) when particles come from same original history, and b) when the same particle is recycled several times to increase statistics.

Geant4 keeps this correlation by generating all correlated particle in the same Geant4 event, this means that one Geant4 event represents one independent event which does not correspond to one unique particle. Therefore, all the particles that share same original history are storedin the same event. In addition, in case of recycling, each particle would be repeated the desired amount of times, always in the same Geant4 event. The user can recycle particles by means of *SetTimesRecycling (G4int n)* method, where n indicates that each particle will be used (n+1) times [13]. Consequently, in each GEANT4 implementation in order to read a PSF, the user can recycle particles to achieve the best statistical output, which is the best way to reduce computation times and improve the simulation efficiency.

- *SetTotalParallelRuns (G4int m)* methods can divide the PSF into m fragments and prepare parallel runs in different CPUs.
- *G4IAEAphspReader* has the ability of translation or rotation of the phase-space plane. For example, the user can rotate the phase-space plane around the direction of the rotation axis of the gantry.

3.3.3 How to read an IAEA-phsp file

The next step after writing and generating an IAEA-phsp file is reading the information stored in the PSF and using them as a particle source to find the deposited dose in the Linac-Dose program. As mentioned before, in the writing step of the simulation the scoring plane was positioned at z=90 cm or z=20 cm. Therefore, the particles which were stored in the PSF are emitted from this position onto the phantom. Figure 3.7 shows how the Geant4 application was combined with the IAEA classes to read the PSF and shows the relationship between the classes in Linac-Dose and IAEA-phsp classes.

For executing this step of simulation the user applies the following requirement in the “Primary Generator” class:

1. In the first step the *G4IAEAphspReader* must to be a data member of the *Primary Generator* class, so a pointer should be added to *G4IAEAphspReader* in the header file of Primary Generator class (*PrimaryGeneratorAction.hh*),

2. Declaring a pointer in the “Primary Generator” class and passing the name of the PSF as an argument (without including the IAEA extension) to use the PSF information,

3. In the *GeneratePrimaries()* method of the Primary Generator class, the pointer to the*G4IAEAphspReader* object must be used to invoke the *GeneratePrimaryVertex()* method.

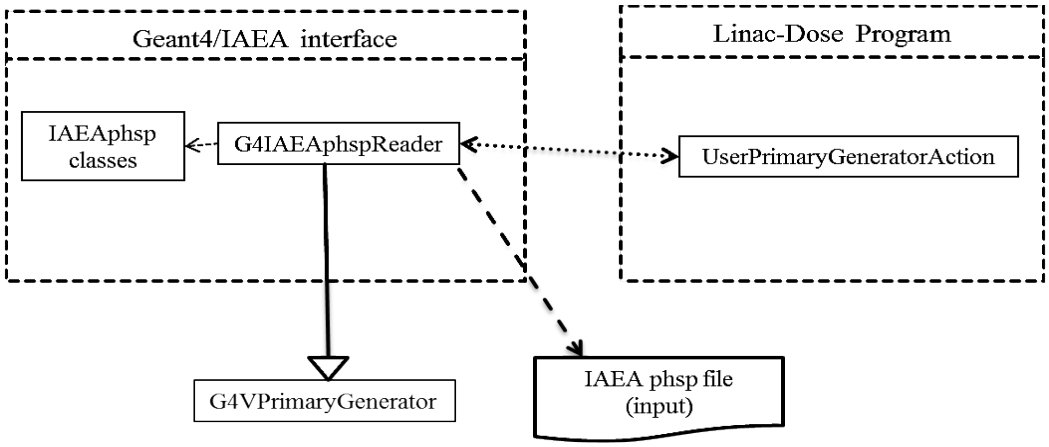

Figure 3.7. The relationship between the classes in Linac-Dose and IAEA phsp classes

These three steps are the minimum requirement for implementing a simulation. Besides these, the *SetTimesRecycled()* method was used for recycling particle 90 times from the PSF to improve the statistics. In the following lines, the header and source file of the “Primary Generator” class are shown.

PrimaryGeneratorAction.cc

```
#include"PrimaryGeneratorAction.hh"
#include"G4Event.hh"
#include"G4IAEAphspReader.hh"

PrimaryGeneratorAction::
PrimaryGeneratorAction()
{
G4StringfileName="PSF_900";
theIAEAReader=newG4IAEAphspReader(fileName)
;
theIAEAReader->SetTimesRecycled(89);// particles
used 90 times
}
PrimaryGeneratorAction::~
PrimaryGeneratorAction()
{
if(theIAEAReader)deletetheIAEAReader;
}
voidPrimaryGeneratorAction::GeneratePrimaries(
G4Event*anEvent)
{
theIAEAReader-
>GeneratePrimaryVertex(anEvent);}
```

PrimaryGeneratorAction.hh

```
#ifndefRE03PrimaryGeneratorAction_h
#defineRE03PrimaryGeneratorAction_h
1
#include"G4VUserPrimaryGeneratorAct
ion.hh"
classG4Event;
classG4IAEAphspReader;
classRE03PrimaryGeneratorAction:pub
licG4VUserPrimaryGeneratorAction
{
public:
RE03PrimaryGeneratorAction();
~RE03PrimaryGeneratorAction();
voidGeneratePrimaries(G4Event*);
private:
// Phase space reader
G4IAEAphspReader*theIAEAReader;
};
#endif
```

3.3.4 Output of Linac-Dose

Percentage depth dose and beam profiles are two important output results obtained from the Linac-Dose program. In the following sections, these outputs are explained and then in the last section, the technique of extracting these data from the simulation by the command-based-scoring method is presented.

Percentage depth dose curve (PDD):

In radiation therapy, the absorbed dose of photons changes with depth in the body. The region between the phantom surface and the depth with a maximum dose is called the dose build-up region. The formation of this region is due to high-energy secondary electrons created in the phantom surface layers which deposit their energy at a considerable distance from the source of their production. As the secondary electrons created in a high-energy photon beam have a significant range in the material, they are effectively removed from the surface layers to a slightly deeper part of the phantom, where the dose is deposited. Therefore, in the phantom surface layers, there is no electron balance, and the electron flux and the absorbed dose increase with depth to the maximum point, after which electron balance exists: now the number of electrons entering each depth slice (from shallower parts of the phantom) equals the number of electrons exiting the slice to deeper parts of the phantom. The build-up effect is clinically advantageous because less dose is given to the skin surface, which is mostly not the target of the radiotherapy (skin-sparing effect).

According to the law of absorption, the flux of the incident photons decreases exponentially with the depth of the phantom, with an additional decrease due to the geometry (inverse square-law). By decreasing the photon flux with depth, the production of secondary electrons also decreases and after reaching the maximum dose, the dose accordingly begins to decrease. Typical photon depth dose curves are shown in Figure 3.8.

Figure 3.8 shows that the dose build-up effect increases with photon energy. As can be seen, with the increase in photon energy, due to the longer range of the secondary electrons that are produced, the depth at which the maximum dose is deposited is also increased. For photons with energies of several MV, the surface dose is much less than the maximum dose.

Of course, the variation of dose in the depth, in addition to the type and the energy of the particles, depends on the source surface distance (SSD). The depth dose curve is an important property of clinical photon beams and must be accurately known and modelled for radiotherapy treatment planning.

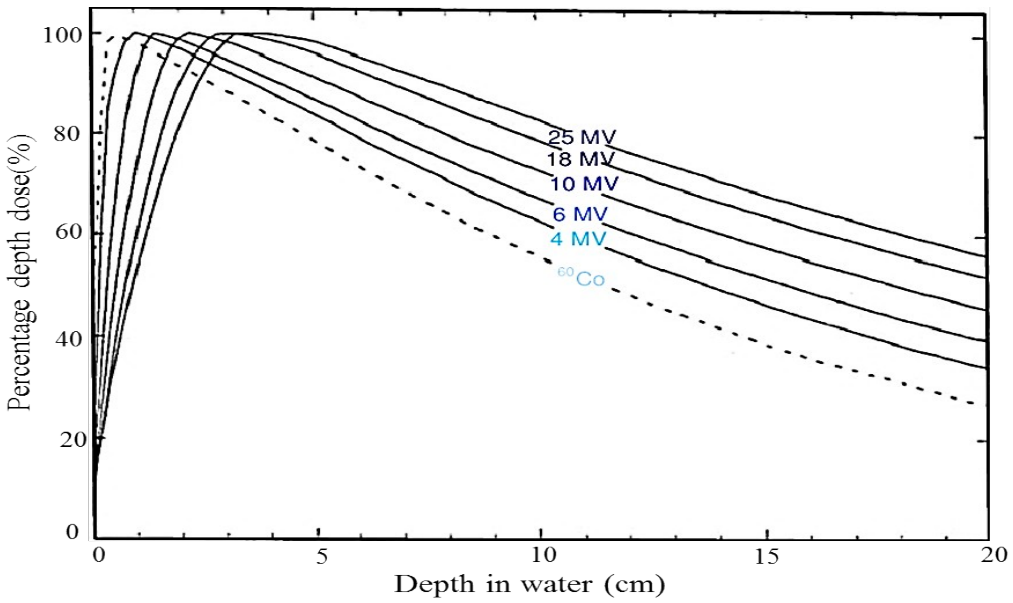

Figure 3.8. Percentage depth dose curves in water for a 10 × 10 cm^2 field for photon beams ranging from cobalt-60 gamma rays to 25 MV X-rays [45].

In all simulations of PDDs the PSFs were placed at z=20 cm (before jaws) and all information of these files were read by *G4IAEAphspReader(.hh* and *.cc*) classes. It is necessary to mention, for obtaining an average standard deviation below 2%, all simulation had a minimum requirement of 30000 particles per cell; therefore, 1.5×10^9 histories were enough to attain acceptable statistical uncertainties in the PDDs curves.

All outputs were stored in a text file and were then analyzed with *OriginLab* to plot all curves. In each PDD curve, the dose is normalized to 100 % at the depth of maximum dose as follows:

$$PDD = \frac{D_d}{D_{max}} \times 100 \qquad (3.\ 1)$$

where the D_d is the deposited dose at depth of d and the D_{max} is maximum deposited dose on the central axis.

Beam Profiles:

Another curve that is usually measured when working with linear accelerators and which is also implemented in the treatment planning system is the beam profile. These curves are required along with the percentage depth dose curves to calculate the 3D dose distribution. Beam profiles measured at different depths and field sizes perpendicular to the central axis are known as OAR (off-axis ratio) and are defined as the ratio of doses at a given distance from the beam central axis to the doses along the center axis at the same depth.

In the present work the beam profile of FFF beam and also the flat 6 MV beam were calculated at various depths in the water phantom to have best comparison with measurements. To show simulation validation the profile beam were calculated at depth of maximum dose (D_{max}) which was 19 mm for the FFF and 16 mm for the flattened beam and for comparing the both modalities of linac this curve was calculated at depth of 10 cm in water phantom. Similar to PDD curves, 1.5×10^{9} histories were enough to have an average standard deviation below 2%.

In contrast to the PDD curves, the normalization of FFF beam profiles is a little more complicated especially when the results of FFF beam should be compared with flattened beam and also for defining some quantities such as dosimetric field size, flatness, symmetry and penumbra (in following, these quantities will be explained completely).

Some studies, i.e. Pönisch et al., 2006 [52], used the inflection point (a point at the field edge when the second derivative is null) to renormalize the FFF beam. But there is a considerable uncertainty by using this method [21]. Fogliata et al., 2012 [21], suggested an alternative normalization point (shoulder point) with better uncertainty. The diamond symbol in Figure 3.9a shows the shoulder point. According to this figure, the two flattened and FFF beam have a similar shape before the shoulder point and after this point the FFF beam stars to increase toward the central axis.

Fogliata et al., 2012 [21], determined the shoulder point with following procedure:

- The flattened profiles should be normalized to their respective maximum value on the central axis.
- The third derivative should be computed in the penumbra region.

- The relative dose on the flat 6 MV profile corresponding to the off-axis position of the second maximum for the left profile edge—closer to the central axis—(first minimum for the right profile edge) is used to normalize the FFF beam profile at the same off-axis position (diamond symbol in Figure 3.9a) [21].

- – The relative dose at the FFF beam central axis is the
- renormalizati on value (circle symbol in Fig.
- 2).

When the FFF profile is renormalized, it becomes comparable with the corresponding flattened profile, because with this normalization they have the same dose level [21]. Figure 3.9b shows some of the beam parameters such as:

- Dosimetric field size: the distance between the half percent dose level [21].
- Penumbra: the distance between the positions of the 20% and the 80% normalized dose with above method in the field edge [52, 21].
- Field region: the area within 80% of the field when the profile has been normalized [21].
- Unflatness: Equation 3.2 formulates the unflatness of the FFF beam profile.

$$Unflatness = \frac{D_{CAX}}{D_{OA}} \tag{3. 2}$$

D_{CAX} is the normalized dos at central-axis and the D_{OA} is the dose at the edge of 80% field size [52, 21].

- Slope: The shape and dose level of FFF profiles strongly depend on the energy, therefore the slope parameter is used for defining the shape and left/right inclination of FFF beam [21, 22]:

$$Slope = \frac{D_1 + D_2}{x_1 - x_2} \tag{3. 3}$$

where x_1 and x_2 being two points at 1/3 and 2/3 of the half beam, respectively, and D_1 and D_2 the normalized doses at x_1 and x_2, respectively [22].

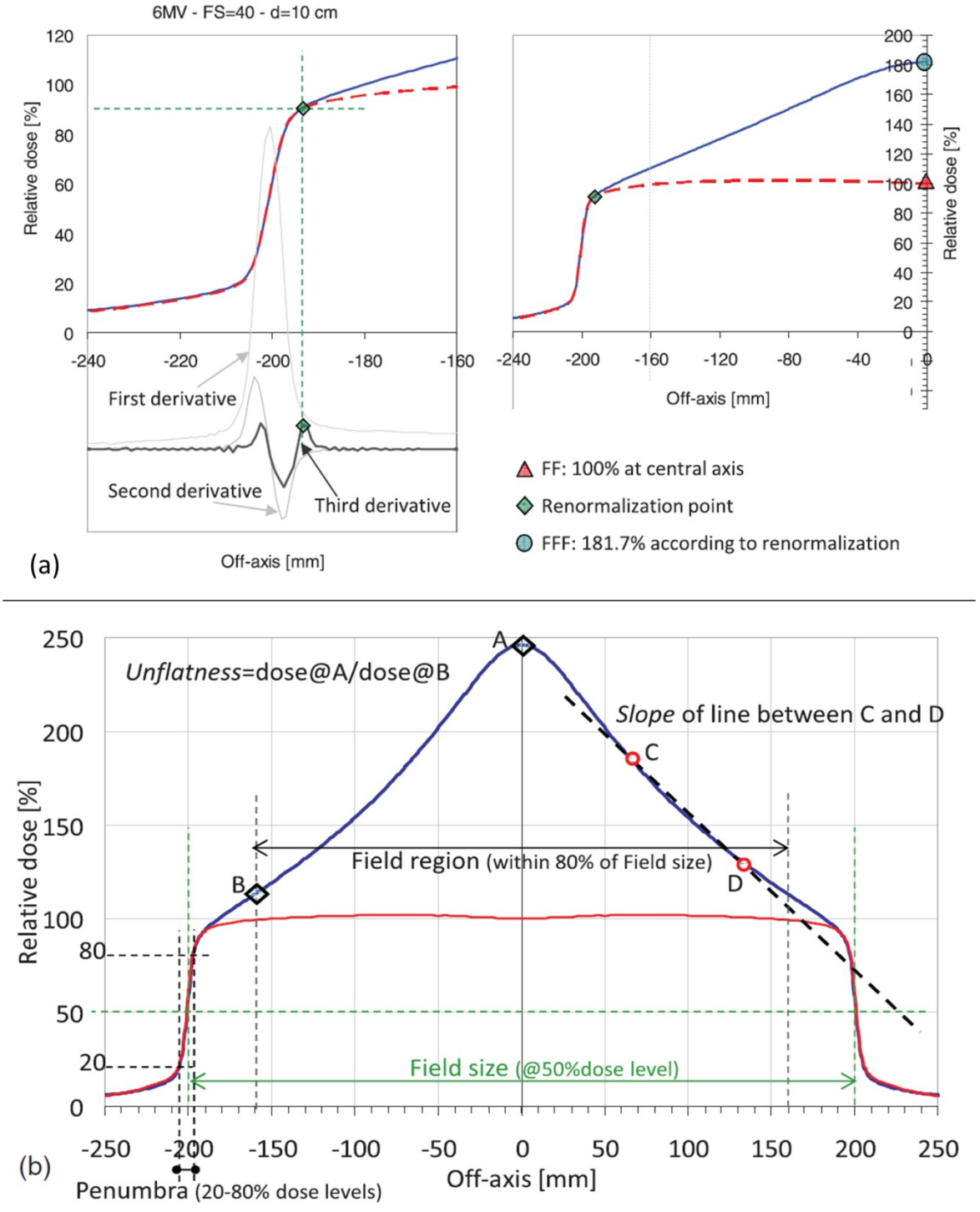

Figure 3.9. a) Renormalization point obtained through the profile third derivative FFF (solid line) and Falttened beam (dashed line),b) schematic description of some of the beam parameters: field region, field size, penumbra, unflatness, and slope. Point A: central axis; point B: off-axis at 80% of the field size (edge of field region); point C: off-axis at 1/3 of the field size; and point D: off-axis at 2/3 of the field size. [21].

3.3.5 Command-based-scoring

In Geant4, after the simulation of the geometry, physics and cross-sections of interactions, and primary particle generation, the user has to extract useful physical quantities by using some code or method.

In our project, as we are not interested in recording each individual *step* information, a command-based-scoring method is used. In this method for accumulating physical quantities, visualizing and dumping scores into a file, the user uses an interactive command to create a parallel world defining a 3D scoring mesh with given size. This method has the ability to define several scoring volumes without any anxiety about volume overlap or mass [5].

Table 3.6. The list of the physical quantities in command-based-scoring

Scoring quantity	**Physics quantity**
energyDeposit *	Energy deposit scorer.
cellCharge *	Cell charge scorer
cellFlux *	Cell flux scorer
passageCellFlux *	Passage cell flux scorer
doseDeposit *	Dose deposit scorer.
nOfStep *	Number of step scorer.
nOfSecondary *	Number of secondary scorer.
trackLength*	Track length scorer
passageCellCurrent*	Passage cell current scorer.
passageTrackLength *	Passage track length scorer.
flatSurfaceCurrent *	Flat surface current Scorer.
flatSurfaceFlux *	Flat surface flux scorer.
nOfCollision *	Number of collision scorer
population *	Population scorer.
nOfTrack *	Number of track scorer.
nOfTerminatedTrack *	Number of terminated tracks scorer.
command-syntax: /score/quantity/“*Scoring quantity*” “*scorer_name*“ “*unit*”	

In addition to this, after scoring the physical quantity such as dose, flux, etc., the user can add different filters to them such as for charged particles, kinetic energy, etc. In Table 3.6 and Table 3.7, the list of the physical quantities and filters with their command-syntax in the interactive command file are shown.

Table 3.7. List of the filters in command-based-scoring

Scoring Filter	filter
charged *	Charged particle filter
neutral*	Neutral particle filter
kineticEnergy *	Kinetic energy filter
particle*	Particle filter
particleWithKineticEnergy*	Particle with kinetic energy filter

command-syntax: /score/filter/*"Scoring Filter"*

How to adapt Geant4 to using command-based-scoring:

Command-based scoring is an optional functionality so the user needs to explicitly define its use in the *main()* program. To do this, the method *G4ScoringManager::GetScoringManager()* must be invoked right after the instantiation of *G4RunManager* [24]. This change in *main()* is enough to enable the simulation for command-based-scoring and read each command inserted into the program.

The next step is defining a scoring mesh. To do this, user needs to:

- define the shape and name of the 3D scoring mesh
- give the size of the scoring mesh
- define the number of bins for each axis
- optionally, define the position and rotation of the mesh.

Currently, box and tube are available for the shape of the mesh and the user must bear in mind that the size of the mesh is specified as “half width”. Bin numbers define the number of the

cell in each mesh, which has an influence on the spatial resolution, but also on memory consumption and computational time. After defining the mesh score, the user can address the program to accumulate and dump the physics quantities. As said before, all of these informations are inserted in the interactive command file with a special command-syntax.
An example of an input macro file in the Linac-Dose program is shown below, showing all the construction of the command-syntax. These commands define two mesh scoring, named "boxMesh_1" and "boxMesh_2", in water phantom. For scoring the PDD, "boxMesh_1" has the same size of the water phantom and is then divided into 5×5×5 mm^3 cells by the number of bins.

/score/mesh/translate/xyz command defines the position of the scoring mesh in the world volume. */score/quantity/doseDeposit dDep1* accumulates the dose in each cell and the */score/dumpQuantityToFile* command dumps all the information of deposited dose in a file named "PDD.txt".

```
/run/initialize
########################################
/score/create/boxMeshboxMesh_1
/score/mesh/boxSize 15. 15. 15. cm
/score/mesh/translate/xyz 0. 0. 115. cm
/score/mesh/nBin 60 60 60
/score/quantity/doseDeposit dDep1
/score/close
########################################
/score/create/boxMeshboxMesh_2
/score/mesh/boxSize 15 0.25 0.25 cm
/score/mesh/translate/xyz 0. 0. di cm
/score/mesh/nBin 60 1 1
/score/quantity/doseDeposit dDep2
/score/close
########################################
#Dump scores to a file
/score/dumpQuantityToFile Phantom dDep1 PDD.txt
/score/dumpQuantityToFile Phantom dDep2 PB.txt
```

The "boxMesh_2" is defined to estimate the beam profile in the given depth (d_i) of the water phantom. The "boxMesh_2" has dimension of 15×0.25 ×0.25 cm^3 which is divided to 60 cells in the direction of the x-axis. Then, the beam profile data is dumped into the file named "PB.txt".

3.4 Linac-Spectrum Program

To evaluate the spectrum of bremsstrahlung radiation photons and their energy, angular distribution and fluence, the linac-Spectrum program is executed at different positions in the beam path. The linac-spectrum program is used to analyse the spectrum produced in the linear accelerators. As we know, when the bremsstrahlung photons are produced, they pass different components of the linac which individually change the features of the spectrum. With this section of the simulation, it is possible to monitor the spectrum in each step of the beam path and then examine the effect of each component on the spectrum.

This program has a simple construction and the primary particle source is the PSF obtained from Linac-Head in the different position. This means, first the PSF is written by Linac-Head and then Linac-Spectrum analyses the information on theparticles stored in the PSF. The output is the particle fluence (Φ) and energy fluence (Ψ).

Particle Fluence (Φ), Energy Fluence (Ψ):

In order to evaluate the secondary particles produced in radiation therapy, we need to know the average number of particles passing through a specific surface, which is called fluence. It is determined in the Monte Carlo method by multiplying the weight of the desired particle by the total sum of all step lengths per volume:

$$Fluence_i = \frac{w_i}{V} \sum_{Steps} StepLenght_i \qquad (3.4)$$

In which the fluence of each particle is usually expressed in $\frac{Number}{cm^2}$ unit and the step lengths of the desired particle in that volume are summed in each event.

The energy fluence spectrum describes the amount of energy that enters the sphere of area A, accounting for the different energies of the representative particles, with unit of MeV/cm^2.

3.5 Measurement Method

The depth dose and profile beam data were measured in a PTW MP3 (PTW, Freiburg, Germany) water phantom using a Semiflex ionization chamber (PTW 31010) which has a sensitive volume of 2.75 mm^3. All measurements for the field size of 10×10 and 20×20 cm^2 were performed at source to surface distance of 100 cm. Measurements were recorded in 1 mm steps using the PTW Verisoft system.

The beam profiles were obtained for four different depths (1.9, 5, 10 and 20 cm for FFF 7XU; 1.6, 5, 10 and 20 mm for the flat 6X beam line). Figure 3.10 illustrates the PTW MP3 and ionization chamber used in our measurement.

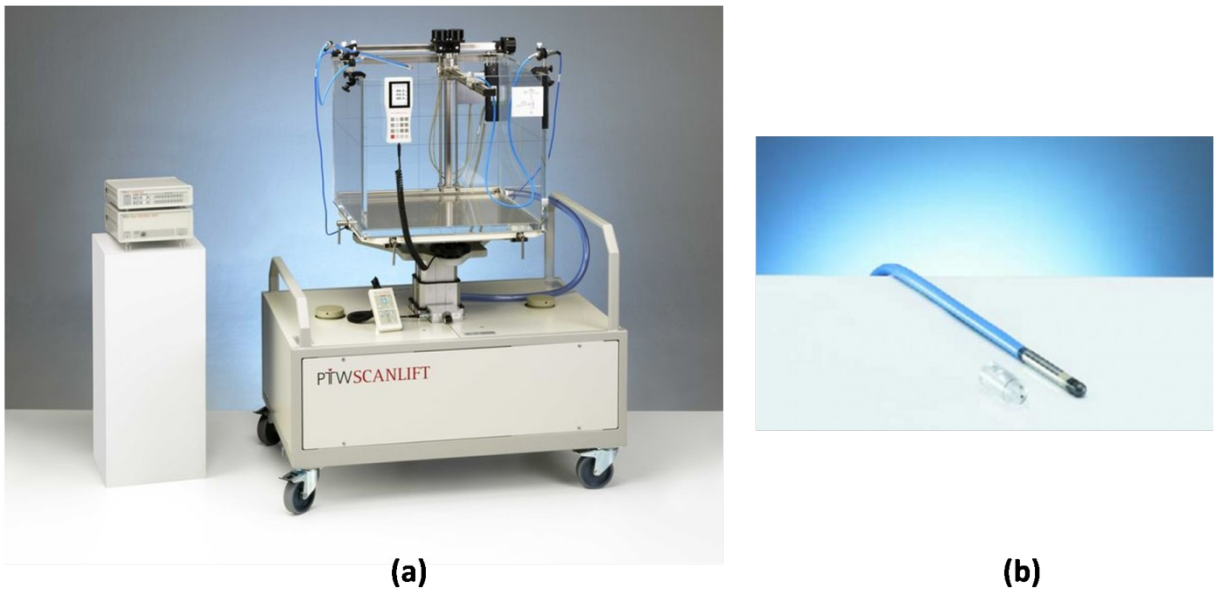

Figure 3.10. a) PTW MP3 (PTW, Freiburg, Germany) water phantom, b) Semiflex ionization chamber (PTW 31010) [57, 58].

4. Results

The flattening-filter-free beam energy 7 MV (FFF) of the Siemens Artiste medical linear accelerator and the corresponding 6 MV flat beam line were modelled using Monte Carlo method. The geometry of the head of the linac includes target, primary collimator, and jaws; for the 6 MV beam, the flattening-filter was added to the aforementioned geometry. All calculated and measured data were acquired in water phantom.

All simulation were performed by Geant4 _10_03 based on a system Intel Core i3-4130 CPU, 3.40 GHZ processor and a system intel Core i3-2100 CPU, 3.10 GHZ processor.

In order to reduce computational time, the simulation was carried out in two phases with generating and reading phase-space files at different distances from the target. Russian roulette was turned off and photon cut-off energy (PCUT) and electron cut-off energy (ECUT) and threshold for secondary particle were applied in simulations as variance reduction techniques. PCUT and ECUT value were set to their default value (1 mm). The secondary particle threshold was set to ECUT for charged particle and PCUT for photons.

The command-based-scoring method was used for the calculation of the dose distribution in the water phantom, placed at SSD 100 cm. In this method, the water phantom was voxelized by number of bins to divide the volume into cells (voxels) of $5\times5\times5$ mm^3 to acquire the PDDs and dose profiles curve.

The present chapter includes selecting the primary electron parameters, the characteristics of the photon beams such as PDDs, dose profile and photon energy spectra of the flat 6 MV and FFF 7 MV configurations. Finally, photon beam characteristics were investigated as a function of off-axis distance (OAD). First, results for the FFF 7 MV beam are presented, secondly, the 6 MV flat beam is investigated.

4.1 Primary Electron Beam Parameters (simulation validation)

The validity of the Monte Carlo method depends on fine-tuning electron beam parameters to have the best match between measurements and simulation. The mean energy value, spread energy and spot size (FWHM) of the Gaussian electron source are three electron beam parameters which were tuned by the Verhaegen and Seuntjens, 2003 [75], method. According to this method, the mean energy and spread energy value are defined by matching calculated PDDs curves with the measurements and after finding the optimal mean/spread energy value, dose profiles are using to select the best spot size (FWHM).

Therefore, in the first step, more than 40 simulations were carried out with different mean energy (from 7 to 9 MeV with step of 0.1 MeV) and the spread energy (from 100 keV to 1 MeV in 100 Kev steps) in order to compare their PDDs with the reference data set. As mentioned, the FWHM was an arbitrary constant number (for example 0.4 mm) at this stage of the program because this value does not influence the PDD curve.

In Figure 4.1, when the mean energy is 8.6 MeV the calculated data do not match with experimental data especially in the tail of the PDD curve, such that the difference in this area is about 3%. The peak of 8.7 MeV shows that this energy is still less than the optimal mean energy of the electrons. Conversely, for the 8.9 MeV PDD curve the high dose values in the tail region illustrate that 8.9 MeV is larger than the optimal mean energy. Noticing this result, 8.8 MeV as primary electron mean energy (with energy spread of 0.4 MeV) offers the best match with an absolute difference of less than 1% in all regions of the curve.

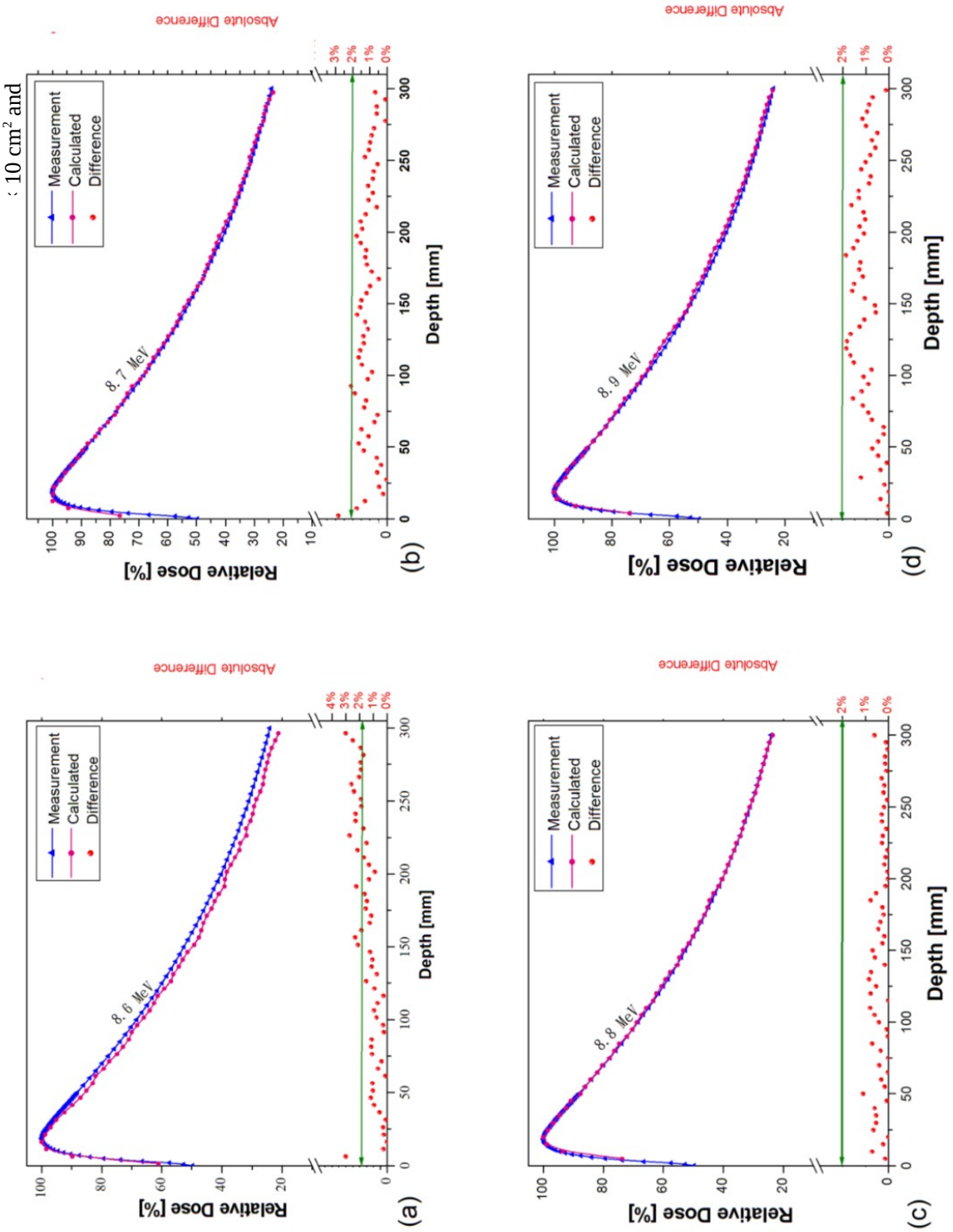
10 cm² and
Measurement
Calculated
Difference
8.7 MeV
8.6 MeV
8.9 MeV
8.8 MeV
Relative Dose [%]
Depth [mm]
Absolute Difference
(a)
(b)
(c)
(d)

Afterwards, a significant number of simulations were implemented to select the spot size of the electron source. In these simulations, dose profiles were calculated with a set of spot sizes from 0.5 mm to 2 mm at a depth of 19 mm for a field size of 10×10 cm^2. Dose profiles were normalized to their maximum value (as 100%) on the central axis. Figure 4.2 shows the dose profile for FFF beams with 10 cm square field size of 8.8 MeV mean energy, 0.4 MeV energy spread and a) 0.5 mm, b) 1 mm, c) 1.5 mm, and d) 2 mm spot size. Figure 4.2 shows that the penumbra of the dose profiles depends strongly on the spot size of the source. The penumbra region is increased directly by increasing the spot size. It is clear that the FWHM of 1 mm achieves the best match with the measurement data in all regions of the profile, and all points have a deviation less than 2%.

Ultimately, mean energy, spread energy and spot size of the selected Gaussian electron distribution source were 8.8 MeV, 0.4 MeV and 1 mm, respectively.

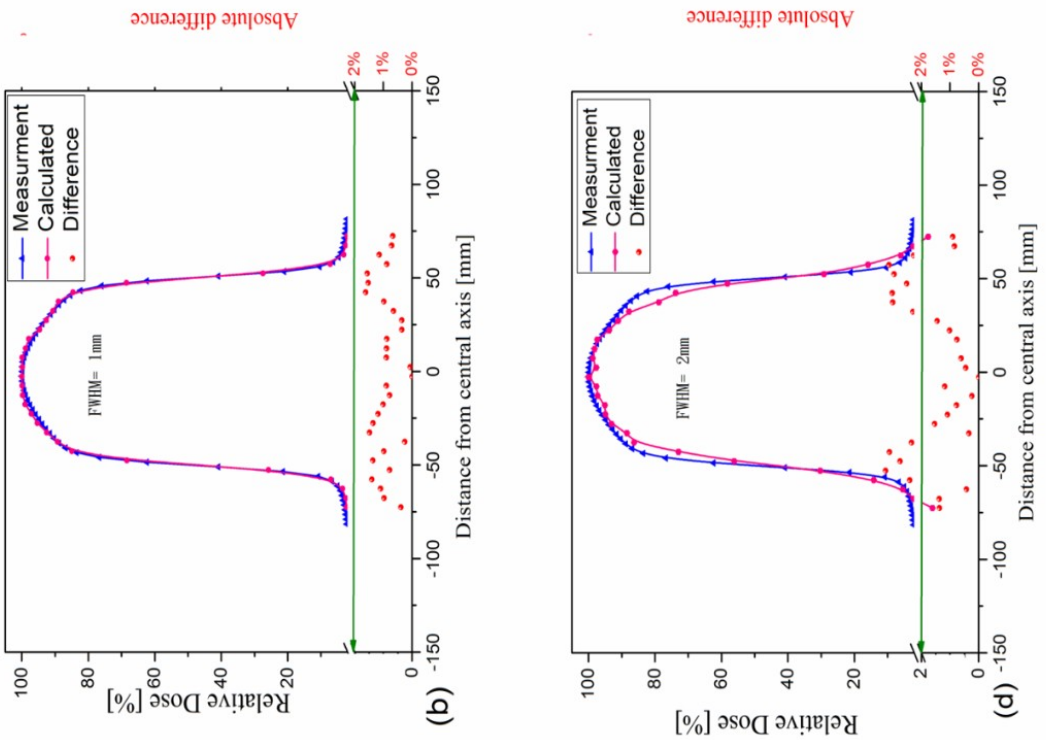

Figure 4.2. Dose profile results for FFF, with mean energy of 8.8 MeV, spread energy 0.4 MeV and full width of half maximum (FWHM) of (a) 0.5 mm, (b) 1 mm, (a) 1.5 mm, (b) 2 mm

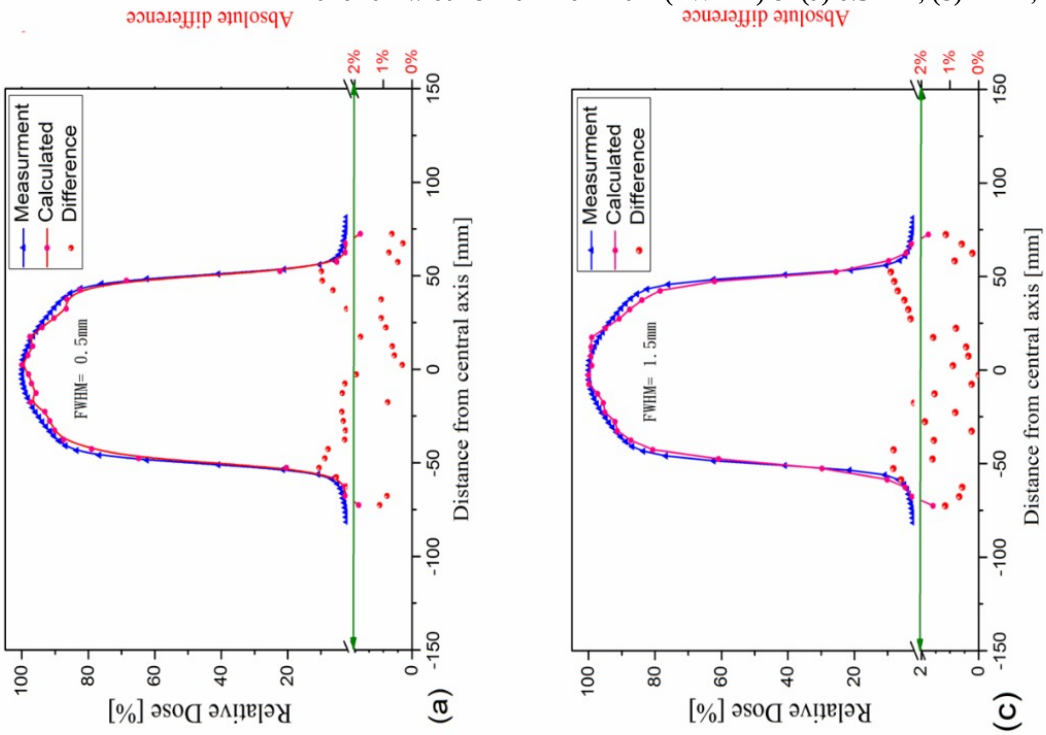

4.2 Percent Depth Dose

In order to calculate the PDD, a box-mesh with dimensions of 5×5×300 mm^3 on the central axis was defined and divided into 60 cells in the z-axis direction (the beam central axis) with dimension of 5×5×5 mm^3. Then the total deposited dose (all particles) in each cell was calculated via the command-based-scoring method. Table 4.1 shows the input micro file for running this simulation.

Table 4.1. The input micro file to calculate PDD

Input
/score/create/boxMesh boxMesh_1 /score/mesh/boxSize 0.250.25 15 cm /score/mesh/translate/xyz 0 0 115 cm /score/mesh/nBin 1 1 60 /score/quantity/doseDeposit depth-dose /score/close /run/beamOn 1.5×10^9
Output
score /dumpQuantityToFile boxMesh_1 depth-dose PDD.txt

Figure 4.3 displays the ecomparison of Monte Carlo-calculated PDDs of the FFF beam for 10×10 and 20×20 cm^2 field sizes with the measured commissioning data in the water phantom. As shown in Figure 4.3 the difference between measurements and model at points below the build-up region is less than 2% (all absolute difference points lie under green line), and in the build-up region, the difference is less 0.6% for both. This difference is in the range of measurement error and calculation error. Therefore, the difference is acceptable.

Due to the relative contribution of scattered radiation, the PDD curve and depth of maximum dose depend somewhat on the field size. This effect could be observed both in the measured data and in the calculations. For 10×10 cm^2, the measured (calculated) d_{max} is 1.8 cm (1.8 cm) and for 20×20 cm^2, the measured (calculated) d_{max} is 1.9 cm (1.9 cm). There was hence a good match between calculations and measurements.

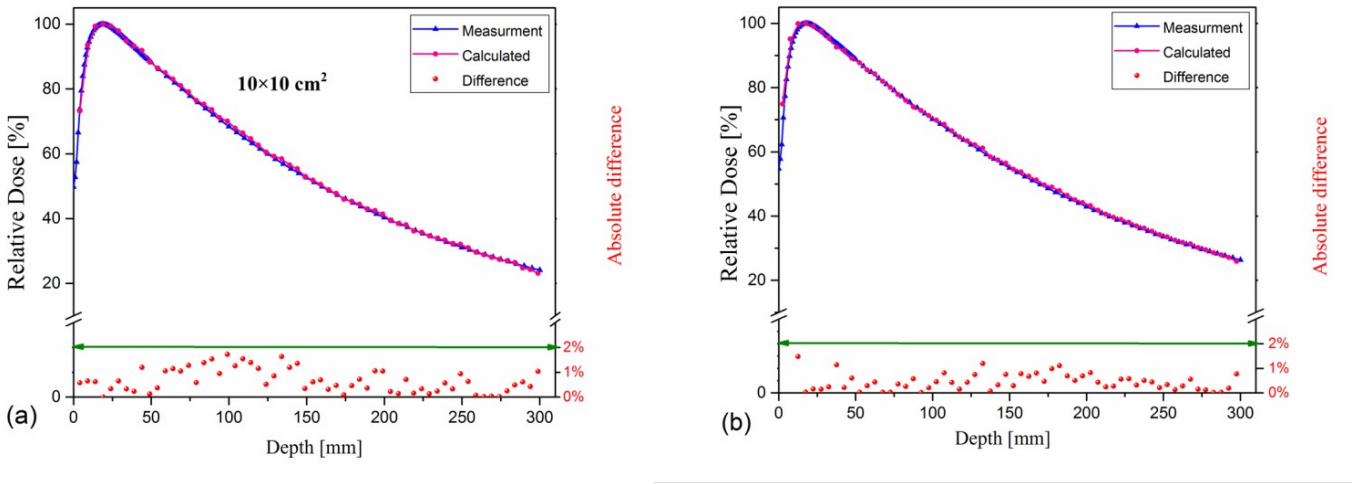

Figure 4. 3. Comparison of Monte Carlo-calculated PDDs of the FFF beam for a) 10×10 and b) 20×20 cm^2 field sizes with commissioning data in water phantom.

Table 4.2 focuses on analyzing the PDD curves of Figure 4.3. The column giving the difference between measured and calculated data reports less than 0.83% relative differences for both square field sizes of 10 and 20 cm, which again confirms the validation of the simulation and good match at all depths. Both data sets exhibit the same general behavior: For example, the calculated PDD at 50 mm decreased by a factor of 21.7% at 100 mm depth for 10×10 cm^2; for square field size of 20 cm this factor is 20.2%, which shows the PDD in 10×10 cm^2 field decreases with a steeper slope.

For characterizing the photon spectrum for practical dosimetry purposes, there are two specific quantities: d_{max} and the ratio D_{20}/D_{10}. As aforementioned, the depth of calculated dose d_{max} is similar to measured d_{max}. According to the last row of Table 4.2, it becomes clear that D_{20}/D_{10} obtained with Geant4 also follows the ratio measured by ionization chamber in the water phantom with a difference of 0.33% for the 10×10 cm^2 field and 0.32% for the 20×20 cm^2 field. Therefore, it can be said that the photons created have the correct energy.

The D_{20}/D_{10} also shows the fall-off behavior of the PDD curves and it changes with changing the field size. For the calculated PDD, when the field size increases from 10×10 cm^2 to 20×20 cm^2, the D_{20}/D_{10} increased by 4.4% and for the measured data the D_{20}/D_{10} increased by 3.7% by increasing the field size.

Table 4.2. Comparison of absorbed dose from measurement and calculation at different depths on central axis

Depth (cm)	PDD					
	10×10 cm^2			**20×20 cm^2**		
	Measurement	**Calculation**	**Difference**	**Measurement**	**Calculation**	**Difference**
1.9	100	99.56	0.44%	99.33	99.70	0.37%
5	88.19	87.78	0.46%	88.77	88.42	0.39%
10	68.37	68.71	0.49%	70.14	70.55	0.58%
20	40.32	40.31	0.02%	42.95	43.31	0.83%
D_{20}/D_{10}	0.589	0.587	0.33%	0.612	0.614	0.32%

4.2.1 Depth Dose distribution YZ-Direction:

To give a 3D representation of the depth dose distribution of the FFF beam with open field size 10×10 cm^2, Figure 4.4 illustrates the calculated output of the linac head in the homogeneous water phantom placed at Z=100 cm from the target. These data were calculated by the command-based-scoring method with cell (voxel) size of 5×5×5 mm^3 (X-Y-Z). It shows the contour of deposited dose in the water phantom point by point, which is normalized to maximum dose at a depth of 1.9 cm.

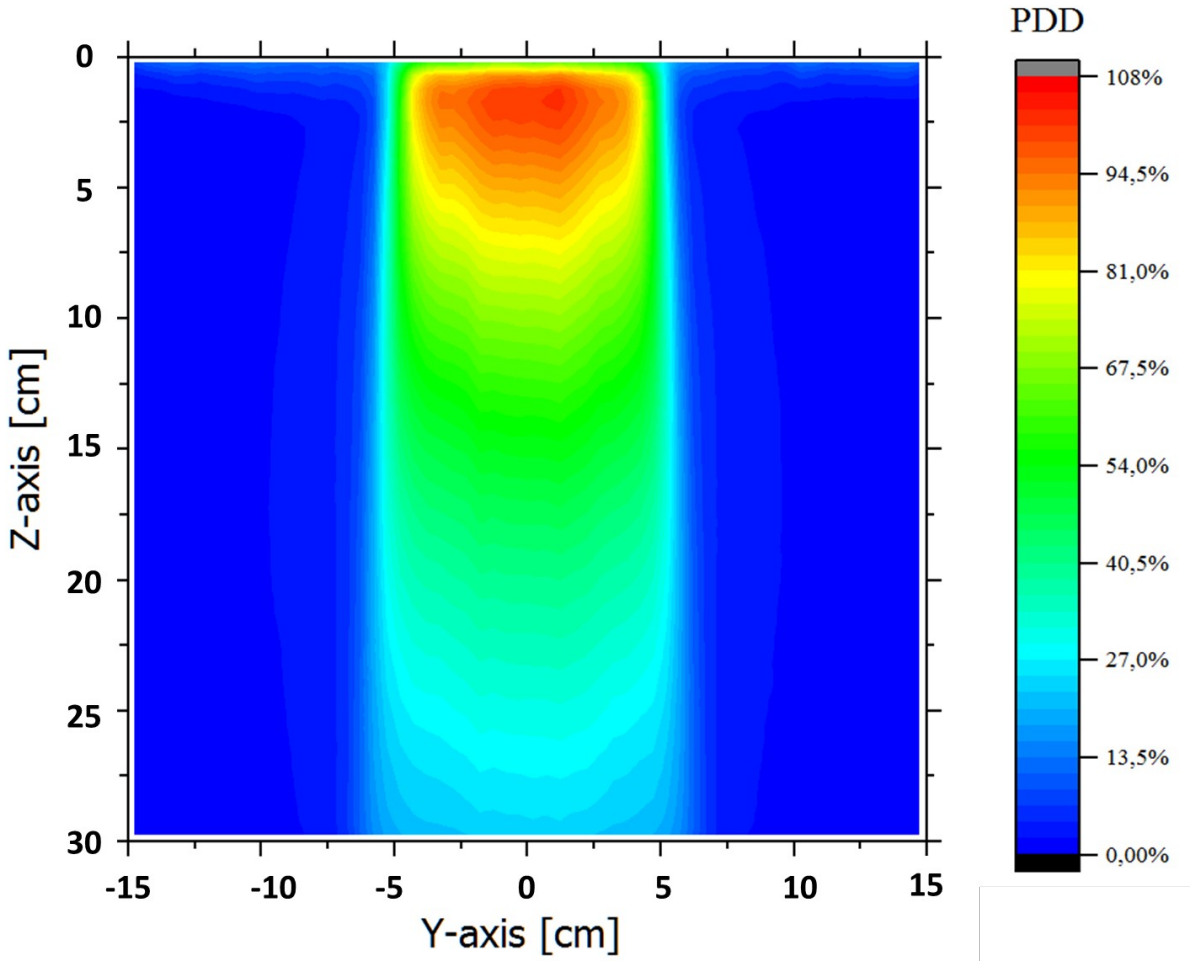

Figure 4.4. Contour plot of the normalized depth dose distribution calculated on the central axis for the FFF beam at 10×10 cm^2 field size.

4.3 Beam profile

To calculate the beam profiles, a box-mesh with a dimension of 300×5×5 mm^3 (x-y-z) perpendicular to the central axis was defined and divided into 60 cells in the x-axis direction with dimension 5×5×5 mm^3 and then the total deposited dose (all particles) in each cell was calculated via the command-based-scoring method.

Table 4.3 shows the input micro file for calculating the beam profile at a depth of 1.9 cm in the water phantom. This depth was selected because all experimental data as reference were acquired at 1.9 cm depth, which was the experimentally observed maximum depth.

Table 4.3. Input micro file to calculate the beam profile

Input
/score/create/boxMesh boxMesh_1
/score/mesh/boxSize 150 2.5 2.5 mm
/score/mesh/translate/xyz 0 0 101.9 cm
/score/mesh/nBin 60 1 1
/score/quantity/doseDeposit beam-profile
/score/close
/run/beamOn 2×10^9
Output
score/dumpQuantityToFile boxMesh_1 beam-profile BeamProfile.txt

The comparison between measurements and calculations of the FFF dose profile at a depth of 1.9 cm for two field sizes (10×10 and 20×20 cm^2) in the water phantom is displayed in Figure 4.5. The SSD was 100 cm and all profiles were normalized to their maximum value (100%) on the central axis.

Generally, there was a good agreement between measurements and calculations for all points, as all deviations below 2% absolute difference. To go into more detail, the deviation within the region from 100% dose to 50% dose is less than 1.6% for a square field size of 20 cm and less than 1.1% for square field size of 10 cm, and for the penumbra tail, this deviation increased up to 1.9% and 1.6 % for 20×20 cm^2 and 10×10 cm^2 field sizes, respectively.

Figure 4.5. Comparison between measurements and calculations of the FFF dose profile at a depth of 1.9 cm for two field sizes of 10×10 and 20×20 cm^2 in the water phantom.

In all comparisons between measurements and calculations of the beam profile curves (Figure 4.5 and all following curves), a large difference in the out-of-field region was outstanding, in which calculation values are smaller than the reference measurements. A possible reason for the difference between measurements and calculations could be due to the difference in voxel size in the calculation (5 mm) and the measurements (2.55 mm step in lateral tail). Figure 4.6 illustrates the dependency of deposited dose per incident particle on voxel sizes.

As you see in Figure 4.6 when the voxel size increases from 0.5×0.5×0.5 mm^3 to 1×1×1 mm^3 the value of the dose increase about 43%. Also it increases by more than a factor of 17 for 20×20×20 mm^3 comparing to the value of 1×1×1 mm^3 voxel size. Additionally, the out-of-field dose is delivered by low intensity scattered radiation. Therefore, the high statistical uncertainties might be another possible reason.

Figure 4.6. Dependency of deposited dose per incident particle on voxel sizes

When the measurement data were acquired, for checking more dose characteristics in the water phantom, dose profiles at different depth of water phantom were measured in addition to the depth of 1.9 cm. Therefore, for further checking of our simulation and its precision, the Monte Carlo calculated dose profiles at depths of 5, 10, and 20 cm were compared with PTW ionization chamber measurement data in Figure 4.7.

Overall, for all depths the errors lie below 2% absolute difference. These errors were smaller within the inner 80% of the field sizes and higher in the penumbra and out-of-field region because of higher statistical uncertainty and different voxel size in measurement and calculation, as mentionedbefore. Consequently, the results of figure 4.7 demonstrated the validation of our simulation in various depths of the water phantom, too.

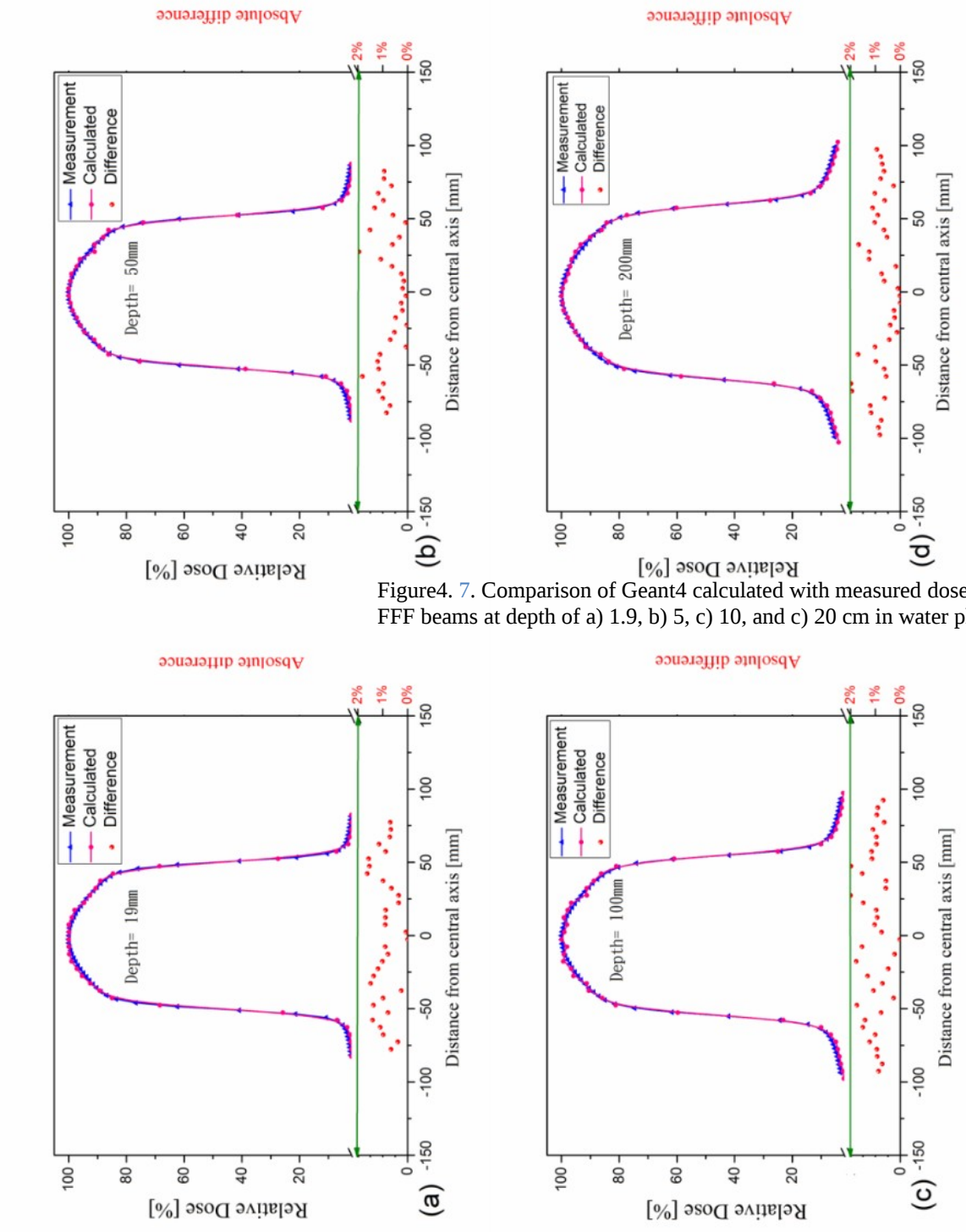

Figure4. 7. Comparison of Geant4 calculated with measured dose profiles for 10×10 cm^2 of FFF beams at depth of a) 1.9, b) 5, c) 10, and c) 20 cm in water phantom

In Figure 4.7 all dose profiles were normalized to their respective maximum value on the central axis, so this normalization did not reflect the decreasing relative dose by increasing depth. So in order to illustrate the depth dependency of the dose profiles, the measured and calculated beam profiles at different depths were normalized to the maximum value of dose on the central axis of the beam profile at maximum depth (1.9 cm) in Figure 4.8. Figure 4.8 confirms that even the percentage of variations in dose decay versus depth in the calculated beam profiles is exactly the same as measured and shows another aspect of the simulation's accuracy.

Figure 4.8. Comparison of calculated with measured dose profiles at various depths for FFF beams of $10\times10cm^2$ field sizes

For comparing the FFF profiles with each other in same condition the normalization to maximum dose on central axis is acceptable but for reporting the beam profile parameter like unflatness, symmetry and other parameters mentioned before, all profiles should be normalized relative to the flat profiles.

After normalization the FFF profile according to Fogliata et al., 2012 [21], procedure, the dosimetric field size for the 10×10 cm^2 and 20×20 cm^2 were 10.8 cm and 21.5 cm, respectively. Unflatness, slope, peak position and symmetry of the FFF beam profile are reported in Table 4.4a-c. Unflatness decreases with increasing depth (about 1.5% for 10×10 cm^2 and 2.7% for 20×20 cm^2 for a depth increase from 1.9 to 20 cm).

Table 4.4-a. Calculated unflatness for 10 and 20 cm square fields.

Depth (cm)	**Unflatness**	
	10×10cm²	**20×20cm²**
1.9 (d_{max})	1.150	1.379
5	1.141	1.370
10	1.137	1.347
20	1.133	1.341

The slope parameter was recorded for both field sizes and is reported as average value between left and right slopes in Table 4.4-b. Similar to the unflatness, the slope decreases with increasing depth (from 1.9 to 20 mm depth, the decrease amounts to 72 % for the 10 cm and by 58 % for the 20 cm square field).

Table 4.4c reports symmetry and peak position for the FFF beams. It should be mentioned that the possible differences may be because of statistical uncertainties of simulation and the definition of the normalization factor.

Table 4.4-b Calculated slope for 10 and 20 cm square fields.

Depth (cm)	**Slope**	
	10×10cm^2	**20×20cm^2**
1.9 (d_{max})	0.391	0.408
5	0.337	0.358
10	0.286	0.273
20	0.108	0.171

Table 3.4-c. Peak position and symmetry of simulated beam profiles for 10 and 20 cm square fields at depth of 10 cm.

Parameter	**Field size**	
	10×10cm^2	**20×20cm^2**
Peak position	-0.34 mm	0.25 mm
Symmetry	2.7%	1.4%

4.4 Photon Energy Spectra

Phase-space files (PSFs) recorded the all information of secondary particles produced in the linac head treatment. These files were used as sources to obtain the photon energy spectrum. The *TrackingAction* class extracts all information like fluence, kinetic energy, type and position of particles in Geant4. Since the information of all secondary particles were rerecorded in PSFs and we need just the data of photon beams, it is possible to put a condition in the *TrackingAction* class for ignoring other particles and just analyzing the photon beam associated with PSFs. An example is shown in Figure 4.9-a.

Figure 3.10-a illustrates the evaluation of photon fluence per incident electron (5×10^8) for two square field sizes of 10 and 20 cm at the surface of the water phantom with 100 cm SSD. Due to the reduced attenuation by the jaws in the larger field, more photons can penetrate and yield more intensity compared with the smaller field size.

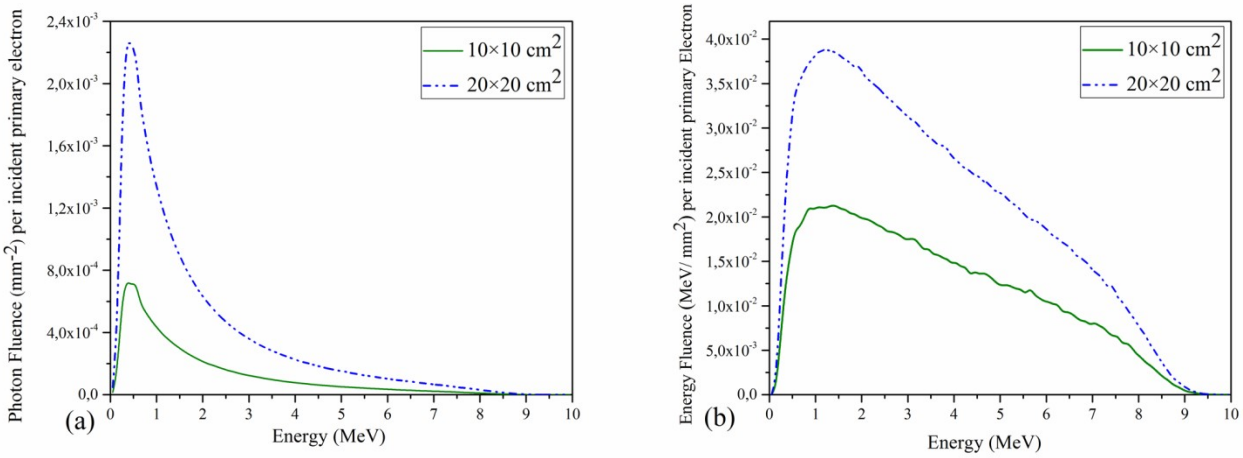

Figure 4.9. a) Photon fluence spectra, b) Energy fluence for 10×10 and 20×20 cm^2 field sizes

Additionally, if we want to find the photon energy spectrum at a given position, we should find the fluence of photons with different energies. To do this, the energy of photons from zero to maximum was subdivided to given intervals (depending on the need for this partition to be linear or logarithmic) and the fluence of photons with different energies in each of these intervals was calculated. In the scientific literature, it is customary to divide the fluence into

bins of 0.1 MeV (Figure 3.10-b). According to photon energy spectrum, the mean energy of photons for field sizes of 10×10 cm^2 was about 1.9 MeV, which was 1.87 for the 20×20 cm^2 field size and there is just 2.1% difference in the mean energy by changing the field size.

4.4.1 The effect of the components of the linac head on photon and electron spectrum

To discuss the effect of the components of the linac head on the photon spectrum, Figure 4.10 shows the photon and electron fluences per incident primary electron after the target, pre-collimator, and jaws for the FFF beam. According to this figure, evidently the intensity of produced photons decreases when moving away from the target, while the mean energy increases. The mean energy of produced photons under the target, pre-collimator, and jaws for 10×10 (20×20) cm^2 field size is 1.54 MeV and 1.61 MeV, 1.9 (1.86) MeV, respectively. On the other hand, after passing through the linac components the mean energy of the electrons decreased from 2.8 MeV under the target to 2.6 MeV, 1.8 (2.2) MeV under the pre-collimator and jaws for 10×10 (20×20) cm^2 field, respectively.

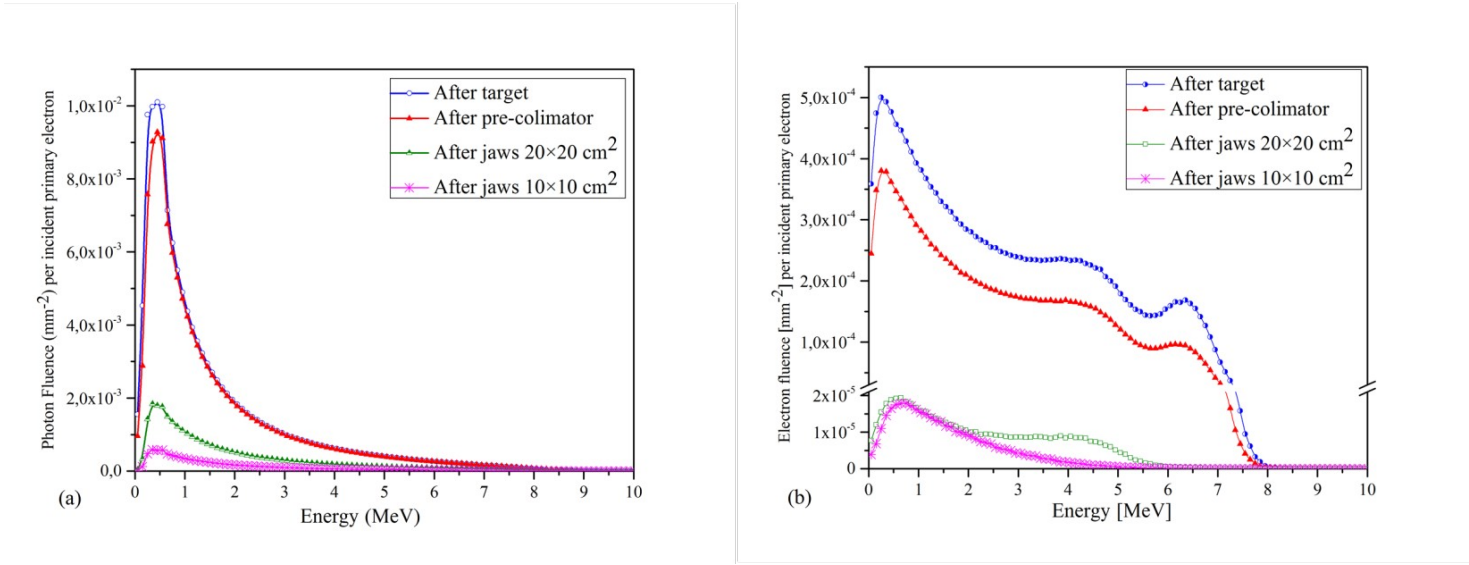

Figure 4.10. Effect of the linac head components on the photon and electron spectrum: a) photon and b) electron fluence per incident primary electron at different stages of the beam line

It should be mentioned that the fluence of electrons as compared with photon fluence on the surface of the water phantom is much lower and in fact, photons play the main roll in depositing dose in the water phantom. This is confirmed by Figure 4.11 which shows that the fluence of photons is on averagely188 times greater than the electron fluence for the 10×10 cm^2 field size and on averagely 302 times greater for a 20×20 cm^2 field for FFF beam (at the surface of the water phantom with a SSD of 100 cm).

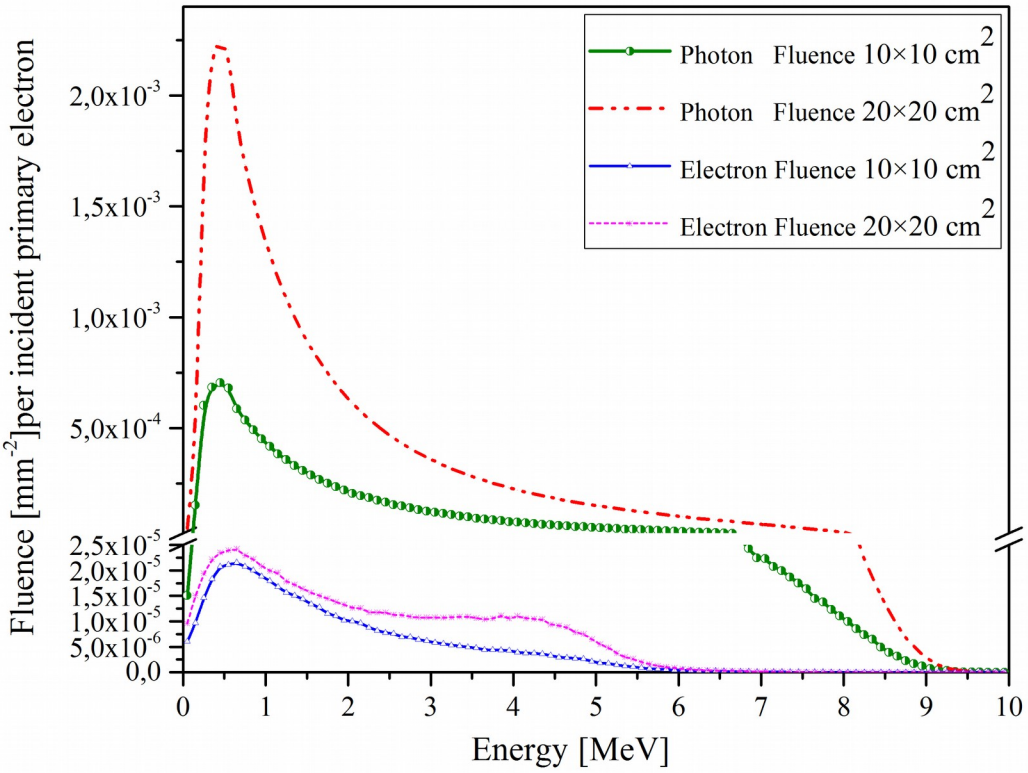

Figure 4.11. Comparison of photon fluence with electron fluence per incident primary electron on target on the surface of the phantom for two field sizes

4.5 Surface and buildup region dose

Surface dose and the exact deposited dose in the buildup region cannot be precisely measured using the ionization chamber because of the chamber volume (volume averaging effect); hence the calculation method is one of the best ways to consider the buildup region besides others possibilities like correction factors [74].

Contaminant electrons from scattering and secondary electrons generated in the first layers of the patient are two reasons that increase the surface dose in the buildup region. As a result of removing the flattening filter, the effect of the first factor decreases, therefore the second factor plays a larger role by generating secondary electrons in the first layers of the phantom (skin), and it depends strongly on the size of field.

For more consideration, Figure 4.12 and Table 4.5 report the effect of field size on surface dose and on deposited energy in the buildup region on the central axis. Surface dose was defined as deposited energy inthe first millimeter (the air-skin boundary) of the water phantom and the buildup region is defined from the surface of the phantom to the depth of maximum dose on the central axis. It is noteworthy to mention that the calculated surface dose was obtained from a different program, in which voxels were defined with dimension of $1\times1\times1$ mm^3 to obtain the exact PDD in the buildup region. Therefore, the PDD was obtained in 1 mm steps instead of 5 mm steps.

Table 4.5. Effect of field size on surface dose and on deposited energy in the buildup region on the central axis for FFF beam. Also, calculated and measured values and their absolute differences are reported.

	Relative Surface Dose (%)					
Buildup Thickness (mm)	**10×10 cm^2**			**20×20 cm^2**		
	calculated	**measurement**	**Absolut difference**	**calculated**	**measurement**	**Absolut difference**
1	42.34	49.79	15%	47.99	54.72	12%
5	86.79	79.46	8.4%	82.57	85.57	3.5%
10	96.91	94.58	2.4 %	95.91	95.92	0.01%

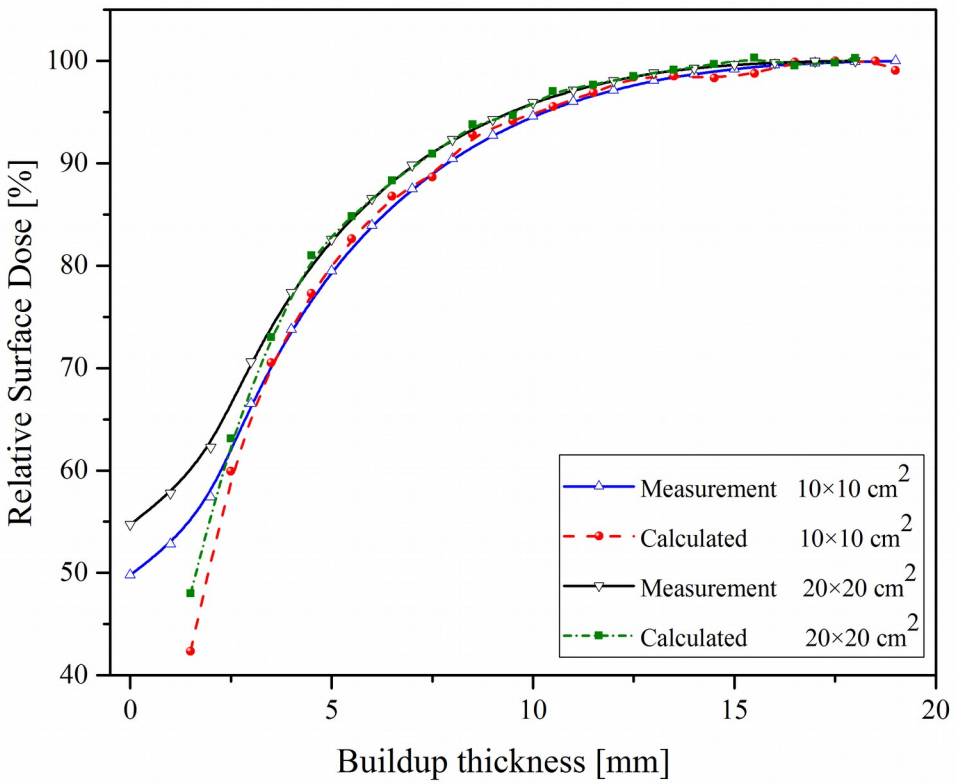

Figure 4.12. Effect of field size on surface dose and on deposited energy in the buildup region on the central axis for FFF beam. (Comparison between calculation and measurement)

4.6 Off-axis change

In this section, the dependency of photon beam characteristics on off-axis distance (OAD) for the FFF beam is investigated. In this work, n cm OAD will be taken to mean n cm shift along both the X and the Y directions, i.e. √2×n cm geometrical distance from the CAX.

4.6.1 PDD

For calculating the PDD at various OADs, similar to previous simulations a box mesh with a dimension of 5×5×300 mm^3 was defined and placed at three different OADs of 2.5 cm, 5 cm, and 7.5 cm in three separate programs. Similar to the simulation of the PDD on the central axis, the mesh-box was divided into 60 cells in the z-axis direction and the same PSF was used as photon source at 20 cm distance from the target. The number of histories was similarly set to 1×10^9.

As a first step, the validation of the simulation should be again tested. Figure 4.13a-c shows the comparison of the simulation for the PDD of FFF beams at an OAD of 2.5 cm, 5 cm, and 7.5 cm for 20×20 cm^2 field size.

Figure 4.13-c illustrates the comparison of the PDD on the central axis (CAX) with PDDs atdifferent OADs. All PDD curves were normalized to 100% at the depth of their maximum dose (d_{max}). It is clear that all curves have same d_{max} (1.8 cm) except at an OAD of 7.5 cm for which the d_{max} was shifted to 1.9 cm. Overall, all curves were similar and there are no significant differences in the buildup region, while deposited energy in the tail of the curves increased with increasing the OAD, so that deposited energy in the region after buildup for OAX of 7.5 cm reached the highest value.

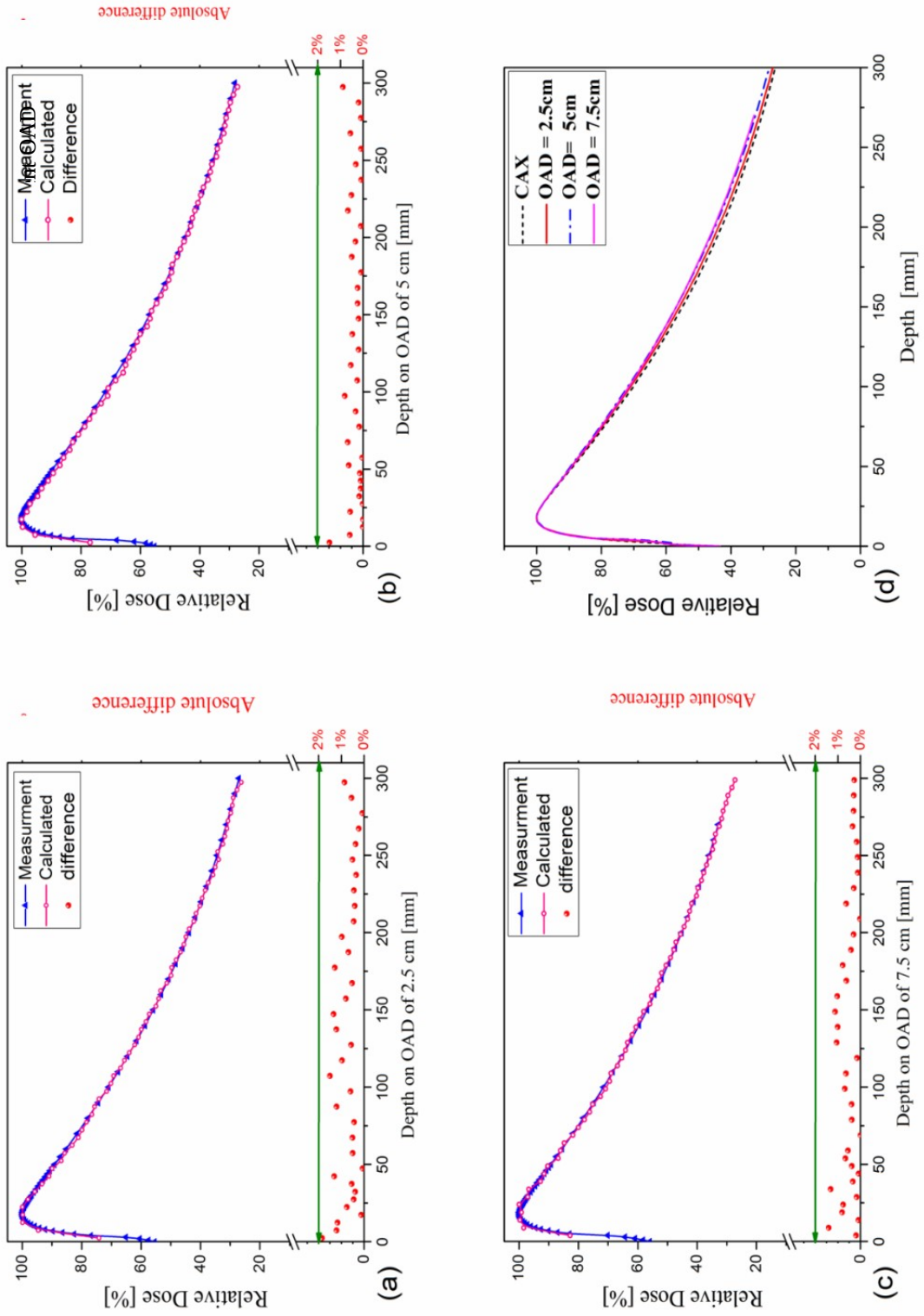
(a)
Measurment
Calculated
difference
Relative Dose [%]
Depth on OAD of 2.5 cm [mm]
Absolute difference
2%
1%
0%
(b)
Measurment
Calculated
Difference
Relative Dose [%]
Depth on OAD of 5 cm [mm]
Absolute difference
(c)
Measurment
Calculated
difference
Relative Dose [%]
Depth on OAD of 7.5 cm [mm]
Absolute difference
(d)
CAX
OAD = 2.5cm
OAD= 5cm
OAD = 7.5cm
Relative Dose [%]
Depth [mm]

For a more precise comparison, Table 4.6 summarizes the D_{10}, D_{20}, and ratio of D_{20}/D_{10} to show the dependency of the fall-off behavior of the PDD curves on OAD. According to Table 3.6, the ratio of calculated D_{20}/D_{10} on the central axis was 0.614 and attained 0.6257, 0.6324, and 0.6420 at an OAD of 2.5, 5, and 7.5 cm, respectively, whichdeviated from the measurements by 0.29%, 1.13%, 1.09%, and 1.51%, respectively.

Table 4.6. Comparison of calculated D_{20}/D_{10} at various OAD with measurement (20×20 cm^2field size)

OAD (cm)	CAX		2.5		5		7.5	
	Meas.	**Cal.**	**Meas.**	**Cal.**	**Meas.**	**Cal.**	**Meas.**	**Cal.**
D_{10}	70.14	70.55	70.97	71.36	71.82	71.13	71.54	70.60
D_{20}	42.94	43.31	43.90	44.65	44.93	44.98	45.24	45.33
D_{20}/D_{10}	0.6122	0.614	0.6186	0.6257	0.6255	0.6324	0.6323	0.6420
Difference (D_{20}/D_{10})	0.29%		1.13%		1.09%		1.51%	

4.6.2 Photon Spectra

Figure 4.14 evaluates photon fluence per incident electron (5×10^8 histories) for a square field size of 20 cm on the CAX and at different OAD (SSD=100 cm). This figure is obtained from a program in which a scoring plane with square shape was simulated around the CAX and off-axis with dimension of 5×5 mm^2. The range of energies from zero to 10 MeV was divided into 50 intervals (bin=50) of 0.5 MeV and then the number of photons passing the scoring plane were recorded and reported in Figure 4.14.

The mean energy was 1.87, 1.85, 1.856, 1.87 MeV at an OAD of 0, 2.5, 5, 7.5 cm, respectively. Therefore, there is less than 1% reduction in mean energy when the OAD increase from zero up to 7.5 cm. This shows that for FFF beams, the OAD has no strong

effect on the mean energy of the photons, as no marked hardening effect occurs at various distances off-axis.

Nevertheless, the photon fluence was decreased by increasing the OAD. For example, at an OAD of 7.5 cm the fluence was decreased by a factor of 1.7 on average when compared with the fluence on the CAX because the angular distribution of bremsstrahlung photons depends strongly on primary electron energy and most photons in the MV range are produced around the direction of primary electrons, $\varphi=0$, and there is a sharp fall-off in photon fluence for high angles (Figure 2.4).

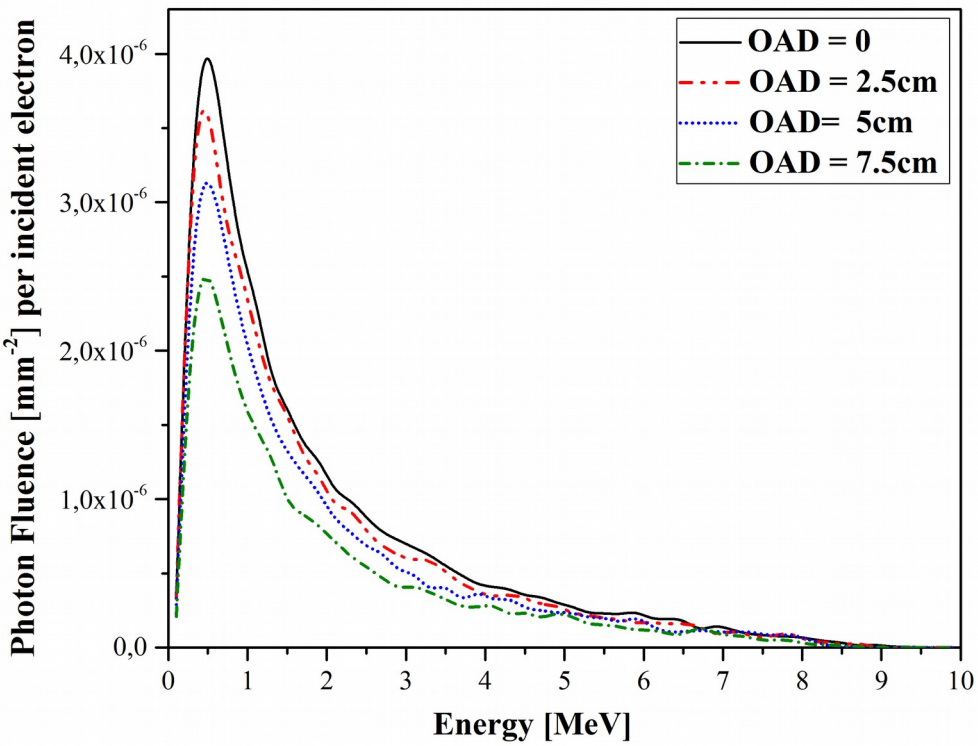

Figure 4.14. Photon fluence of FFF beam on CAX and at different OAX for 20×20 cm^2 field size

4.7 Dosimetric properties of FFF beam versus flat 6 MV

As mentioned before, simulation of the flattening filter was one of the challenges in this work and a significant number of programs were implemented to find the geometry of the flattening filter (Figure 4.15).

The flattening filter consists of five cone-shaped layers with various heights and radii. The first four layers are placed in the conical hollow of the primary collimator and the fifth layer is placed outside the primary collimator. The radius of the fifth layer is equal to the outer radius of the primary collimator (2.6 cm). The height of the flattening filter is 1.85 cm and the density of stainless steel is 8.03 g/cm^3.

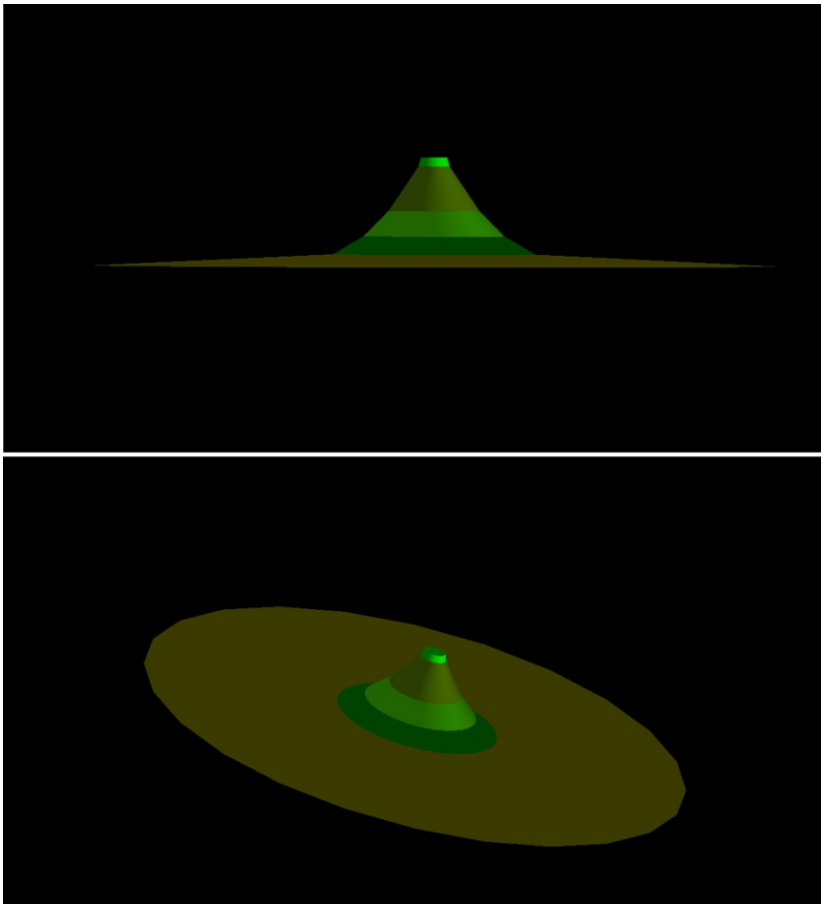

Figure 4.15. View of simulated flattening filter

4.7.1 Primary Electron Beam Parameters

After simulating the geometry of the flattening filter and adding to geometry of Linac head, the program was executed with primary electron parameters used in the FFF case; energy=8.8 MeV, spread energy=0.4 MeV, and FWHM=1 mm. The method for obtaining PDD curves of flat 6 MV beams was the same with FFF, just in this case for getting good statistical accuracy; the calculation was longer because of more histories were required.

The output for the primary electron parameters used in the FFF beam did not match the measurement and the PDD curve had higher values (Figure 4.16). Therefore, lower energies with various spread energies (more than 20 executed programs) were examined and finally a mean energy of 7.5 MeV and spread energy of 0.4 MeV with lowest absolute difference were selected as optimum primary electron energy for the flat 6 MV beam. Afterwards, the beam profiles showed that the spot size (FWHM) of the electron source is similar to the FFF mode.

Figure 4.16. comparison of calculated PDD curve of Flat 6 MV with primary electron parameters used in the FFF case (energy=7.6 MeV, spread energy= 0.4 MeV, and FWHM=1 mm), with measurements.

The results of the optimum electron parameters for both depth-dose and beam profiles are illustrated in Figure 4.17 which shows the Monte Carlo validation in the case of flat 6 MV for 10×10 and 20×20 cm^2 field sizes. Depth dose curves were normalized to maximum dose and beam profiles at depth of maximum dose (16 mm) were normalized to their maximum value on the central axis. The absolute difference between measurements and calculations was less than 2% for depth doses and beam profiles. The mean electron energy of flat 6 MV was 7.5 MeV and the spread energy and spot size of the selected Gaussian distribution source were 0.4 MeV and 1 mm, respectively.

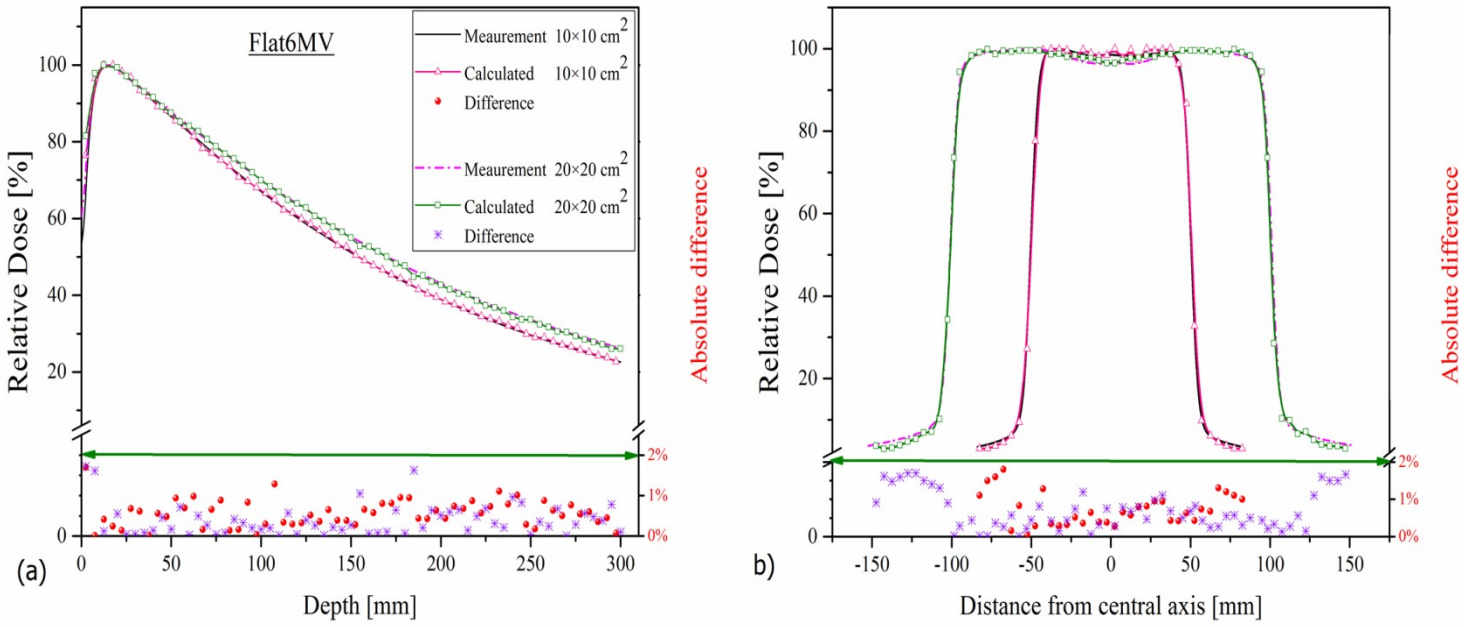

Figure 4.17. Monte Carlo validation; a) depth dose curve and b) beam profile of the Flat6 MV beam, for 10×10 and 20×20 cm^2 field sizes.

4.7.2 Depth Dose

The calculated depth dose on the central axis of both configurations of FFF and flat 6 MV for both filed sizes is plotted in Figure 4.18. The penetration of both beam modalities is evaluated in Table 4.7 by the D_{20}/D_{10} ratio. Overall this ratio increases by increasing the field size from 10 to 20 cm (about 7% for flat 6 MV and 5% for the FFF beam). The dose rate of the FFF beam was 2.8 (2.96) times higher than for the flattened beam for a field size of 10×10 (20×20) cm^2.

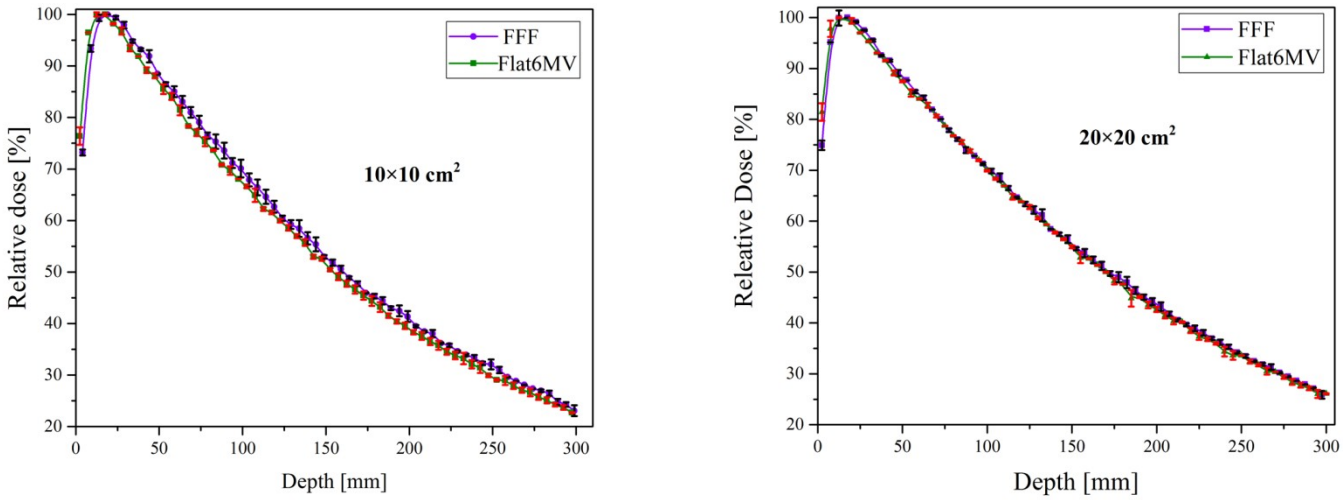

Figure4.18. Calculated depth-dose of FFF and flat6 MV beams for two field size of 10×10 and 20×20 cm^2

Table 4.7. Calculated D_{20}/D_{10} in FFF and flat 6 MV mode for two different field sizes

Field size (cm^2)	**D_{20}/D_{10}**	
	FFF	**Flat 6 MV**
10×10	0.587	0.578
20×20	0.614	0.614

4.7.3 Dose Rate:

One of the advantages of removing the flattening filter is the increase the dose rate which leads to a decrease the treatment time and consequently enhancements the efficiency of treatment. According to some reports the dose rate will be increase more than factor of 2 by the removing flattening filter [44, 66]. Hence check this issue, Figures 4.19 displays the calculated dose rate for both FFF and flat 6 MV beams with different open field sizes.The dose rate is defined as amount of the dose per incident electron (Gy/primary electron) on the central axis at depth of 10 cm with SSD=100 cm. It is clear that for two field sizes, the dose rate of FFF beams is higher than for the flattened beam at each point of the central axis. The dose rate of the FFF beam is 2.8 (2.96) times higher than the flattened beam when the open field is 10×10 (20×20) cm^2.

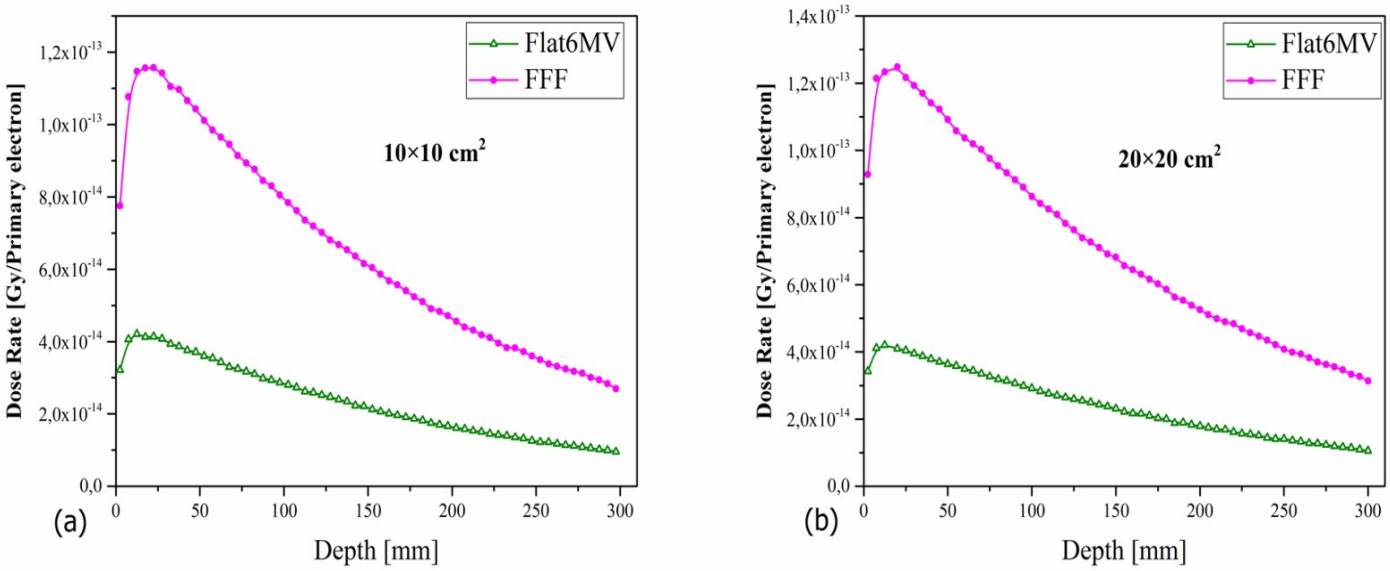

Figure 4.19. Depth dose per incident particle on central axis (dose rate) of FFF and flat 6 MV beams for 10×10 and 20×20 cm^2

4.7.4 Surface dose and buildup region

Table 4.8 evaluates the delivered dose in the buildup region for both configurations. It reports the calculated relative buildup dose normalized to D_{max} on the central axis and at SSD=100 cm for each corresponding open field. It is clear that the FFF beam creates less surface dose because of less scattering compared to the flattened beam. According to Table 4.8 the surface dose of the FFF beam was about 21% less than for the flat 6 MV for open field 10×10 cm^2 and 20% less for 20×20 cm^2.

Table 4.8. Comparison of the calculated relative buildup dose of the FFF with the flat 6 MV modes.

Buildup thickness (mm)	**Field size (cm^2)**			
	10×10		**20×20**	
	FFF	**Flat 6 MV**	**FFF**	**Flat 6 MV**
1 (Surface)	42.34	53.58	47.99	60.19
5	86.79	83.28	82.57	89.39
10	96.91	98.69	95.91	99.88

4.7.5 Beam profile

Figure 4.20 shows the comparison of the normalized beam profiles for the FFF and flat beams for two open field sizes at depth of 10 cm. Table 4.9 evaluates the 20-80% penumbra for the flattened and unflattened beams. The FFF beams have a smaller penumbra because these beams have softer spectrum and also less scattering. The penumbra of the 10 cm square open field size of flattened beam was 0.4 mm larger than for the corresponding FFF beam and this difference was 0.2 mm for 20 cm square open field size.

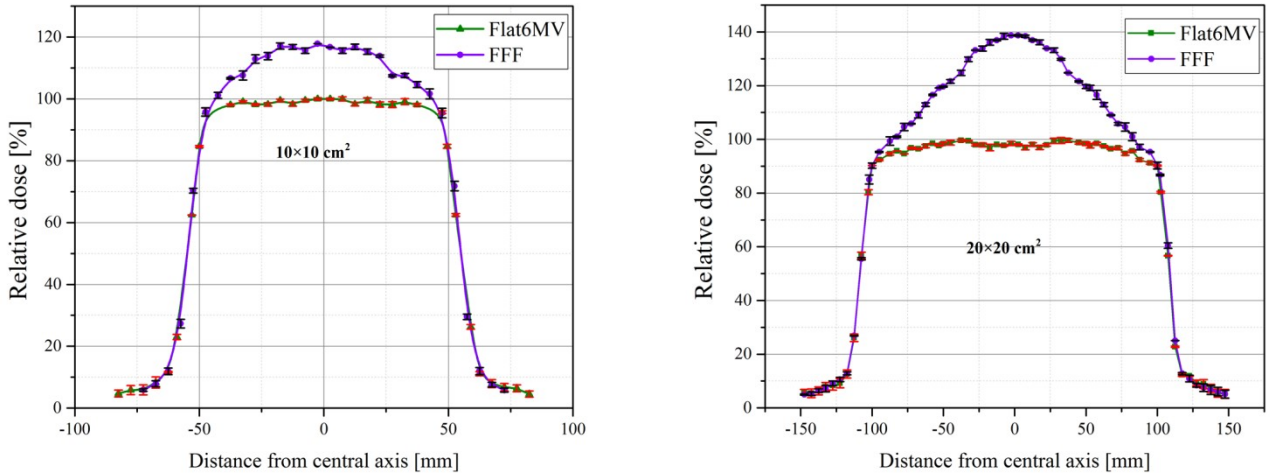

Figure 4.20. Comparison of calculated beam profiles of FFF and flat 6 MV for two field sizes at depth of 10 cm.

Table 4.9. Calculated penumbra for 10 and 20 cm field side at a depth of 10 cm.

Field size (cm^2)	Penumbra (mm)	
	FFF	Flat 6 MV
10×10	9.35	9.75
20×20	11.57	11.77

4.7.6 Photon and electron beam spectra

Figure 4.21.a-b illustrates the photon energy distributions normalized to their maximum value (100%). Although the primary electrons in flat 6 MV configuration have lower energy (7.5 MeV) compared to FFF (8.8 MeV), the FFF mode has a larger photon distribution at low energies (<=1.55 MeV), which shows that the flattening filter acts as an energy filter for photons and the mean energy was higher for the flat 6 MV beams. The mean energy of photons of the 10×10 cm^2 field size was 1.91/2.14 MeV for FFF / flat 6 MV beams and was 1.87 / 2.06 MeV for 20×20 cm^2. Figure 4.21.c-d illustrate the corresponding electron energy fluence at the surface of the water phantom for both beam facilities. The electron mean energy of the FFF beam for the 10×10 (20×20) cm^2 field was 3.12 (3.53) MeV and for the flat 6 MV 2.63 (2.61) MeV.

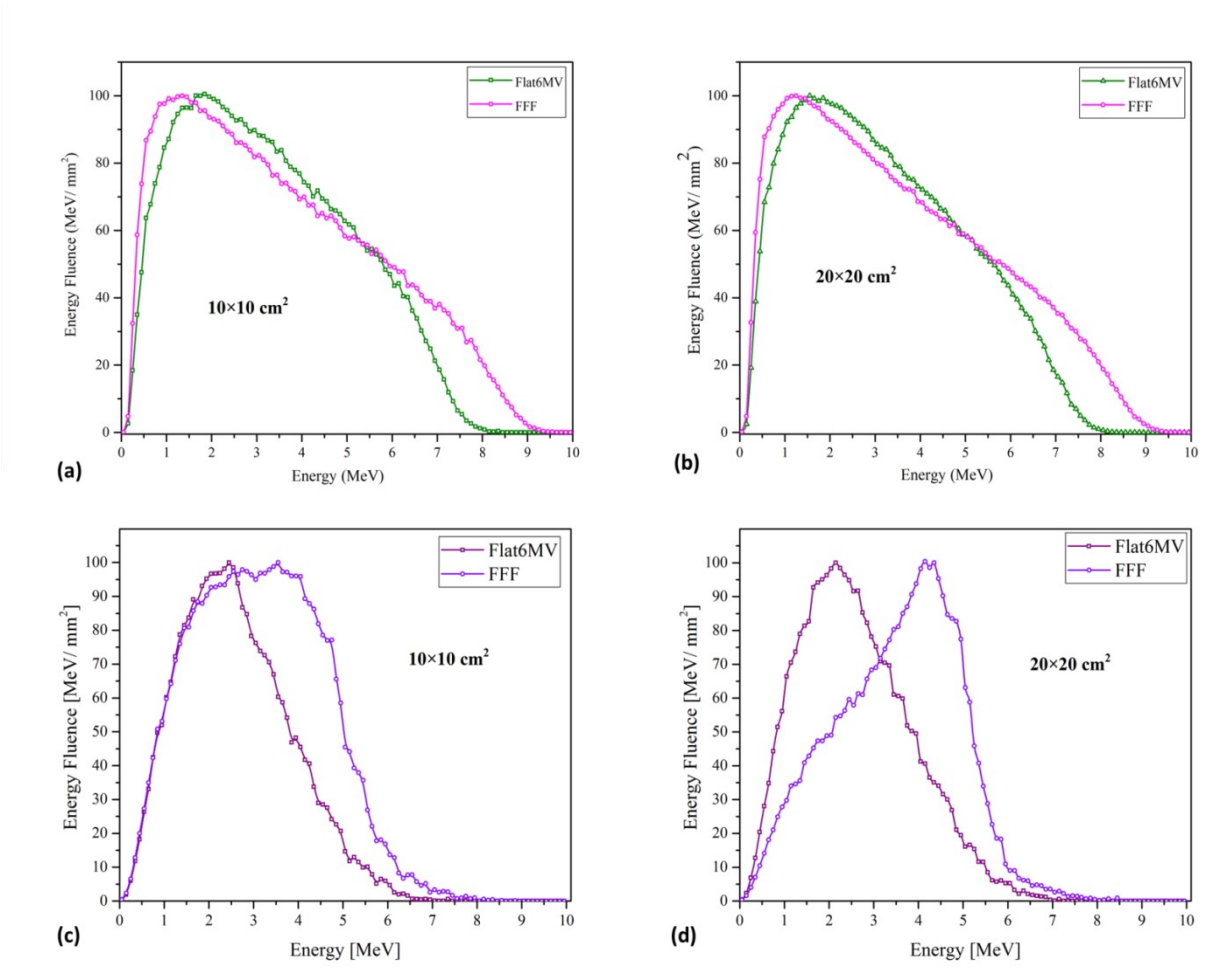

Figure 4.21. Effect of removing the flattening filter on photon energy fluence (a,b) and electron energy fluence (b,c)

3.7.7 Off-axis change

Because of the shape of the flattening filter, the dependency of the photon beam characteristics on off-axis distance is expected to be more considerable for flattened beams than FFF beams. These dependencies on OAD for depth-dose curves of FFF and flat 6 MV beam are quantified in Table 4.10 by the ratio D_{20}/D_{10}.

Table 4.10. Comparison of calculated D_{20}/D_{10} of FFF at various OAD with flat 6 MV beams (20×20 cm^2 field).

OAD (cm)	D_{20}/D_{10}	
	FFF	Flat 6 MV
CAX	0.614	0.614
2.5	0.6257	0.642
5	0.6324	0.634
7.5	0.6420	0.623

Table 4.11 reports the calculated mean energy of the FFF beam on the CAX and at different OAD for the 20×20 cm^2 field. For FFF beams, the mean energy was 1.87, 1.85, 1.86, 1.87 MeV at OAD 0, 2.5, 5, 7.5 cm, respectively. Therefore, there is less than 0.5% variation in mean energy when the OAD increases from zero up to 7.5 cm.

Table 4.11. Calculated photon mean energy of FFF beam on CAX and at difference OAX for 20×20 cm^2 field size.

OAD (cm)	Mean energy (MeV)	
	FFF	Flat 6 MV
CAX	1.87	2.06
2.5	1.85	2.02
5	1.86	1.91
7.5	1.87	1.81

Figure 4.22 also shows that for FFF beams, the OAD has no strong effect on the mean energy of the photons, as no marked hardening effect occurs at various distance of off-axis. Nevertheless, the photon fluence was decreased by increasing the OAD, as is expected from the bremsstrahlung intensity distribution. It is clear in Figure 4.22 that the effect of OAD on the mean energy for the flattened beam is more considerable. Our simulations show that the mean photon energy decreases by about 12% from 2.06 MeV on the CAX to 1.81 MeV at an OAD 7.5 cm.

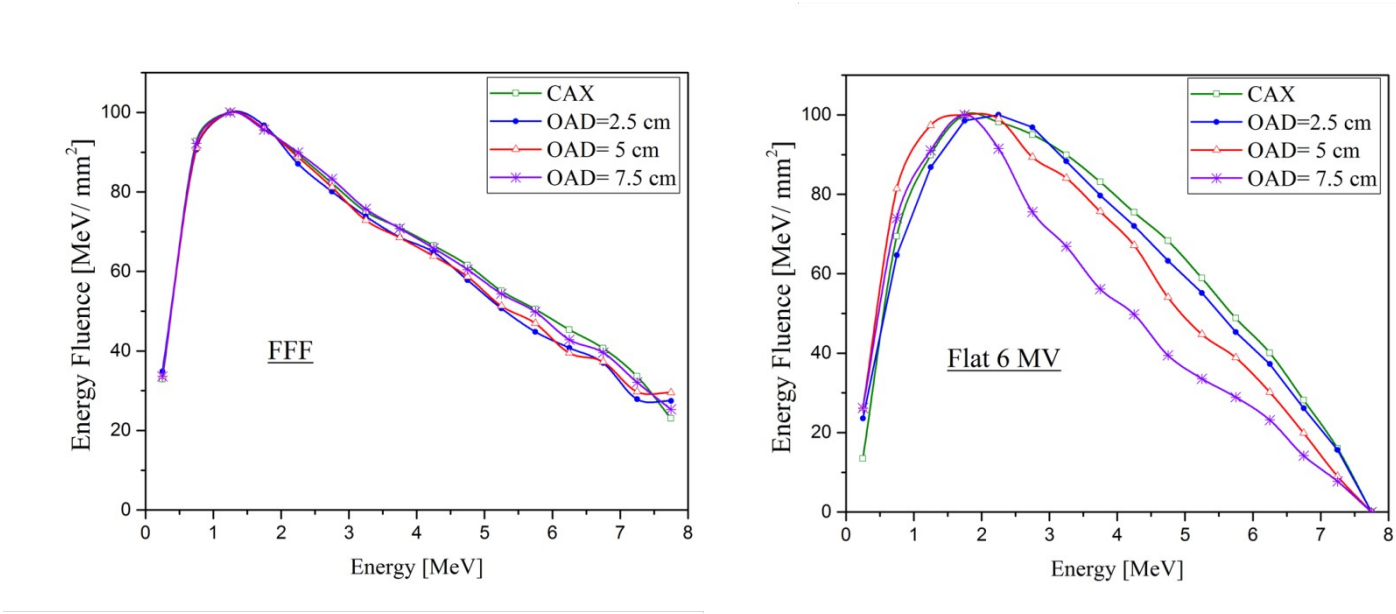

Figure 4.22. Calculated photon energy fluence on the CAX and as a function of OAX for FFF and flat 6 MV with 20×20 cm^2 field size.

5. Discussion

In recent years, a number of studies have studied flatting filter free modes of standard linacs with the aim to dosimetrically characterize the FFF beams and find the advantages and disadvantages of this model. Most studies have focused on the Varian and Elekta linacs, for which the technical implementation of the FFF mode is somewhat different from the Siemens approach. The present study has therefore focused on the Siemens Artiste FFF 7 MV and flat 6 MV beam lines, both of which are in routine use at our institution. The Monte Carlo model created in Geant4 could reproduce the measured dosimetric data and yield further insight into spectral properties, surface dose and off-axis effects which are difficult to obtain experimentally.

In the section of results, we showed that there is good agreement between calculation and experimental result and the absolute difference of our calculations was less than 2% and the most cases less than 1%.

Fine-tuning the electron beam parameter was the most important challenge in the simulation. In contrast to other vendors (Varian or Elekta), the Siemens implementation increases the incident electron beam energy for the FFF beam line to create closely similar depth-dose curves for the flat 6 MV and FFF 7 MV beams.

Concequently in the present work, the mean electron energy for the FFF beam and flat 6 MV was different (8.8 MeV/7.5 MeV for FFF/flat 6 MV), the spread energy and spot size of the selected Gaussian distribution were similar for two configuration (0.4 MeV and 1 mm, respectively). A Gaussian distribution for the simulation of primary electrons is common in most works, [e.g. 50, 18, 20] (the Siemens Primus, Varian True Beamline, and Elekta linear accelerator, respectively). But for the mean energy of primary electron there is a significant difference between our simulation and other studies. This can be because of the geometry and materials which we used in target construction of the treatment head.

The Artiste target is made of seven layers of Titanium, Graphite, Tungsten, Nicoro, Copper and Stainless steel with thickness of 13.71 mm while, in some studies [31, 12, 15] the target was made a layer of titanium, tungsten, copper, or a few millimeter thickness mix of them. Therefore the mean energy for Artiste is 8.8 MeV while, in other studies or other linacs, that was less than 6.6 MeV for FFF beams. Regarding Siemens Primus linacs [12, 62], the mean energy of 5.75 MeV and the spread energy of the 0.127 MeV were reported which in our worked the spread energy was 0.4 MeV. Ultimately, according to Figure 4.1, the mean and spread energy were accepted with an absolute difference of less than 1% and the FWHM was accepted in Figure 4.2 with 2% absolute difference.

After finding the electron parameters and confirming the validation of our simulation, we can compare our results about the dose characteristics with other publications. The first one is the comparison of the penetration by value of D_{20}/D_{10} for both beam modalities. Table 5.1 summarizes some results of the other studies for this value.

In the most similar studies, the value of D_{20}/D_{10} of for FFF beams was lower while, the percent increase was approximately similar. Kajaria et al. [31] simulated a VarianClinac 600, reporting that the D_{20}/D_{10} is 0.54 for 10×10 cm^2 and 0.588 for 20×20 cm^2 field sizes and this ratio increases by about 8% with increasing the field size. Mohammed et al. [46] simulating the Varian 2100 showed a value of 0.54/0.57 for 10×10 cm^2/20×20 cm^2, which increased by 5%. And the study of Gete et al. [25] on a Varian linac seems convergent with our result so that, the D_{20}/D_{10} increased about 4% by increasing the field size.

Regarding flattened beams, the value of penetration was in the range of other studies reported in Table 5.1 with absolute difference less than 7% for both open field sizes. Totally, the penetration of Siemens Artiste was larger than other vendors.

Table 5.1. Penetration (D_{20}/D_{10}) for square field sizes of 10 and 20 cm, overview of previous studies

Author	**Vendor**	**FFF 7 MV**		**Flat 6 MV**	
		10×10 cm²	**20×20 cm²**	**10×10 cm²**	**20×20 cm²**
Kajaria et al. [31]	VarianClinac 600	0.54	0.588	0.56	0.598
Mohammed et al. [46]	Varian 2100	0.54	0.57	0.569	0.607
Gete et al. [25]	Varian TrueBeam	0.55	0.576	-	-
Kajaria et al. [30]	Varian Clinac 600	0.54	0.544	0.567	0.572
Present work	Siemens Artiste	0.587	0.614	0.578	0.614

One of the results of removing the flattering filter is increasing the dose rate. Most previous works reported an increase in dose rate by factor of 2 ([27, 12] for Siemens ONCOR Avant-Garde and Siemens Primus linacs). For the other vendors, recently Sangeetha et al. [61] reported a relative dose rate of 2.52 (2.60) for the 10×10 cm² (20×20 cm²) field for a Varian 600C/D and Dalaryd et al. [16], observed that the dose rate of the FFF beams increased by a factor of 2.23 for an ElektaPrecise. Notably, the values for our Siemens Artiste were larger than previous ones with dose rate of 2.8 (2.96) for the 10×10 cm² (20×20 cm²) fields.

Yarahmadi et al. [78] evaluated the penumbral width of the VarianClinac2100 linear accelerator using the EGSnrc/ BEAMnrc Monte Carlo code and reported a 0.3 mm /0.2 mm reduction in penumbra for 10×10 cm²/20×20 cm² fields by removing the flattening filter. Comparing this with our work this reduction was 0.1 mm less than our results for 10×10 cm² field size while for the 20×20 cm² field size had a similar value.

Our obtained relative surface dose of the flat 6 MV beam line tended to decrease by about 21% (22%) for 10×10 cm² (20×20 cm²) field size when the flattening filter was removed from the beam line. Contrarily, Mohammed et al. [46] showed an increase in relative surface dose

by about 19 % (12%) for 10×10 cm² (20 × 20 cm²) field size by removing the flattening filter from a Varian 2100 linac included to low energy. For the Siemens FFF, our results converge with the results of Sigamani and Nambiray [76] who evaluated the buildup region and surface dose the Siemens Artiste 7 MV-FFF and 6 MV flattened photon beams using GafChromic film and two different dosimeters.

Comparing our data with previous work, we find an elevated photon mean energy at the isocenter (Table 5.2), which distinguishes the FFF 7 MV and flat 6 MV beam line from the other linac models. In all works which are mentioned in this table, the mean energy of photon beam decreased by removing the flattening filter, similar to present work. However, for the Siemens linac this decrease is less pronounced (FFF mean energy 89 % of flat beam mean energy) than for all other vendors (ratio FFF/flat mean energy 69% – 85% for 10 cm square fields). Therefore, this difference of Artiste in mean energy was clearly observed in the depth-dose curve in which the maximum dose was obtained at a deeper position and the value of penetration (D_{20}/D_{10}) was higher than in previous studies.

Table 5.2. Photon mean energy at isocenter for square field sizes of 10 and 20 cm, overview of previous studies

Author	**Vendor**	**FFF 7 MV**		**Flat 6 MV**	
		10×10 cm²	**20×20 cm²**	**10×10 cm²**	**20×20 cm²**
Mesbahi et al., 2007 [43]	Elekta SL-25 linac	1.47	1.44	1.73	1.71
Vassiliev et al., 2006 [72]	Varian Clinac 2100	1.22	1.22	1.77	1.77
Mesbahi, 2007 [44]	Varian Clinac 21EX	1.32	1.31	1.76	1.64
Yarahmadi et al., 2013 [78]	VarianClinac2100	1.26	1.26	1.81	1.81
Kajaria et al., 2017 [31]	Varian Clinic 600 unique	-	1.23	-	1.52
Czarneckia et al.,2017 [15]	Siemens KD	1.839	-	-	-
Present work	Siemens Artiste	1.9	1.87	2.14	2.06

Regarding the beam profiles and normalization, we have shown that it is possible to apply the renormalization method [21] to the Siemens FFF 7 MV and flat 6 MV beams. This is not *a priori* trivial, because this method was developed for Varian FFF beams which do not differ from the flat beam except in the omission of the flattening filter. Therefore, the FFF beams are then renormalized to their “identical” flat counterpart. In our case, the energy of the FFF beam is adjusted so that the two beam lines are no longer intrinsically identical, which might result in different normalization, penumbra, and other characteristics. On the other hand, the FFF beam is matched to the flat beam regarding the depth-dose curve. It might therefore be useful to consider the two beam lines as “pdd-matched”. In fact, this would result in more similar spectral and absorption properties than for an implementation of FFF energies which just lacks a flattening filter. As our results show, the “shoulder point” or “renormalization method” can successfully be applied to this implementation of a pdd-matched FFF beam line as well, so that a good match both of the pdd and the profile properties of the two beam lines can be achieved.

6. Conclusions

The aim of present work was the physical modelling of a Siemens Artiste medical linear accelerator which installed at the Department of Radiotherapy of the Saarland University Medical Center is equipped with a new technique for obtaining higher-output photon beams, called a flattening-filter-free (FFF) mode. Geant4 toolkit was used as simulation Monte Carlo code because of wide scope of applications, availability of source code, flexibility in the design of complex geometries and support with the code extension team for regular troubleshooting.

Both configurations of the linac (flat and FFF) were simulated and compared with the measurements using a Semiflex ionization chamber (PTW 31010) in a PTW MP3 phantom to verify the validation of simulation and tuning the primary electron parameters. To reduce computation times and improve the simulation efficiency, the simulations were performed in two steps (first, creating the phase space file (PSF) before jaws and then using PSF as virtual source) to calculate the dosimetric properties for two field size of 10×10 cm^2 and 20×20 cm^2.

The mean primary electron energy for the FFF beam was 8.8 MeV and 7.5 MeV for flat 6 MV, the spread energy and spot size of the selected Gaussian distribution source were 0.4 MeV and 1 mm, respectively. Lideatically for flat and FFF simulation results had good agreement with experimental results thus the absolute difference between measurements and calculations was less than 2% for depth doses and beam profiles.

Because of the reduced scattering and less photon absorption in the case of FFF beam the dose rate of the FFF beam was 2.8 (2.96) times higher than for the flattened beam for a field size of 10×10 (20×20) cm^2. Also, the FFF beam creates less surface dose because of less scattering compared to the flattened beam. The surface dose of the FFF beam was about 21% less than for the flat 6 MV for open field 10×10 cm^2 and 20% less for 20×20 cm^2.

The FFF beams have a smaller penumbra because these beams have softer spectrum besides the smallest scattering. The penumbra of the 10 cm square open field size of flattened beam was 0.4 mm larger than for the corresponding FFF beam and this difference was 0.2 mm for 20 cm square open field size. Unflatness and slope decreases with increasing depth were more considerate for the open field size of 10×10 than 20×20 cm^2. Peak position and symmetry were -0.34 mm/0.25 mm and 2.7%/1.4% for 10×10 cm^2/20×20 cm^2. These possible differences may be because of statistical uncertainties of simulation and the definition of the normalization factor.

Although the primary electrons in flat 6 MV configuration have lower energy compared to FFF, the mean energy was higher for the flat 6 MV beams because of the hardening beam effect of the flattening filter. The mean energy of photons of the 10×10 cm^2 field size was 1.91/ 2.14 MeV for FFF / flat 6 MV beams and was 1.87 / 2.06 MeV for 20×20 cm^2. Totally, the electron mean energy of the FFF beam was larger than for the flattened beam and there was more electron contamination on the surface of the water phantom for FFF beams.

The dependency of the photon beam characteristics on off-axis distance was more considerable for flattened beams than FFF beams, for example the OAD has no strong effect on the mean energy of the photons of FFF mode, as no marked hardening effect occurs at various off-axis distances.

7. Directory of tables

8. Directory of figure

9. References

[1] Abdulraheem Kinsara A, Ahmed Sherif El-Gizawy A SH, Banoqitah E, Ma X (2016) J Nucl Med Radiat Ther 7: Review of Leakage from a Linear Accelerator and Its Side Effects on Cancer Patients. 288. doi:10.4172/2155-9619.1000288.

[2] Agostinelli S. et al. (2003) Nuclear Instruments and Methods in Physics Research Section A: Accelerators, Spectrometers, Detectors and Associated Equipment: Geant4-a simulation toolkit. 506, pp.250-303.

[3] Allison J, Amako K, Apostolakis J, Araujo H, et al. (2006) Nuclear Science, IEEE Transactions on: Geant4 developments and applications. 53(1):270–278.

[4] Allison J, Garnier L, Kimura A, Perl J (2013) International Journal of Modeling, Simulation,and Scientific Computing: The Geant4 visualization system-a multi driver graphics system. Vol. 4, 1340001.

[5] Allison J, Amako K, et al. (2016) Nuclear Instruments and Methods in Physics Research Section A: Accelerators, Spectrometers, Detectors and Associated Equipment: Recent developments in Geant4. Volume 835, Pages 186-225.

[6] Andreo P (1991) Phys Med Biol.: Monte Carlo techniques in medical radiation physics. 36(7):861-92

[7] Andersona C, McKinneya G, Tutta J, Jamesb M (2017) Physics Procedia :Delta-ray Production in MCNP 6.2.0, Conference on the Application of Accelerators in Research and Industry. 90 .229 – 236.

[8] Astro Targeting cancer care (2013) Retrieved from https://www.astro.org/Affiliate/ARRO/Resident Resources/Educational Resources/Image-Challenge/Content-Pieces/Physics-1/.

[9] Berger MJ (1963) Methods in Comput. Phys.: Monte Carlo calculation of the penetration and diffusion of fast charged particles.1:135 – 215.

[10] Capote R, Jeraj R, Ma CM, Rogers DWO, Sánchez-Doblado F, Sempau J, Seuntjens J, Siebers JV (2006) IAEA (International Atomic Energy Agency) Technical Report INDC(NDS)-0484: Phase-space database for external beam radiotherapy.Available from the website: http://wwwnds.iaea.org/phsp/documents/indc-nds-0484.pdf.

[11] Cashmore J (2008) Phys Med Biol.: The characterization of unflattened photon beams from a 6 MV linear accelerator. 53:1933–46.

[12] Chofor N, Harder D, Willborn K, Rühmann A, PoppeB (2011) Phys. Med. Biol.: A direction-selective flattening filter for clinical photon beams. Monte Carlo evaluation of a new concept. 56(14):4355-76.

[13] Cort´es-Giraldo M A, Quesada J M, Gallardo M I, Roberto Capote R (2009) Geant4 Interface to Work with IAEA Phase-Space Files.

[14] Constantin M, Perl J, LoSasso T, Salop A, Whittum D, Narula A, Svatos M, Keall PJ (2011) Med Phys.: Modeling the truebeam linac using a CAD to Geant4 geometry implementation: dose and IAEA-compliant phase space calculations. 38(7): 4018-24.

[15] Czarnecki D, Poppe B, Zink K (2017) Med. Phys.: Monte Carlo-based investigations on the impact of removing the flattening filter on beam quality specifiers for photon beam dosimetry. 44 (6).

[16] Dalaryd M, Kragl G, Ceberg C, Georg D, McClean B, Wetterstedt S, et al. (2010) Phys Med Biol.: A Monte Carlo study of a flattening filter-free linear accelerator verified with measurements.55:7333–44.

[17] Dalaryd M (2015) Doctoral dissertation: Dosimetric effects of removing the flattening filter in radiotherapy treatment units. Retrieved from https://www.lunduniversity.lu.se/lup/publication/37d0be6b-1211-4c31-8624-f2a5636744e8.

[18] Efendi MA, Funsian A, Chittrakarn T, Bhongsuwan T(2017) Sains Malaysiana: Monte Carlo Simulation of 6 MV Flattening Filter Free Photon Beam of True Beam STx LINAC at Songklanagarind Hospital. 46(9):1407-1411.

[19] F. A. A. Ajaj, N. M. H. Ghassal (2003) Phys. Eng. Sci. Med: An MCNP-based model of a medical linear acceleratorX-ray photon beam.Australas.Vol. 26, No 3.

[20] Feng Z, Yue H, Zhang Y, Wu H, Cheng J, Su X (2016) mode.Radiat Oncol: Monte Carlo simulation of beam characteristics from small fields based on TrueBeam flattening-filter-free. 11:30.

[21] Fogliata A, Garcia R, Knoos T, Nicolini G, Clivio A, Vanetti E, Khamphan C, Cozzi L. (2012) Med Phys: Definition of parameters for quality assurance of flattening filter free (FFF) photon beams in radiation therapy. 39(10):6455-64.

[22] Fogliata A, Fleckenstein J, Schneider F, Pachoud M, Ghandour S, Krauss H, Reggiori G, Stravato A, Lohr F, Scorsetti M, Cozzi L (2016) Med Phys: Flattening filter free beams from TrueBeam and Versa HD units: Evaluation of the parameters for quality assurance. 43(1):205.

[23] Georg D, Kragl G, Wetterstedt S, McCavana P, McClean B, Knoos T (2010) Med Phys: Photon beam quality variations of a flattening filter free linear accelerator. 37:49–53.

[24] Geant4 Collaboration (2017) Geant4 User's Guide for Application Developers (Release 10.4). Retrieved from http://geant4-userdoc.web.cern.ch/geant4 userdoc/UsersGuides/ForApplicationDeveloper/fo/BookForAppliDev.pdf.

[25] Gete E, Duzenli C, Milette MP, et al. (2013) Med Phys: A Monte Carlo approach to validation of FFF VMAT treatment plans for the TrueBeamlinac. 40(2):021707.

[26] Hahn CH, Kim IS, Park ST, Cho BH (2007) Journal- Korean Physical Society: First observation of signals due to KAERI's 10 MeV electron beam by using GEM detectors. 50(4).

[27] Huang Y, Alfredo Siochi R, Bayouth JE (2012) Journal of Applied Clinical Medical Physics: Dosimetric properties of a beam quality-matched 6 MV unflattened photon beam. 13(4): 71-81.

[28] IUPAC, Compendium of Chemical Terminology, 2nd ed. (the "Gold Book") (1997) Online corrected version: (2006) "Auger effect".Retrieved fromhttps://en.wikipedia.org/ wiki/Auger_effect.

[29] Jiang SB, Kapur A, Ma CM (2000) Med Phys: Electron beam modeling and commissioning for Monte Carlo treatment planning.27(1):180-91.

[30] Kajaria A, Sharma N, Sharma Sh, Pradhan S, Mandal A, Aggarwal LM (2016) J Biomed Phys Eng: Monte Carlo Study of Unflattened Photon Beams Shaped by Multileaf Collimator.ISSN:2251-7200.

[31] Kajaria A, Sharma N, Sharma S, Pradhan S, Mandal A, Aggarwal ML (2017) Biomedical Research: Monte Carlo study of a flattening filter-free 6 MV photon beam using the BEAMnrc code. 28 (4): 1566-1573.

[32] Kawrakow I (2000) Med Phys: Accurate condensed history Monte Carlo simulation of electron transport. I. EGSnrc, the new EGS4 version.27 (3):485-98.

[33] Kawrakow I (2000) Med Phys: Accurate condensed history Monte Carlo simulation of electron transport. II. Application to ion chamber response simulations. 27(3):499-513.

[34] Kragl G, Wetterstedt S., Knausl B, Lind M, McCavana P, Knoos T, et al. (2009) Radiother Oncol: Dosimetric characteristics of 6 and 10 MV unflattened photon beams. 93(1):141-6.

[35] Kry SF, Howell RM, Titt U, Salehpour M, Mohan R, Vassiliev ON (2008) Med Phys: Energy spectra, sources, and shielding considerations for neutrons generated by a flattening filter-free Clinac.35:1906–11.

[36] Kry SF, Titt U, Ponisch F, Vassiliev ON, Salehpour M, Gillin M, et al. (2007) Int J Radiat Oncol Biol Phys: Reduced neutron production through use of a flattening-filter-free accelerator. 68:1260–4.

[37] Kry SF, Howell RM, Polf J, Mohan R, Vassiliev ON (2009) Phys Med Biol: Treatment vault shielding for a flattening filter-free medical linear accelerator.. 54:1265–73.

[38] Labinot K, Gazmend N, Gëzim S (2016) RAD Conference Proceedings: The penumbra of irradiations in linear accelerators, its use in radiotherapy of cancer diseases, negative effects, and the possibilities of reduction them. vol. 1, pp. 111-113.

[39] Liu HH, Mackie TR, McCullough EC (1997) Med Phys: A dual source photon beam model used in convolution/superposition dose calculations for clinical megavoltage X-ray beams..24(12):1960-74.

[40] Mader JE (2014) Master's thesis: Flattening Filter Free Photon Beams for Treatment of Early-Stage Lung Cancer: An Investigation of Peripheral Dose. Retrieved fromhttps://dspace.library.uvic.ca/handle/1828/5806.

[41] Mark EL, Jeffrey VK, James KC Liu (2015) CHAPTER 247: General and Historical Considerations of Radiotherapy and Radiosurgery. Retrieved from https://clinicalgate.com/general-and-historical-considerations-of-radiotherapy-and-radiosurgery/.

[42] Mathiszik B (2005) Closing the gap between AXI and semi-automated systems. Retrieved from https://www.embedded.com/print/4382009.

[43] Mesbahi A, Mehnati P, Keshtkar A, Farajollahi A (2007) Radiat Med: Dosimetric properties of a flattening filter free 6 MV photon beam: a Monte Carlo study. 25:315–24.

[44] Mesbahi A (2007) Appl Radiat Isot: Dosimetric characteristics of unflattened 6 MV photon beams of a clinical linear accelerator: a Monte Carlo study.65(9):1029-36.

[45] Mohamed Ariff bin Jaafar Sidek (2010) Doctor of Philosophy dissertation: Monte Carlo investigations of radiotherapy beams: studies of conventional, stereotactic and unflattened beams. Department of Medical and Radiation Physics School of Physics and Astronomy, The University of Birmingham.

[46] Mohammed M, Chakir E, Boukhal H, Mroan S, El Bardouni T (2017) Journal of King Saud University-Science: Evaluation of the dosimetric characteristics of 6 MV flattened and unflattened photon beam. 29, 371–379.

[47] Moreno M Z (2012) Doctoral dissertation: Monte Carlo simulations for dosimetric verification in photon and electron beam radiotherapy. Retrieved from https://run.unl.pt/handle/10362/7835?locale=en.

[48] Nave R. Auger Effect. Retrieved fromhttp://hyperphysics.phy-astr.gsu.edu/hbase/Atomic/auger.html.

[49] Parsai EI, Pearson D, Kvale T (2007) Nucl Instrum Methods Phys Res B: Consequences of removing the flattening filter from LINACs in generating high dose rate photon beams for clinical applications: A Monte Carlo study verified by measurement.261:755–9.

[50] Pearson D, Parsai E, Fledmeier J (2006) Med Phys: Evaluation of dosimetric properties of 6 and 10 MV photon beams from a linear accelerator with no flattening filter. 33:2099.

[51] Pönisch F, Titt U, Vassiliev ON, Kry SF, Mohan R (2006) Med Phys: Properties of unflattened photon beams shaped by a multileaf collimator. 33:1738–46.

[52] Pönisch F, Titt U, Oleg N, Vassiliev S K, Mohan R (2006) Med Phys : Properties of unflattened photon beams shaped by a multi-leaf collimator. 33, pp. 1738-1746.

[53] Ragheb M (2013). Russian Roulette and particle splitting. Retrieved from http://mragheb.com/NPRE%20498MC%20Monte%20Carlo%20Simulations%20in%20Engineering/Russian%20Roulette%20and%20Particle%20Splitting.pdf.

[54] Retrieved from https://en.wikipedia.org/wiki/Duane%E2%80%93Hunt_law. (8)

[55] Retrieved from https://physics.tutorvista.com/modern-physics/compton-scattering.html. (28)

[56] Retrieved from http://scientificsentence.net/Radiations/index.php?key=yes&Integer=attenuation. (29)

[57] Retrieved from http://www.ptw.de/2097.html. (59)

[58] Retrieved from http://www.rpdinc.com/ptw-31010-0125cc-semiflex-chamber-972.html. (60)

[59] Rogers DWO, Faddegon BA, Ding GX, Ma CM, We J, Mackie TR (1995) Med Phys: BEAM: a Monte Carlo code to simulate radiotherapy treatment units. 22(5):503-24. (44)

[60] Rogers DWO, Kawrakow I, Seuntjens JP, Walters BRB, Mainegra-Hing E (2018) NRCC Report: NRC User Codes for EGSnrc. PIRS-702(revC).

[61] Sangeethaa S, Surekab CS (2017) Radiation Physics and Chemistry: Comparison of Flattening Filter (FF) and Flattening-Filter-Free (FFF) 6 MV photon beam characteristics for small field dosimetry using EGSnrc Monte Carlo code. 135 (2017) 63–75.

[62] Sardari D, Maleki R, Samavat H, Esmaeeli A (2010) Rep Pract Oncol Radiother: Measurement of depth-dose of linear accelerator and simulation by use of Geant4 computer code. Reports of practical oncology and radiotherapy.15 (3): 64–68.

[63] Sawkey DL, Faddegon BA (2009) Med Phys: Determination of electron energy, spectral width, and beam divergence at the exit window for clinical megavoltage X-ray beams.36:698–707.

[64] Seco J (Ed.), Verhaegen F (Ed.) (2013) Boca Raton: Monte Carlo Techniques in Radiation Therapy. CRC Press.

[65] Sharma SD (2011) J Med Phys: Unflattened photon beams from the standard flattening filter free accelerators for radiotherapy: Advantages, limitations and challenges. 36(3): 123–125.

[66] Sigamani A, Nambiraj A (2017) Rep Pract Oncol Radiother: Comparison of surface dose delivered by 7 MV-unflattened and 6 MV-flattened photon beams. 22:243-250.

[67] Sikora M, Dohm O, Alber M (2007) Phys Med Biol: A virtual photon source model of an Elekta linear accelerator with integrated MLC for Monte Carlo based dose calculation. 52(15):4449-63.

[68] Taylor A, Powell ME (2004) Cancer Imaging: Intensity-modulated radiotherapy-what is it? 68-73.

[69] Teoh M, Clark CH, Wood K, Whitaker S, Nisbet A (2011) Br J Radiol: Volumetric modulated arc therapy: a review of current literature and clinical use in practice. 84(1007): 967–996.

[70] Titt U, Vassiliev ON, Ponisch F, Kry SF, Mohan R (2006) Med Phys: Monte Carlo study of backscatter in a flattening filter free clinical accelerator. 33:3270–3.

[71] Tsechanski A, Krutman Y, Faermann S (2011) J Med Phys: On the existence of low-energy photons (<150 keV) in the unflattened X-ray beam from an ordinary radiotherapeutic target in a medical linear accelerator. 36(3):123–125.

[72] Vassiliev ON, Titt U, Kry SF, Pönisch F, Gillin MT, Mohan R (2006) Med Phys: Monte Carlo study of photon fields from a flattening filter free clinical accelerator.33(4):820-7.

[73] Vassiliev ON, Titt U, Kry SF, Mohan R, Gillin MT (2007) Radiat Prot Dosimetry: Radiation safety survey on a flattening filter-free medical accelerator.124:187–90. (26)

[74] Velkley DE, Manson DJ, Purdy JA, Oliver GD Jr (1975) Med Phys: Build-up region of megavoltage photon radiation sources. 2(1):14-9.

[75] Verhaegen F, Seuntjens J (2003) Med. Biol: Monte Carlo modelling of external radiotherapy photon beams Phys. Med.Phys. 48 (2003) R107–R164. (48)

[76] Wikidot Inc. (last edited: 1 Jan 2008). Linear Accelerator. Retrieved from http://radonc.wikidot.com/linear-accelerator.

[77] Wikidot Inc. (Last edited: 1 Jan 2008). Compton Effect. Retrieved from http://electrons.wikidot.com/compton-effect.

[78] Yarahmadi M, Allahverdi M, Nedaie HA, Asnaashari K, Vaezzadeh SA, Sauer OA (2013) Z Med Phys: Improvement of the penumbra for small radio surgical fields using flattening filter free low megavoltage beams. 23(4):291-9.

10. Acknowledgements

My sincere thanks goes to Prof. Dr. Christian Rübe and Dr. Norbert Licht, who provided me an opportunity to join their team, and who gave access to the laboratory and research facilities. Without they precious support it would not be possible to conduct this research.

My journey of PhD has been a life changing experience for me and it would not have been possible without constant support and guidance from my supervisor PD Dr. Yvonne Dzierma Apart from her academic supervision, I found her extremely inspiring, who ignited the quest for knowledge in me. I am in a deficit of word to write about her role in this thesis and my life.

My special words of thanks should also go to my research co-guide Dr. Frank Nüsken for his continuous support, guidance, cooperation, encouragement.

A special mention of thanks to my friends in the Radio-oncology department of the Saarland University Medical Center in Homburg, especially Dr. Katharina Bell and Mr. Georg Blaß, who encouraged me a lot with their friendly advice and support which helped me to overcome all the obstacles during my research. Their timely help and friendship shall always be remembered.

My heartfelt regard goes to my family. Words cannot express how grateful I am to my mother, father, my brother Reza, my younger sister Fatemeh. A special thanks to my older sister, Elaheh For all her support from my first day of entry to Germany until now.

Last but not least, I am highly indebted to my husband Mohammadreza for his patience and strong persistent support and he is a big mental strength for me.